

The evolution of the Antarctic Ice Sheet
from the Last Glacial Maximum to 2100

Malou Maris

ISBN 978-90-393-6245-7

Copyright © Malou Maris, The Netherlands

Institute for Marine and Atmospheric research Utrecht (IMAU)
Faculty of Science, Department of Physics and Astronomy
Utrecht University, The Netherlands

An online version of this thesis is available via
<https://sites.google.com/site/mnamaris/>



Cover: The nightly sky, as seen from the South Pole, with a timeline from 120 000 years ago until the year 2100. On the back is a picture of the Fram ('Forward' in Norwegian), the ship used by Roald Amundsen and his crew on their expedition to the South Pole from 1910 to 1912.

The evolution of the Antarctic Ice Sheet from the Last Glacial Maximum to 2100

De evolutie van de Antarctische ijskap
van de laatste ijstijd tot 2100

(met een samenvatting in het Nederlands)

PROEFSCHRIFT

ter verkrijging van de graad van doctor aan de Universiteit Utrecht
op gezag van de rector magnificus, prof.dr. G. J. van der Zwaan,
ingevolge het besluit van het college voor promoties
in het openbaar te verdedigen op

woensdag 26 november 2014 des ochtends te 10.30 uur

door

Malou Nikea Anthea Maris

geboren op 11 januari 1986 te Ommen

Promotor: Prof. dr. J. Oerlemans

Copromotor: Dr. B. de Boer

La science, mon garçon,
est faite d'erreurs,
mais d'erreurs qu'il est bon
de commettre,
car elles mènent
peu à peu
à la vérité

from 'Voyage au Centre de la Terre'
by Jules Verne, 1864

Science, my boy,
is made up of mistakes,
but they are mistakes which it is
useful
to make,
because they lead
little by little
to the truth.

Contents

Samenvatting	ix
1 Introduction	1
1.1 History of the AIS	3
1.2 The initial state	5
1.3 External forcing mechanisms	7
1.4 Ice dynamics	14
1.5 Validation	16
1.6 Outline	17
2 Model description	19
2.1 Introduction	19
2.2 General background of the model	19
2.3 Oceanic forcing	20
2.4 The bedrock response to ice loading	23
2.5 SIA and SSA	25
2.6 Thermodynamics	27
2.7 Coupling of the model components	29
3 GCM intercomparison	31
3.1 Introduction	32
3.2 Method	33
3.3 Present-day results	38
3.4 Mid-Holocene results	40
3.5 LGM results	44
3.6 Conclusions	46

4	Model sensitivity	49
4.1	Introduction	50
4.2	Method	51
4.3	The reference simulation	61
4.4	Results of the sensitivity experiments	64
4.5	Conclusions	69
5	The evolution of the AIS from the LGM to 2100	71
5.1	Introduction	72
5.2	Methods	72
5.3	Results	83
5.4	Conclusions	93
6	Conclusions and outlook	97
6.1	Conclusions	97
6.2	Outlook	101
	List of acronyms	103
	Bibliography	105
	Dankwoord	113
	About the author	115

Samenvatting

De Antarctische ijskap is gelegen in het zuidpoolgebied en is de grootste ijskap op aarde. In tegenstelling tot het ijs rondom de noordpool ligt het meeste ijs van Antarctica op land. Wanneer ijs van het land in zee terecht komt draagt het bij aan de stijging van het zeeniveau. Als al het ijs van Antarctica zou verdwijnen, zou het mondiaal zeeniveau bijna 60 meter stijgen. Het grootste deel van de ijskap is onder de huidige omstandigheden echter stabiel en zal op korte termijn niet verdwijnen als de temperatuur een aantal graden stijgt. Grotere veranderingen in de ijskap zijn wel zichtbaar over lange tijdschalen. Zo heeft de Antarctische ijskap vooral in het westelijk deel (ten zuiden van Amerika en de Stille Oceaan) veel veranderingen ondergaan sinds de laatste ijstijd, ongeveer 21 000 jaar geleden. De temperatuur was toen ongeveer 10 graden lager dan nu, en het zeeniveau was bijna 120 meter lager. Die 120 meter lag toen in de vorm van ijs opgeslagen op de landmassa's van Noord-Amerika, Eurazië en Antarctica, waarbij Antarctica een bijdrage leverde van 8 tot 25 meter. Sinds de laatste ijstijd is het volume van de ijskap afgenomen, en het is nog steeds aan het afnemen. Om te bepalen hoeveel van de ontwikkelingen die we zien, in het heden en in de toekomst, worden veroorzaakt door het natuurlijk verloop en hoeveel door menselijk toedoen, is in dit proefschrift de evolutie van de ijskap van de laatste ijstijd tot het jaar 2100 onderzocht. Voor dit onderzoek is het ijskapmodel ANICE gebruikt.

De simulaties met ANICE zijn gedaan van 120 000 jaar geleden tot nu en van 21 000 jaar geleden tot het jaar 2100. Om de simulaties te kunnen uitvoeren is er een initiële ijskap (beginsituatie van de ijskap) nodig in het model en een beschrijving van de externe invloeden (de forcering). De initiële ijskap voor de simulaties van 21 000 jaar geleden tot 2100 wordt gegeven door de simulatie van 120 000 jaar geleden tot nu die de ijskap het best modelleert in vergelijking met observaties (zie Hoofdstuk 4). Voor de simulatie van 120 000 jaar geleden tot nu hebben we aangenomen

dat de initiële ijskap ongeveer gelijk is aan de huidige ijskap omdat het klimaat en het zeeniveau ook ongeveer hetzelfde waren. De forcering bestaat uit onder andere de temperatuur van het oceaanwater, het zeeniveau en het klimaat: de luchttemperatuur en de oppervlaktemassabalans (de som van de neerslag, de smelt en andere processen die de hoeveelheid ijs aan de oppervlakte van de ijskap beïnvloeden).

Om een zo realistisch mogelijke luchttemperatuur en oppervlaktemassabalans te krijgen hebben we het regionaal klimaatmodel RACMO2/ANT gebruikt om het huidige klimaat en het klimaat ten tijde van de laatste ijstijd te simuleren. De simulatie van het huidige klimaat is ook gebruikt als forcering voor 120 000 jaar geleden omdat het volgens ijskerndata toen ongeveer even warm was op aarde. We interpoleren de temperatuur en de oppervlaktemassabalans tussen de drie tijdstippen van 120 000 jaar geleden, de laatste ijstijd en nu. De interpolatiemethode wordt in detail beschreven in Hoofdstuk 4.

RACMO2/ANT heeft input nodig uit meteorologische observaties of uit een mondiaal klimaatmodel. Voor het heden zijn er observaties beschikbaar, maar voor de laatste ijstijd is een mondiaal klimaatmodel nodig. Om het klimaat ten tijde van de laatste ijstijd zo realistisch mogelijk te kunnen simuleren met RACMO2/ANT hebben we in Hoofdstuk 3 onderzocht welk mondiaal klimaatmodel de meest realistische simulaties levert in het Antarctisch gebied, zowel in het heden als in het verleden. Met dit doel zijn 18 klimaatmodellen vergeleken met referentiedata voor het heden, het mid-Holoceen (6 000 jaar geleden) en de laatste ijstijd. Voor het heden zijn de temperatuur en de neerslag zoals gesimuleerd door RACMO2/ANT als referentie genomen. Als referentie voor het verleden zijn ijskerndata gebruikt. Over het algemeen wordt de huidige temperatuur goed gesimuleerd door de klimaatmodellen, maar de neerslag wordt overschat. Uit dit onderzoek is verder gebleken dat de onzekerheid in de simulaties van klimaatmodellen vaak groter is dan het gemeten verschil in temperatuur of neerslag tussen het verleden en het heden. Dit geldt vooral voor het mid-Holoceen, waardoor de prestaties van de klimaatmodellen moeilijk te meten zijn voor deze periode. Uit de vergelijking van de 18 klimaatmodellen is gebleken dat HadCM3 het klimaat in het Antarctisch gebied het meest realistisch simuleert. In de rest van het onderzoek zijn resultaten uit HadCM3 dan ook gebruikt als input voor RACMO2/ANT om zo een klimatologische forcering te krijgen voor ANICE.

Om een gevoel te krijgen voor welke parameters in ANICE belangrijk zijn voor het modelleren van de Antarctische ijskap en om een zo realistisch mogelijke initiële ijskap te krijgen om simulaties van 21 000 jaar geleden tot 2100 mee te starten, zijn in Hoofdstuk 4 gevoeligheidsexperimenten gedaan van 120 000 jaar geleden tot nu. Via deze experimenten zijn de effecten van het veranderen van vijf parameters onderzocht. De eerste twee parameters betreffen het gemak waarmee het ijs over het onderliggende land glijdt. Dit glijden gebeurt als de wrijving tussen de bodem en het ijs klein wordt. De derde parameter bepaalt hoe makkelijk het ijs stroomt onder invloed van deformatie (vervormingen) van het ijs. De laatste twee parameters

beschrijven hoe veel en hoe snel de aarde vervormt onder invloed van veranderingen in ijsdikte en de diepte van de oceaan. Eerst hebben we een referentiesimulatie gedefinieerd met optimale waarden voor deze vijf parameters. Deze simulatie is later ook gebruikt om de initiële ijskap voor de simulaties van 21 000 jaar geleden tot 2100 te leveren. De optimale waarden zijn bepaald door een zo realistisch mogelijke simulatie te zoeken van de huidige ijskap en van de terugtrekking van het ijs sinds de laatste ijstijd.

Een toename van het glijden van het ijs ten opzichte van deze referentiesimulatie leidt tot een afname van het volume van de ijskap door de grotere ijssnelheden op met name het westelijk deel van de ijskap. Als het ijs echter makkelijker stroomt onder invloed van deformatie leidt dit tot een afname van het ijsvolume op met name het oostelijk deel van de ijskap. Dit komt doordat het westelijk deel op een veel lager bed ligt en het ijs daar een hogere temperatuur heeft, waardoor het makkelijker glijdt dan het ijs op het oostelijk deel, dat voornamelijk wordt gedreven door deformatie. De effecten van veranderingen in de laatste twee parameters zijn het sterkst in West-Antarctica, waar de grootste veranderingen in ijsdikte hebben plaatsgevonden gedurende de afgelopen 120 000 jaar. Als de aarde meer en sneller vervormt bij een zelfde verandering in ijsdikte leidt dit tot een groter huidig ijsvolume. De reden hiervoor is dat de aardbodem in dit geval meer en sneller omhoog komt zodra het ijs begint te verdwijnen na de laatste ijstijd, waardoor er minder ijs in contact is met de zee en er dus ook minder ijs in zee verdwijnt.

De referentiesimulatie uit Hoofdstuk 4 levert een ijskap op ten tijde van de laatste ijstijd, welke is gebruikt in Hoofdstuk 5 als beginsituatie voor 80 simulaties van 21 000 jaar geleden tot 2100. Deze simulaties zijn gedaan met verschillende klimaatreconstructies om te onderzoeken welke gevolgen de onzekerheden in klimaatreconstructies hebben voor de onzekerheid in de evolutie van de ijskap. Ten eerste is de verandering in het zeeniveau tussen de laatste ijstijd en het jaar 1850 gevarieerd. Hiervoor zijn twee verschillende reconstructies gebruikt. Ten tweede zijn er vier verschillende ijskernen gebruikt om de temperatuur en de oppervlaktemasabalans te interpoleren tussen de laatste ijstijd en 1850. Het jaar 1850 wordt hier gebruikt om een scheiding te maken tussen het pre-industriële tijdperk van voor 1850 en het tijdperk waarin de opwarming van de aarde door menselijk toedoen een rol gaat spelen. Ten derde zijn er twee verschillende ijskaptopografieën gebruikt in RACMO2/ANT om het klimaat voor 21 000 jaar geleden te simuleren omdat die topografie erg onzeker is. De eerste topografie komt uit een model dat gebruik maakt van de snelheid en de grootte van de vervormingen van de aarde, waaruit de ijsdikte in het verleden kan worden afgeleid. De tweede topografie komt uit de referentiesimulatie in Hoofdstuk 4. Tenslotte zijn de simulaties doorgedraaid tot het jaar 2100 met vijf verschillende forceringen van het zeeniveau en het klimaat tussen 1850 en 2100. Deze forceringen volgen vier scenario's uit het IPCC rapport van 2014 en als vijfde forcering worden de zeespiegel en het klimaat op het niveau van 1850 gehouden (pre-industriële forcering). Dit doen we om het verschil te kunnen zien tussen

de natuurlijke ontwikkeling van de ijskap en de ontwikkeling ten gevolge van de opwarming van de aarde door menselijk handelen.

We hebben de resultaten van de simulaties van 21 000 jaar geleden tot nu vergeleken met observaties om de prestaties van het model te kunnen beoordelen. Hieruit blijkt dat ANICE zijn grenzen heeft, maar we wel de (kwalitatieve) conclusies kunnen trekken dat de zeeniveaustijging de belangrijkste factor was in het verdwijnen van het ijs sinds de laatste ijstijd, terwijl temperatuurveranderingen en het natuurlijk verloop van de ijskap de voornaamste oorzaak zijn van de veranderingen in ijsvolume in de toekomst. We schatten dat de bijdrage van de ijskap aan de wereldgemiddelde zeeniveaustijging tussen het maximale ijsvolume (ongeveer 16 000 jaar geleden) en nu 8.4 tot 12.5 meter is geweest en in 2100, ten opzichte van 2000, -22 tot 63 mm zal zijn.

CHAPTER 1

Introduction

The Antarctic Ice Sheet (AIS) is the largest ice sheet on Earth. It is situated on the southern hemisphere, includes the South Pole (see Figure 1.1) and extends to the 60th latitude South, the outer circle in Figure 1.1. Around the AIS is the Southern Ocean, incorporating a westward flowing current, the Antarctic Circumpolar Current (ACC) (Hassold et al, 2009). In contrast to the North Polar ice, most of the AIS rests on bedrock, i.e. the ice is grounded. Part of this bed, particularly underneath the western side of the ice sheet, is below sea level. The rest of the ice sheet floats on the ocean water. These parts are called ice shelves, the biggest ice shelves being the Filchner-Ronne ice shelf and the Ross ice shelf. Both of them are as big as 10 times The Netherlands, see also Table 1.1. A big difference between floating and grounded ice is that floating ice does not contribute to sea-level rise when melted, but grounded ice does.

If all ice on the AIS would melt, the global average sea level would rise by almost 60 metres (Vaughan et al, 2014). Fortunately, the largest part of the ice sheet is stable under present-day (PD) conditions and will not melt even when temperatures rise several degrees (Pollard and DeConto, 2009). However, changes in the ice cover of the Antarctic continent are visible when longer time scales of thousands of years are considered. The Last Glacial Maximum (LGM) was approximately 21 000 years (21 kyr) ago, at that time there was more ice present on Earth. Over the ice sheet, temperatures were about 10 degrees lower than today and the additional ice volume that was present at the time was equal to 120 metres sea-level equivalent (m s.l.e.), of which 8-25 metres were on the AIS (Clark and Mix, 2002; Whitehouse et al, 2012; Golledge et al, 2013). Other large ice bodies that contributed to the 120 m.s.l.e. are the Fennoscandian ice sheet over northern Europe and Asia, the Laurentide ice sheet over Northern America and the Greenland ice sheet, of which a large part still remains.

The AIS makes a regular appearance in the news nowadays, mostly connected to large chunks of ice breaking off and the question whether this is due to global warming (e.g. Amos, 2013). To be able to answer the question how global warming will affect the AIS we have to gain insights in the processes that play a role in the accumulation, melting and movement

Ice-sheet surface area ¹	13.9·10 ⁶ km ²
Ice-sheet volume ¹	26.9·10 ⁶ km ³ or 58 m sea-level equivalent
Mean ice-sheet thickness ¹	1.9 km
Floating ice surface area ¹	1.6·10 ⁶ km ²
Floating ice-sheet volume ¹	0.4·10 ⁶ km ³
Ross ice-shelf surface area ²	0.42·10 ⁶ km ²
Filchner-Ronne ice-shelf surface area ²	0.39·10 ⁶ km ²
Mean annual precipitation ³	0.19 m ice equivalent yr ⁻¹
Mean annual 2m-air temperature ³	-38°C

Table 1.1: General facts on the Antarctic Ice Sheet with superscripts indicating the source: 1) Bedmap2 (Fretwell et al, 2013), 2) ALBMAP (Le Brocq et al, 2010), and 3) RACMO2/ANT (Ligtenberg et al, 2013)

of the ice. In this thesis the AIS will therefore be studied with a numerical ice-dynamical model that takes these processes into account. The studied period runs from the LGM to the PD for two reasons. Firstly, parts of the AIS have experienced large changes during the deglaciation (the retreat of the ice sheet since the LGM). We want to know what part of the current changes on Antarctica are associated with the natural transition from a glacial into an interglacial period and what part is a consequence of human activities. Secondly, the LGM-PD period is the most constrained by observations, see Section 1.5.

Modelling the evolution of an ice sheet starts with constructing, or choosing, an ice-sheet model. A model is a simplified description, especially a mathematical one, of a system or process, to assist calculations and predictions (Oxford Dictionaries, 2013). The ice-dynamical model ANICE (e.g. De Boer et al, 2013; Helsen et al, 2012) meets this definition and is used in this thesis to study the processes involved in the evolution of the AIS. ANICE has been developed at the IMAU and will be described in more detail in Chapter 2. In this introductory chapter a general introduction to the AIS and its history will be given first in Section 1.1. Then follows a description of the three basic parts of which carrying out model simulations exists: Preparation of the input, running the model itself, and analysing the output. The input is described in Sections 1.2 and 1.3. Section 1.2 describes possible ways to initialise the model and the method of initialisation that is used throughout this thesis. The evolution of an ice sheet is driven by internal variability (e.g. differences in temperature, driving forces, etc.) and external forcings (such as air temperature and basal melt). The external forcings prescribed in ANICE are discussed in Section 1.3. This is followed by an introduction to the underlying principles of ice dynamics (Section 1.4). In order to assess its range of validity, model output should be compared to observations, which is done in Chapter 5. These observations concern both the past and the PD state of the ice sheet and are described in Section 1.5.

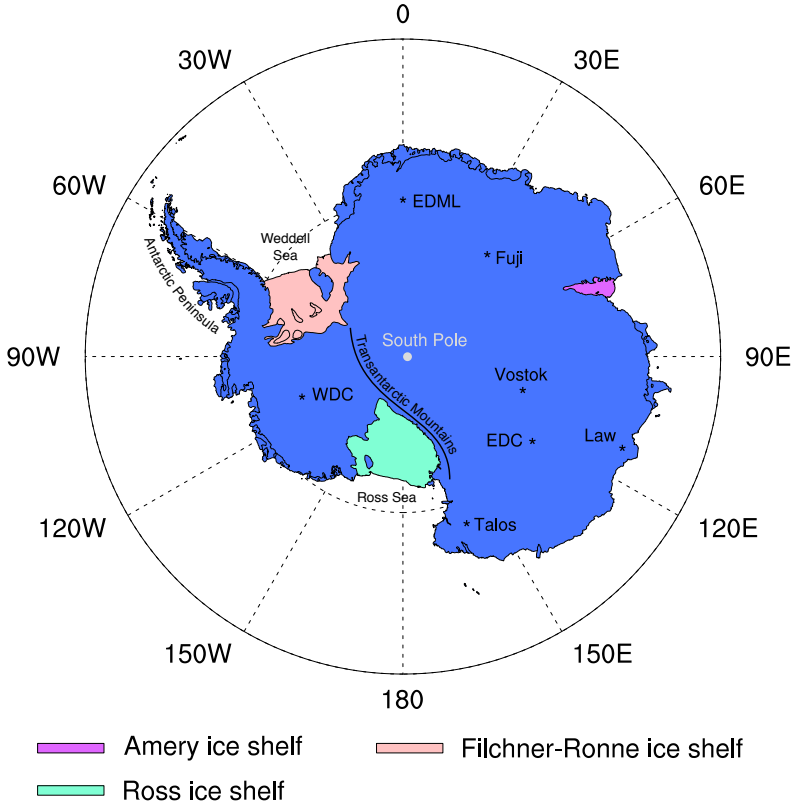


Figure 1.1: The AIS with the South Pole (90°S) indicated by the white dot. The dashed circle is drawn at latitude 75°S and the outer solid circle at 60°S . The three largest ice shelves are shown in different colours and the locations of the ice cores, from which data are used throughout this thesis, are indicated with asterisks. EDC and EDML stand for EPICA Dome C and EPICA Dronning Maudland respectively, which are both ice cores of the EPICA project (European Project for Ice Coring in Antarctica), and WDC stands for West Antarctic Ice Sheet (WAIS) Divide ice Core. The Transantarctic Mountains separate the western part of the ice sheet, the WAIS from the eastern part, the EAIS (East Antarctic Ice Sheet). The Antarctic Peninsula is part of the WAIS, but often mentioned separately because of its relatively moderate climate.

1.1 History of the AIS

About 180 million years (Myr) ago the supercontinent Gondwana started breaking up and the Antarctic continent started drifting south. Temperatures over the continent were much higher than they are today and it was populated by plants and animals. Through continental drift the Antarctic continent subsequently separated from the African continent (160 Myr ago), the Indian subcontinent (125 Myr ago), Australia-New Guinea (40 Myr ago) and finally the South-American continent (23 Myr ago) (Stonehouse, 2002). CO_2 levels in the atmosphere gradually lowered

during this period, the Antarctic continent drifted towards the South Pole and due to the separation from other continents the ACC established itself (Hassold et al, 2009). Consequently, the oceanic currents changed from mainly longitudinal (equator to pole), temperature-equalizing currents to mainly latitudinal currents which intensified the temperature differences between lower and higher latitudes. Since about 34 Myr ago the decreased CO₂-levels (see Figure 1.2) and the existence of the ACC induced the decrease of temperatures over the Antarctic continent and the eastern part (where the EAIS is now, see Figure 1.1) became mostly covered by ice (DeConto and Pollard, 2003).

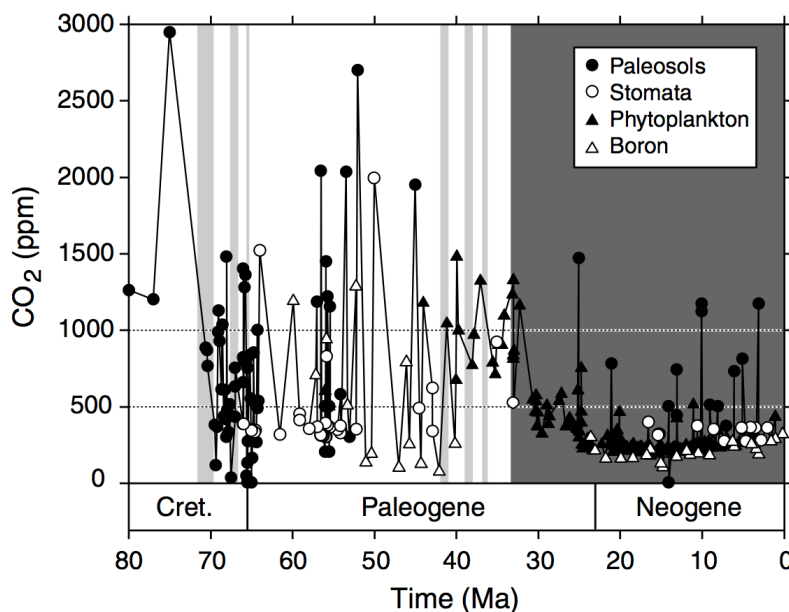


Figure 1.2: This figure was taken from Royer (2006). It shows the CO₂-record from 80 to 0 Myr ago obtained with four different measurement methods. Around 35 Myr ago the amount of CO₂ in the atmosphere has halved, after which it declined a bit further until about 15 Myr ago. Presently the amount of CO₂ in the atmosphere is about 390 ppm (Hartmann et al, 2014).

About 15 Myr ago the western part of Antarctica also glaciated and around 3 Myr ago glacial periods came into being with extended ice sheets on both hemispheres, approximately 40 kyr apart (De Boer et al, 2012). However, 0.8 to 1.2 Myr ago the glacial cycle changed from a 40 kyr period to a 100 kyr period. Several explanations have been offered for this change in period, predominantly pertaining to non-linear interactions within the climate system (Bintanja and van de Wal, 2008). The last interglacial, called the Eemian, began about 130 kyr ago and lasted at least until 118 kyr ago (Overpeck et al, 2006). Hereafter, temperatures decreased and reached a minimum around the LGM, after which they increased again to their PD level.

During the past 15 million years the western ice sheet (WAIS, see Figure 1.1)

has been strongly fluctuating. During glacial periods it would expand as far as the continental edge, while during warm interglacial periods it collapsed, losing almost all of its ice (Pollard and DeConto, 2009; De Boer et al, 2014a). These collapses are probably caused by a large part of the WAIS being below sea level and the bed sloping inwards (Hughes, 1975). This hypothesis is called the marine ice sheet instability hypothesis and was first described by Weertman (1974). It asserts that ice discharge over the grounding line (the boundary between grounded and floating ice) should increase when ice thickness increases. A retreat of the grounding-line position leads to an increase in ice thickness and hence to an increase in ice discharge making the ice sheet retreat even further. This feedback mechanisms continues until the ice sheet has disintegrated or is stabilised on an upward sloping bed (Schoof, 2007).

Nowadays the Antarctic continent is covered by ice, although the ice volume is significantly less than it was at the LGM. Temperatures are well below zero year-round over the largest part of the continent and winter temperatures reach below $-80\text{ }^{\circ}\text{C}$. The lowest natural temperature on Earth of $-89.2\text{ }^{\circ}\text{C}$ has been measured at the Russian Vostok station on 21 July 1983 (Budretsky, 1984). Although this is still the official record low temperature, there are indications that temperatures regularly drop below $-90\text{ }^{\circ}\text{C}$ on some places on the AIS (NASA, 2013). However, these temperatures are skin temperatures measured with satellites as opposed to the 2m-air temperature measured with an automatic weather station and therefore not directly comparable. These low temperatures are reached on the EAIS, which is colder than the marine WAIS. Summer temperatures reach 5 to $15\text{ }^{\circ}\text{C}$ near the coast of the Antarctic Peninsula, where it is relatively warm due to its northern, marine location. The western part of the peninsula receives quite a lot of precipitation (more than 2000 mm per year locally) due to the persistent westerlies that strike the continent from the ocean (Van den Broeke et al, 2006). In contrast, east Antarctica is very desert-like, with generally less than 100 mm of precipitation per year, see also Figure 4.2.

1.2 The initial state

Part of the input of ANICE consists of the initial ice thickness and bed topography with which a simulation starts. To find this initial state, a reconstruction of the ice sheet is needed. An often used reconstruction of the AIS at the LGM is the ICE-5G reconstruction from Peltier (2004), see Figure 1.3. This reconstruction is based on an analysis of Glacial Isostatic Adjustment (GIA), which is the sinking and rebounding of the bedrock due to changes in ice loading. GIA is further explained in Section 1.3.3. With geodynamical models it can be predicted how much the bedrock would still be moving in the present, assuming a certain ice loading history. So, by comparing observations of bedrock movement with model output the ice loading history can be derived.

When using a reconstruction, the ice sheet will not be in balance with the im-

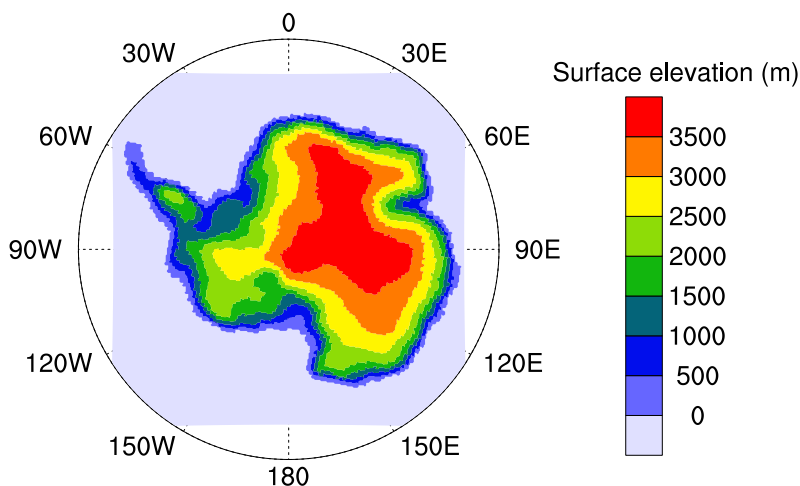


Figure 1.3: Smoothed surface elevation of the ICE-5G reconstruction.

posed climate. This is because there are uncertainties in both the ice sheet and the climate reconstructions. The modelled ice sheet will initially evolve in a reaction to the imbalance. As we are interested in the reaction of the ice sheet to a specific forcing, the model run should start before the period of interest, long enough for the ice sheet to overcome the initial imbalance. The part of the run before the period of interest is called the spin-up, used by, for example, Huybrechts (2002); Nowicki et al (2013). Another method is to calculate a so-called steady state and use this at the start of the period of interest. This method has been used by, amongst others, Golledge et al (2012) and Whitehouse et al (2012). A steady state is accomplished by running the model forward with the initial forcing and reconstructed ice sheet until an equilibrium state has been reached. This goal is met when, for instance, the ice-sheet volume does not change significantly anymore. The difference between these two methods is that in the first method the forcing is changed with time, so the ice sheet has a different 'memory' of its past when the period of interest starts (e.g. the ice temperature is different) then when the forcing was constant over time (the steady-state method). It has been argued that the memory is more realistic for the spin-up method (Nowicki et al, 2013). Furthermore, with the spin-up method it is not necessary to assume that the ice sheet is in a steady state at any one point in time, so this method is what we use in this study.

In this thesis, the PD AIS is used as a reconstruction of the ice sheet at the end of the last interglacial, 120 kyr ago. The temperature and sea level were very close to what they are now (Jouzel et al, 2007; Rohling et al, 2009). During the first 100 kyr, the ice sheet can adapt to the initial imbalance, after which the period of interest starts (LGM to PD).

120 kyr ago the temperature and sea level were very close to what they are to-

day. Therefore, we assume in this study that the ice sheet was close to its PD state and we use PD bed topography, ice thickness and climate as an initial state for the spin-up runs starting at 120 kyr ago. PD observations of bed topography, ice thickness and surface elevation from different sources have been combined in a comprehensive dataset called BEDMAP (Lythe et al, 2001). In this study a re-analysis of this dataset is used (ALBMAP), which is an update from BEDMAP and has been especially adapted for ice-sheet modelling (Le Brocq et al, 2010). The climate (temperature and surface mass balance) is provided by the regional atmospheric climate model RACMO2/ANT (Lenaerts et al, 2012b), see Section 1.3.1.

1.3 External forcing mechanisms

The second part of the input of ANICE consists of the external forcing. The atmosphere, the ocean and the bed all influence the ice sheet by being in contact with it and thus exchanging energy and mass. The exchange of energy mostly comprised in the thermodynamics of the ice sheet, while the exchange of mass is determined by the mass balance. The mass balance is made up of three parts, the basal mass balance (BMB), the surface mass balance (SMB) and ice discharge. The BMB consists of melt or freeze-on associated with the ocean water and geothermal heat. The SMB comprises precipitation, surface melt and to a lesser extent sublimation (Ligtenberg et al, 2013). On the AIS, the mass balance is dominated by accumulation (snow fall) versus ice discharge and basal melt by the ocean, with both representing about 50% of the ice loss (Depoorter et al, 2013). Ice discharge takes place through calving, which is the breaking off of chunks of ice at the edge of the ice sheet.

In Figure 1.4 the interactions between the ice sheet and its surrounding systems are shown, of which the atmospheric forcing will be discussed in the next section. This is followed by the oceanic forcing in Section 1.3.2 and the influence of the bed on which the ice rests in Section 1.3.3.

1.3.1 Atmospheric forcing

The atmospheric forcing consists of two parts: the air temperature and the surface mass balance (SMB). The SMB incorporates precipitation, be it liquid (rain) or solid (snow), and surface melt, evaporation and sublimation. The temperature and SMB are observed on the AIS by automatic weather stations that are placed on several locations on the ice sheet (Reijmer et al, 2005). However, these observations do not result in a spatially continuous field and they have only been conducted over the past few decades. Therefore, to get spatially, and temporally continuous fields of the temperature and the SMB, we use the output of the regional atmospheric climate model RACMO2/ANT (Van Meijgaard et al, 2008). This model includes a sophisticated snow model (Ettema et al, 2009) and albedo scheme (Kuipers Munneke et al, 2011) in order to realistically simulate snow-air interactions and liquid water processes

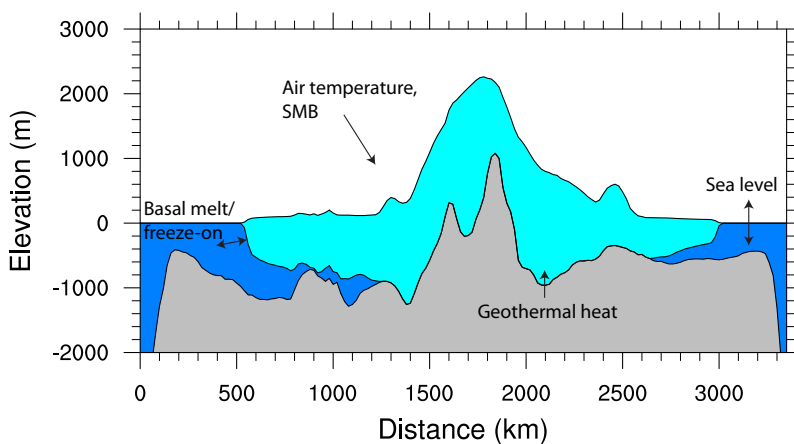


Figure 1.4: A cross-section of the present-day WAIS along a flow line, showing the topography in grey, the ocean in dark blue and the ice sheet in light blue. The different external forcing mechanisms that play a role in ice-sheet modelling are indicated.

(melt, percolation, retention, refreezing and runoff). In combination with a better horizontal grid resolution (55 km), RACMO2/ANT is therefore able to simulate a more realistic Antarctic climate than a general circulation model (GCM) (Ligtenberg et al, 2013). When forced with re-analysis data for the recent past, RACMO2/ANT has yielded realistic results over Antarctica, compared to in-situ observations (Van de Berg et al, 2006; Lenaerts et al, 2012b).

However, as RACMO2/ANT is a model as well, it requires the input of certain fields, such as temperature, wind components, surface pressure and specific humidity. These fields may be obtained from so-called re-analysis data or from a General Circulation Model (GCM). Re-analysis data are observational data (from automatic weather stations, satellites, etc) that have been analysed to derive spatially continuous fields of for instance temperature, radiation and wind. They have been re-analysed to ensure the continuity of the data in time, as this is not automatically the case because of changing observation techniques (Gibson et al, 1999). Re-analysis data only exist since 1979 and therefore only represent the PD climate. A GCM produces a climate state from combining input like insolation, greenhouse gas concentrations and Earth surface characteristics with a description of known physical processes and feedback systems. To summarise, Figure 1.5 shows a scheme of the different models and their input and output.

The RACMO2/ANT-input fields for the LGM need to be obtained from a GCM. There are many different GCMs, of which some are better suited for the Antarctic region than others. A comparison between GCMs is made in Chapter 3, from which we conclude that the HadCM3 model is best suited for the atmosphere in the Antarctic region.

RACMO2/ANT is run for about 30 years to define a climate state. The offi-

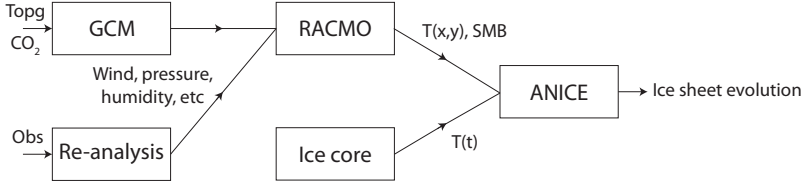


Figure 1.5: Scheme of the way different models are connected with their input and output. Data like the topography (topg) of the Earth and CO_2 -levels go into the GCM. Observations (obs) are re-analysed, this input is only used for the PD run. Both feed fields of e.g. wind, pressure and humidity into RACMO2/ANT. RACMO2/ANT supplies spatial temperature $T(x,y)$ and SMB fields to ANICE. The temporal evolution of the temperature and the SMB follows reconstructions from ice cores $T(t)$.

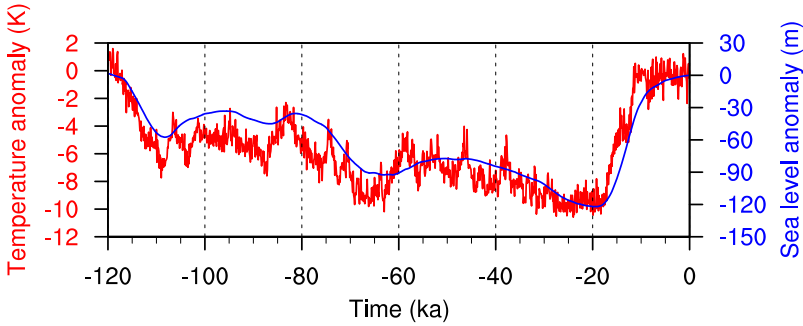


Figure 1.6: Temporal evolution of the temperature (in red) and the sea level (in blue) anomalies, with respect to the PD, from 120 kyr ago until now. The temperature reconstruction comes from the EDC ice core (Jouzel et al, 2007), the sea-level reconstruction is from the work by Bintanja and van de Wal (2008).

cial WMO (World Meteorological Organisation) definition of climate is the state of the climate system, averaged over 30 years, because 30 years is long enough to capture inter-annual variability. Temperature and SMB are then averaged over these 30 years. Running ANICE and a climate model in a synchronous mode is not possible, because, it is computationally too expensive. Therefore, we only used RACMO2/ANT for the LGM and PD temperature and SMB. To interpolate between the two states we use the ice core record of Epica Dome C (EDC, Jouzel et al (2007)), see Figure 1.6, to evolve both temperature and SMB in time. There are records obtained from other ice cores, see Figure 1.1, but the EDC-record is the most recent one. The method that we followed to achieve temporal evolution of the temperature and the SMB is described in Section 4.2.2.

To get a temperature record, the isotopic composition of the ice from an ice core is used as a proxy. Isotopes are atoms of the same chemical element with a different atomic mass. Oxygen (O) has 3 stable isotopes: ^{16}O , ^{17}O and ^{18}O , of which ^{16}O is the most abundant. Hydrogen also has 3 isotopes: ^1H (H), ^2H (deuterium, or D) and ^3H

(tritium), but tritium is unstable and can therefore not be used. The two isotopes that are most often used are ^{18}O , because it is more abundant than ^{17}O and D (Helsen, 2006). To understand how temperature can be derived from the abundance of these isotopes, one has to consider the water cycle.

Generally, water evaporates in the tropics and is transported to the north and the south where it partly rains out and eventually reaches the polar regions where the precipitation falls as snow. ^{18}O and D are heavier than their more common counterparts ^{16}O and H, and therefore the associated heavier H_2O molecules evaporate less. Furthermore, the saturation vapour pressure (the pressure exerted by a vapour in thermodynamic equilibrium with its condensed phase, solid or liquid) is less for heavy isotopes than for light ones at a given temperature, which means that heavy H_2O -isotopes condensate and rain out easier than light ones (Dansgaard, 1964). The saturation vapour pressure is also a function of temperature, in such a way that heavy isotopes condensate relatively easier than light ones when the temperature increases. In other words, the abundance of heavy isotopes is less in the precipitation when temperatures are lower.

Consequently, precipitation that falls over Antarctica is depleted in heavy isotopes with respect to lower latitudes. The amount of depletion is given by the ratio (R) between the heavy isotope and the common isotope:

$$R[^{18}\text{O}] = \frac{^{18}\text{O}}{^{16}\text{O}}, \quad R[\text{D}] = \frac{\text{D}}{\text{H}}. \quad (1.1)$$

These ratios give very small numbers and are therefore presented in parts per thousand (‰). The ratio R is compared to a standard ratio (for water isotopes this is the Vienna Standard Mean Ocean Water, VSMOW) to give the $\delta^{18}\text{O}$ and δD values (see e.g. WAIS Divide Project Members, 2013):

$$\delta^{18}\text{O} = \left(\frac{R[^{18}\text{O}]_{\text{sample}}}{R[^{18}\text{O}]_{\text{standard}}} - 1 \right) \cdot 1000\text{‰}, \quad \delta\text{D} = \left(\frac{R[\text{D}]_{\text{sample}}}{R[\text{D}]_{\text{standard}}} - 1 \right) \cdot 1000\text{‰}. \quad (1.2)$$

The spatial relation that can be found between $\delta^{18}\text{O}$ and temperature has in the past been assumed to be constant over time (e.g. Jouzel et al, 1987). However, the relation between $\delta^{18}\text{O}$ and temperature can be obscured by changes in the water vapour source area, the seasonal distribution of precipitation and by changes in the strength of the temperature inversion (Helsen, 2006). Like $\delta^{18}\text{O}$, there is a similar relation between δD and temperature. Therefore, a linear relationship exists between $\delta^{18}\text{O}$ and δD . The deviation from that line has been found to be particularly sensitive to changes in the moisture source conditions. This deviation is called the deuterium excess and is given by (Dansgaard, 1964):

$$D_{\text{excess}} = \delta\text{D} - 8\delta^{18}\text{O}. \quad (1.3)$$

For instance, the temperature reconstruction from the Vostok ice core was calculated by (Petit et al, 1999):

$$\Delta T_I = (\Delta \delta D_{ice} - 8 \Delta \delta^{18} O_{sw}) / 9, \quad (1.4)$$

where ΔT_I is the temperature anomaly above the inversion level (where precipitation forms), which is related to the surface temperature through $\Delta T_I = 0.67 \Delta T_s$, $\Delta \delta D_{ice}$ is the ice deuterium isotope ratio anomaly, and $\Delta \delta^{18} O_{sw}$ is the globally averaged sea water $\delta^{18} O$ anomaly. The division by 9 comes from the spatial deuterium isotope/temperature gradient of 9‰ per °C in the region where the ice core was drilled (Petit et al, 1999).

We also use the EDC temperature record to interpolate between the LGM and PD SMB in time, since the SMB is mainly dependent on temperature. Firstly, melt, sublimation and other phase changes as well as the fraction of precipitation that falls as snow are all determined by the temperature of the air. Moreover, even the amount of precipitation, the most important part of the SMB, is dependent on temperature through the Clausius-Clapeyron relation (Bintanja et al, 2002). This relation describes how the saturation vapour pressure increases when temperature increases. As a result of this, air can hold more moisture at higher temperatures, and hence more precipitation occurs. Both temperature and SMB are fed into ANICE as yearly averages, since it requires more detailed modelling to incorporate seasonal cycles in both the input fields and the ice-sheet model itself. Furthermore, it does not influence the output of the model significantly when an ice sheet is modelled over tens of thousands of years.

In Chapter 5 the possible future evolution (until 2100) of the AIS is studied by using different temperature and sea-level forcings from the fifth assessment report of the IPCC Collins et al (2014); Church et al (2014). These forcings are produced by GCMs that use four different emission scenarios. These scenarios are called RCP (Representative Concentration Pathway) 2.6, 4.5, 6.0 and 8.5. Each specifies concentrations and corresponding emissions of greenhouse gases and aerosols. The number represents the radiative forcing (in $W m^{-2}$) with respect to pre-industrial values (i.e. before 1900). The higher the radiative forcing, the higher the global mean temperature. As higher temperatures lead to more ice melt (especially on the Northern Hemisphere), sea level will also rise more for the higher RCP-scenarios.

1.3.2 Oceanic forcing

The ocean exerts an influence on the AIS through the processes of basal melt and freeze-on, sea-level change and facilitating ice to float and to calve. Changes in sea level have a large effect on the amount of ice in West Antarctica because its bed elevation is very low (mostly below PD sea level, see Le Brocq et al (2010)), see Section 1.1. In light thereof, sea-level change is a key ingredient to the modelling of the evolution of the AIS.

Sea-level change can be inferred from deep-sea sediment cores. These cores are taken from the bottom of the ocean and sea-level information is derived from the (fossilised) shells of benthic foraminifera (e.g. Emiliani, 1955). Benthic foraminifera are small animals that live on the ocean floor (hence the name benthic) that build their calcite shells from calcium carbonate (CaCO_3). The oxygen isotope ratios in these shells give information about the (deep ocean water) temperature, but also about global sea level. This is because lower air temperatures lead to the build up of ice sheets and hence there is less water in the oceans. Vaporisation favours light isotopes so the left-over water is enriched in $\delta^{18}\text{O}$ when sea level is low, and ice volume is high (De Boer, 2012). The sea-level record used in this research has been constructed by using an ice-sheet model with an ocean-temperature model by Bintanja and van de Wal (2008). The sea-level record from 120 kyr ago until now is shown in Figure 1.6.

Next to sea-level change, basal melt also influences the advance and retreat of ice sheets. Basal melt is simply the result of the ocean water being so much warmer than the ice that it leads to melt. If the water is not warm enough when it comes in contact with the cold ice, the temperature drops to the point that the water freezes onto the base of the ice. The freezing temperature of water is dependent on its salinity and the pressure it experiences (Knauss, 1997). Non-saline water at sea-level pressure freezes at 0°C , or 273.15 K. At the base of the major ice shelves, typically 200-500 metres below sea level, the pressure is much higher, and therefore the freezing temperature is 0.1 to 0.4 degrees higher. The salt in the ocean water causes it to freeze at about 2 degrees lower temperatures.

Another process influencing the extent of the ice sheet is ice discharge, which is made possible by the presence of water at the edge of the ice sheet. The ice is discharged through calving. Calving happens because the outer parts of the ice shelf flow more rapidly than the inner parts, inducing a strain on the floating ice (Benn et al, 2007). When this strain is large enough, crevasses form in the shelf. When the strain increases these crevasses grow and eventually the ice is ripped and a chunk of ice is broken off. The calving front (the edge of the ice shelf) has a typical ice thickness of about 200 m, and the large ice shelves regularly experience calving events producing tabular icebergs of up to 5000 km^2 (Joughin and MacAyeal, 2005).

1.3.3 Influence of the bed

The AIS is, for the largest part, grounded on bedrock. The bedrock responds to changes in ice thickness, but the ice sheet also responds to the bedrock. Firstly, the altitude and the slope of the bed play an important role. Where the bed is higher, the ice is less influenced by the ocean and the steeper the slope, the stronger the gravitational pull on the ice. Especially the WAIS is vulnerable for changes in sea level, because a major part of its bed is currently below sea level. Therefore, the height of the bed has a significant influence on this part of the ice sheet (Pollard and DeConto, 2009). Furthermore, where the bed slopes downward inland an ice sheet

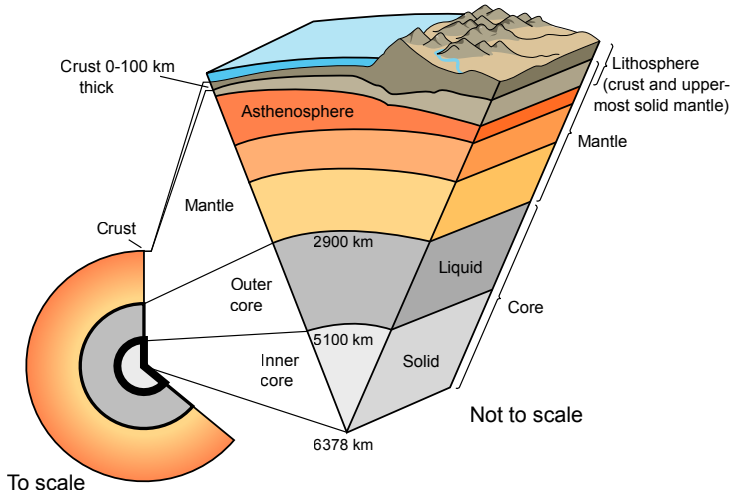


Figure 1.7: Cutaway diagram of Earth's internal structure (to scale), with an inset showing a more detailed breakdown of the structure (not to scale). This figure was taken from USGS (2013)

might be unstable as explained in Section 1.1.

The altitude and slope of the bed react, through GIA, to changes in the ice loading. This happens because the density of the bedrock is only 3.4 times that of ice, so every 100 metres of ice added to the ice sheet make the bedrock sink for more than 30 metres. When the ice is then removed, the bedrock will rebound to its original state. GIA consists of two parts: isostatic adjustment due to elastic rebounding of the lithosphere (see Figure 1.7) and viscous rebound because of the mantle material flowing back. The elastic adjustment is instantaneous, but the viscous deformation takes thousands of years. When modelling an ice sheet from the LGM or the Eemian until the present, both components of the geodynamic adjustment have to be taken into account. Many uncertainties remain as to how fast the bed responds to ice loading because little is known about the thickness and rigidity of the Earth's lithosphere underneath the AIS, except the lithosphere being thinner and less rigid underneath the WAIS than underneath the EAIS (Morelli and Danesi, 2004). The speed at which the bed responds to ice loading depends on the thickness of the Earth's crust and the structure of the mantle, which may be modelled as well (Huerta and Harry, 2007). When the Earth underneath an ice sheet is modelled, the history of the ice sheet serves as a boundary condition, but the bed serves as a boundary condition for ice-sheet modelling. The ice-dynamical model is therefore coupled to a simple geodynamical model to capture this feedback system. This model is described in more detail in Section 2.4.

Secondly, in the interior of the Earth heat is generated by nuclear processes. This leads to a geothermal heat flux at the Earth's surface which is typically enough

to melt 5 mm of ice per year underneath the entire ice sheet. Although this order of magnitude for the geothermal heat flux is commonly accepted, there are large uncertainties. The two mostly used datasets are those of Shapiro and Ritzwoller (2004) and Fox Maule et al (2005). Although there are some substantial differences between these datasets, they do agree that the heat flux is higher underneath the WAIS than underneath the EAIS because West Antarctica is a region with more tectonic activity. However, Shapiro and Ritzwoller (2004) deduced peaks in the heat flux further north of the Transantarctic Mountains than Fox Maule et al (2005). We chose to use the dataset by Shapiro and Ritzwoller (2004) because their method is more elaborately described and validated.

1.4 Ice dynamics

The evolution and the ice dynamics of an ice sheet are determined by its mass balance, because it regulates where the ice accumulates and recedes. The mass balance depends partly on the velocity of the ice. For instance, calving is largely determined by stresses in the ice and therefore the ice velocity. There are two types of ice movement, one is caused by deformation of the ice itself and the other is caused by basal sliding of the total ice column (see Figure 1.8).

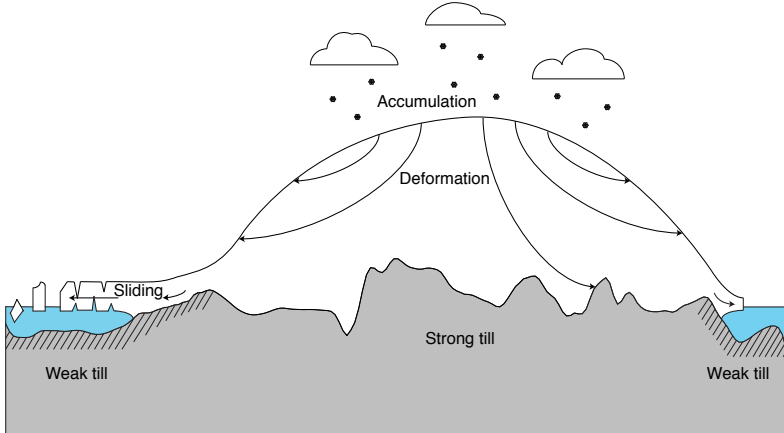


Figure 1.8: A schematic cross-section of an ice sheet, showing the ice dynamics. Snow accumulates on the ice sheet and transforms into ice through compaction. The ice moves slowly through deformation following the long curved arrows or faster through sliding when the till layer is weak. Ice velocities near the grounding line are generally lower than velocities further outward on the ice shelf, which is why crevasses form and the ice calves.

In the case of sliding the material of which the bed consists plays a large role, as does the amount of liquid water available at the bed. When the bed consists of hard rock, ice may start sliding over it when a film of liquid water lubricates the interface.

This way of sliding is limited to temperate basal conditions, as ice may be frozen to the bedrock when temperatures are too low for liquid water to exist at the ice base. When the bed is weak (consisting of sand or gravel), it is more easily deformed by the ice flow than hard rock, and the amount of sliding is not only determined by the amount of water present at the ice base (the basal water pressure), but also by the thickness and rheology of the weak layer. In ANICE, the sliding velocity of the ice is dependent on temperature, water pressure, and bed characteristics (see also Section 2.5 for a mathematical description). However, as the bed material beneath the AIS is mostly unknown, the assumption is that the bed is weaker where it is below sea level due to its marine origin. This is a very crude assumption and it remains a source of debate how sliding should be parametrised in ice-dynamical models.

On large parts of the EAIS, the conditions at the base are not suitable for sliding and the ice will move due to deformation. Ice deformation arises from gravity acting on the ice, pulling the ice towards the bed. On a sloping bed, the ice velocity will have a component parallel to the bed (down slope), and a shear stress is invoked by the friction between the bed and the ice, which is called basal drag. Two other stress components play a role in ice dynamics. The first is side drag which only becomes important when ice is moving past valley walls for instance. The second is normal stress, in the direction of gravity, as a result of the ice's own weight. Normal stress is usually much smaller than shear stress, except when the ice is floating freely in water or sliding, as basal drag is almost zero then.

Stress gradients cause gradients in the ice velocity. For instance, stress gradients may exist in the vertical direction when basal drag is present, but there is no surface stress. As a result the ice velocity will be close to zero near the bed and at its maximum at the surface. This is accompanied by the deformation of the ice. Deformation occurs in two ways: shearing and stretching, see Figure 1.9 and may be either elastic or plastic. Elasticity means that application of a finite force leads to a new steady state and when the force is removed the material will return to its original state. Plasticity means that the material under consideration continues to deform when a constant force is applied and will not return to its original state once the force is removed. Ice is subject to both kinds of deformation, for instance, a rapidly varying force may cause elastic deformation, while a slower varying force may cause plastic deformation.

The deformation of ice and the ice velocity depend on its rheology (hardness/stiffness) and therefore on its temperature. Warmer ice is softer and easier to deform. The ice temperature depends on advection, diffusion, frictional heating and heating due to refreezing. Advection is the transport of heat by movement of the ice itself and diffusion is the exchange of kinetic energy between individual particles. Frictional heating is caused by basal drag and side drag, but also by velocity gradients inside the ice (internal friction). A more detailed description of the thermodynamics in ANICE is given in Section 2.6.

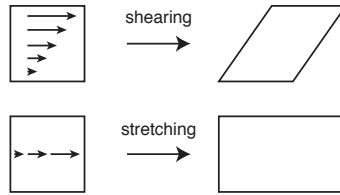


Figure 1.9: *The effects of shearing and stretching on a block of ice, with the accompanying velocity field drawn in the blocks on the left.*

1.5 Validation

Comparing model output to observations is an essential part of this study. There are different kinds of geological observations that give information about the location of the grounding line, about when a certain location was ice covered or even about how thick the ice was. Furthermore, the PD ice sheet is well-mapped, and modelling it correctly is crucial for the model to be trustworthy. The PD ice sheet is observed through satellites, radar and seismic sounding. Data from these sources have been combined in a comprehensive dataset called BEDMAP (Lythe et al, 2001). In this thesis an update of the BEDMAP dataset is used, which has been presented as the ALBMAP dataset (Le Brocq et al, 2010).

Geological observations have different sources. Firstly, dating animal remains (penguin guano or bones, seal skin or hairs, snow petrel nests and mollusc fossils, see Figure 1.10a) gives information about where animals could have lived in the past. For example, penguin and seal remains from old rookeries indicate that open ocean water was not too far away at the time the rookeries were built and snow petrel nest sites are ice-free. On the other side, molluscs, a type of shelled invertebrates, need at least 1-2 m of water depth to survive. Thus animal remains give clues about whether there was open water or ice in the past.

Secondly, marine sediment cores (Figure 1.10b) record transitions in the sediments that occur when the grounding line retreats or advances and with the onset of open marine conditions. This is because sediments underneath grounded ice (sub-glacial sediments) are different from those underneath floating ice (glacial-proximal sediments). These sediments are both different from sediments under open water. Thus, stratigraphic analysis of the sediments and dating of the boundaries between different types of sediments give information on the timing of grounding-line retreat and the onset of open marine conditions.

Finally, glacially transported boulders (Figure 1.10c) and glacially scoured bedrock (Figure 1.10d) designate paleo-ice surface elevation relative to the PD ice free surface. When an ice sheet retreats bedrock becomes exposed and rocks that were entrained within the ice (called erratics) are left behind. The time of exposure of the bedrock and the erratics can be determined because they have, since their

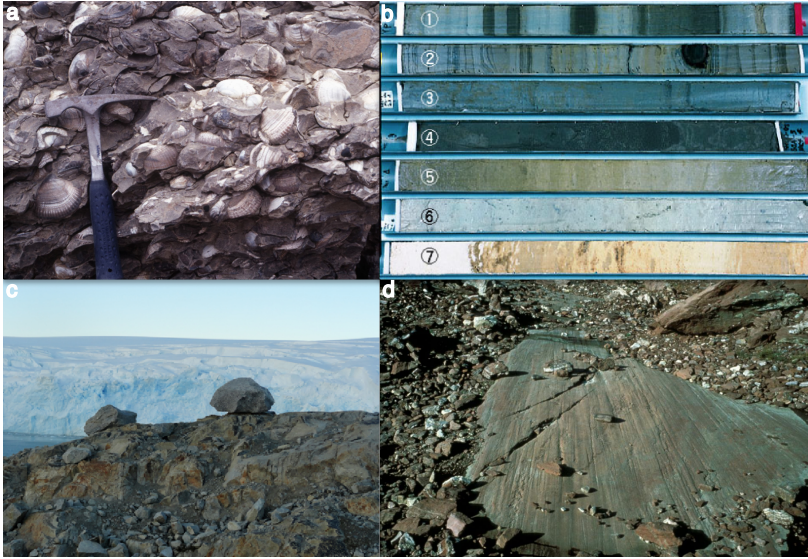


Figure 1.10: Four ways of determining past ice extent: a) mollusc fossils (from Moody, 2007), b) marine sediment cores (number 1-6 are taken in Japanese and Chinese seas, number 7 is taken in the Southern Ocean, from Center for Advanced Marine Core Research, Kochi University (2006)), c) erratics (from Herrmann, 2012) and d) scoured bedrock (from Cox, 2012).

emergence, been exposed to cosmic radiation. When cosmic rays interact with the surface of rock, radioactive nuclides are formed (e.g. ^{10}Be and ^{26}Al). The concentration of the nuclides yields the length of time the rock has been exposed. The difference between the elevation at which the bedrock is scoured or the erratic is deposited and the PD bedrock elevation gives the paleo-ice thickness.

The observations used in this thesis to verify model output that is not from the PD come from a database called AntICEdat (Briggs and Tarasov, 2013), which has been specifically compiled to validate ice-dynamical model results.

1.6 Outline

This thesis starts with a detailed physical description of the ice-dynamical model ANICE in Chapter 2. In Chapter 3 an intercomparison of GCMs is conducted to find the GCM that models the Antarctic region best over the period LGM to PD, with respect to temperature and precipitation. This GCM (HadCM3) has been selected to provide the regional climate model RACMO/ANT with e.g. wind, pressure and humidity fields for the LGM. The re-analysis data from ERA-interim have been used for the PD climate simulation of RACMO2/ANT. The temperature and SMB output from RACMO2/ANT for the LGM and the PD have then been used to provide ANICE with a climatological forcing for sensitivity experiments of which the

results are presented in Chapter 4. In these sensitivity experiments the effect of five different parameters on the evolution of the AIS is tested. These five parameters are related to the sliding parameterisations and the response of the bed to ice loading. Furthermore, a reference run has been defined that simulates the LGM state of the AIS best. This LGM state has then been used to investigate the influence of using different climate reconstructions on the evolution of the AIS, as described in Chapter 5. The model results are validated in detail by using the AntICEdat-database. Also, a short look into the future (until 2100) of the ice sheet is presented here by investigating the effect of different scenarios of temperature and sea-level rise.

Model description

2.1 Introduction

As stated in Chapter 1, the ice-dynamical model ANICE is able to evaluate the evolution of an ice sheet, based on physical principles. This chapter describes the physical basis of several parts of the model that are relevant to this thesis. Section 2.2 starts with the description of the computational grid of ANICE and a short history of its development and how it has been used in other research projects. Section 2.3 deals with the modelling of the ocean, i.e. the basal mass balance underneath ice shelves and calving. The effect which the ice loading has on the underlying bedrock, which then affects the ice sheet by a feedback system is described in Section 2.4. Section 2.5 describes how ice velocities are calculated by means of the Shallow Ice Approximation (SIA) and the Shallow Shelf Approximation (SSA). Because the ice velocity depends strongly on the temperature regime in the ice, Section 2.6 presents the thermodynamics used in ANICE. The different components of the model are linked together in Section 2.7.

2.2 General background of the model

ANICE is based on the models of Huybrechts (1990) and Van de Wal (1999), after which it has been further developed by Reerink (2013); De Boer et al (2013); Maris et al (2014). The model has been used for a number of studies regarding the Northern Hemisphere ice sheets, like the North American ice sheet (Bintanja and van de Wal, 2008), the Eurasian ice sheet (Van den Berg et al, 2008) and the Greenland ice sheet

(Helsen et al, 2012). Additionally, in De Boer et al (2013) ANICE is used to simulate global ice volume and in De Boer et al (2014a) to simulate Antarctic ice volume variability over the past 5 million years. This thesis adds to the research already done with ANICE by focussing on the last 20000 years of the evolution of the Antarctic Ice Sheet (AIS).

ANICE is a 3D finite difference model, with a horizontal grid spacing of 20 by 20 km. Horizontally, the grid consists of 281x281 points, which comprises the AIS and a large part of the Southern Ocean, see Figure 1.3 for the model domain, which runs from 90°S until approximately 54°S. The vertical levels in the model are split between levels in the ice, in the bedrock and in the ocean. The ice thickness is divided into 14 layers in the vertical, with a spacing of 10 % of the ice thickness at the top and 1% of the ice thickness at the bottom to ensure a higher vertical resolution at the base of the ice sheet. The bedrock is modelled until a depth of 1500 metres, divided into five evenly spaced levels of 300 metres each. The ocean has a vertical resolution of 100 metres, and is modelled till a depth of 3000 metres.

2.3 Oceanic forcing

2.3.1 Basal mass balance

The basal mass balance (BMB) of floating ice is determined by the difference between the water temperature (T_o) and the freezing temperature (T_f) at ice shelf depth, following Holland and Jenkins (1999):

$$\text{BMB} = F_{melt} \cdot \rho_o \cdot c_{p_o} \cdot \gamma_T \cdot (T_o - T_f) / (L \cdot \rho_i) , \quad (2.1)$$

where $F_{melt} = -5.0 \cdot 10^{-3} \text{ m s}^{-1}$ is the melt parameter, $\rho_o = 1028 \text{ kg m}^{-3}$ is the ocean-water density, $c_{p_o} = 3974 \text{ J kg}^{-1} \text{ K}^{-1}$ is the specific heat capacity of the water, $\gamma_T = 10^{-4} \text{ m s}^{-1}$ is the thermal exchange velocity, $L = 3.335 \cdot 10^5 \text{ J kg}^{-1}$ is the latent heat of fusion and $\rho_i = 910 \text{ kg m}^{-3}$ is the ice density. The ocean temperature (T_o) is given by:

$$T_o = (\theta_o - 1.7) + 0.3 \cdot \Delta T - 0.12 \cdot 10^{-3} \cdot D_{shelf} . \quad (2.2)$$

Here, θ_o is the ocean potential temperature, ΔT is the air-temperature anomaly with respect to the present-day and D_{shelf} is the depth of the bottom of the ice shelf. The ocean potential temperature is provided by ECHAM53, from the PMIP2 project (Braconnot et al, 2007). A cross section of θ_o at 300 m depth is shown in Figure 2.1. ECHAM53 was chosen because both the vertical and horizontal patterns match observations from the WOCE-atlas (Orsi and Whitworth III, 2004). However, the mean value of θ_o is too high by about 1.7 degrees, and the coarse resolution (which is already higher than for most other GCMs) disables the output of θ_o beneath the innermost ice shelves. Therefore, the data have been interpolated for

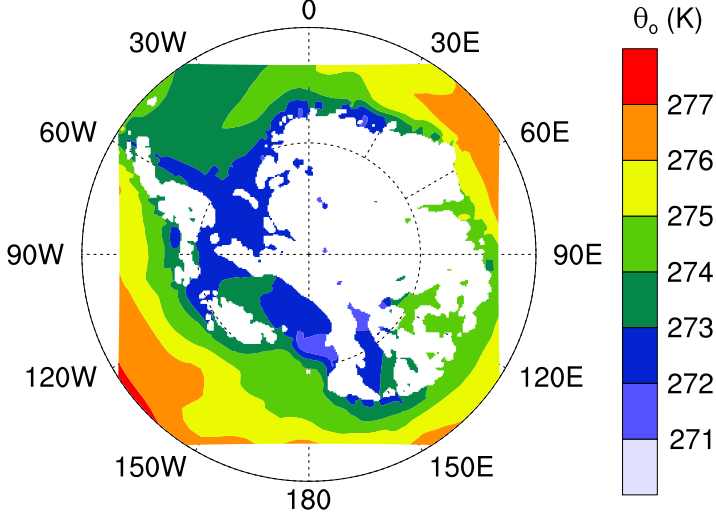


Figure 2.1: Ocean potential temperature at 300 m depth, as given by ECHAM53 (Braconnot et al, 2007). In the areas where no water is present, a mask has been placed (transparent areas in the figure).

these regions by simple inverse distance interpolation. The temperature anomaly with respect to the present (ΔT) is retrieved from an ice core record, see Chapters 4 and 5. Furthermore, to convert potential temperature to real temperature, a lapse rate is used, multiplied by the depth of the ice shelf D_{shelf} . The mean lapse rate in water is $0.12 \cdot 10^{-3} \text{ K m}^{-1}$ (Knauss, 1997). T_f in Equation 2.1 is the freezing temperature (Holland and Jenkins, 1999):

$$T_f = T_0 + 0.0939 - 0.057 \cdot S + 7.64 \cdot 10^{-4} \cdot D_{shelf}. \quad (2.3)$$

Here, T_0 is the triple point of water at 273.16 K and S is the salinity of the ocean water, equal to 34 psu in the Southern Ocean.

2.3.2 Calving

The AIS loses a large part of its mass (around 50%) through calving. Furthermore it has been suggested that floating ice provides buttressing for the flow of grounded ice. It is therefore important to model a realistic calving rate. In ANICE three mechanisms to model calving can be switched on or off:

- Calving at the edge of the continental shelf
- Calving every few hundreds of years if the thickness of the ice shelf is below a certain threshold

- A scheme that is based on horizontal strain rates in the ice shelf, due to the divergence in the velocity field

It has been shown in the literature (Denton and Hughes, 2002; Livingstone et al, 2012; Whitehouse et al, 2012) that the ice sheet and ice shelves have not extended beyond the edge of the continental shelf. Therefore, we assume that ice shelves will calve at the edge of the continental shelf, which is taken to be at $H_b = -2200$, with H_b the bed elevation.

The ice at the calving fronts around the AIS is usually a few hundreds of metres thick. Therefore, a second possible calving description is to cut off all the floating ice that is thinner than a certain threshold value (further on referred to as threshold calving). However, if this is done at every time step of the model (typically 1/3 year), unrealistically high calving rates are modelled. Therefore, we assume that this threshold calving happens in 'events' every few hundreds of years. The grounding-line position is not greatly influenced by the exact calving rate, and in ANICE we adopt calving at a threshold thickness of 250 m, occurring at 300 year intervals as this leads to grounding-line and calving-line positions that resemble the results of Pollard and DeConto (2012b), see below.

Physically, calving is thought to be dominated by (horizontal) strain rates that cause crevasses to develop in parts of the floating ice, which finally break off from the main shelf. These strain rates are due to divergence in the ice velocity field. In ANICE a divergence calving scheme has been implemented, following Pollard and DeConto (2012b), who show that their calving mechanism leads to realistic results regarding ice-sheet evolution. First, the divergence of the floating ice-shelf points is calculated as:

$$\nabla \cdot \vec{V}_{SSA} = \frac{\partial \bar{u}}{\partial x} + \frac{\partial \bar{v}}{\partial y}, \quad (2.4)$$

where \bar{u} and \bar{v} are the (vertically averaged) SSA-velocities (see section 2.5.2) in the x- and y-direction respectively. This divergence is calculated for all floating ice points, except the points at the ice shelf edge. The divergence is then passed on to the points at the edge of the ice shelf through nearest-neighbour value propagation. The calving rate (in m/yr) is given by

$$\text{CMB} = (1 - w_c) \cdot 30 + w_c \cdot F_c \cdot \max[\nabla \cdot \vec{V}_{SSA}, 0] \cdot H_i / dx. \quad (2.5)$$

The weighting factor w_c is dependent on the ice thickness at the edge (H_i), and equal to $\min(1, H_i/250)$. This way, when H_i is much smaller than 250 m the $(1 - w_c)$ -term will be dominant, and the calving rate will be at least 30 m/yr. When H_i is larger than 250 m only the $F_c \cdot \max[\nabla \cdot \vec{V}_{SSA}, 0] \cdot H_i / dx$ will count. Here, F_c is a scaling coefficient, set to $3 \cdot 10^5$ m in ANICE, and the term $F_c \cdot \max[\nabla \cdot \vec{V}_{SSA}, 0]$ represents the horizontal erosion rate. As we want to evaluate the change in ice thickness this term is multiplied by $H_i \cdot dx/dx^2 = H_i/dx$. The grounding line

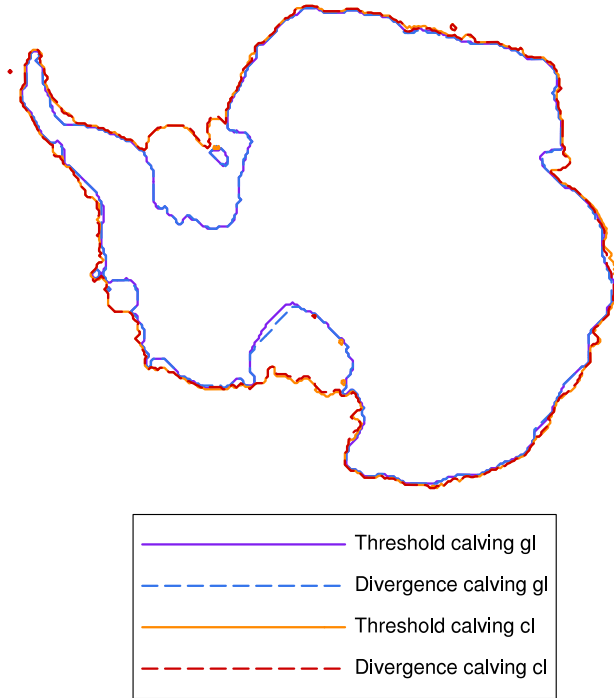


Figure 2.2: Grounding line (gl) and calving line (cl) positions at the PD for the standard run in Chapter 4 for the threshold and the divergence calving schemes, both in combination with calving at the continental edge.

and calving line position for this calving scheme are shown in Figure 2.2, together with the grounding line and calving line for the threshold calving scheme. It can be concluded from this figure that the difference between divergence calving and the simpler threshold calving (with a threshold thickness of 250 m, every 300 years) is minimal. Therefore, we use the threshold calving scheme in our research.

2.4 The bedrock response to ice loading

The bedrock model in ANICE is an Elastic Lithosphere, Relaxed Asthenosphere (ELRA) model and is based on Le Meur and Huybrechts (1996). The bedrock is in this case approximated by a thin, elastic lithosphere, controlling the geometric shape of a deformation, floating on a more viscous asthenosphere, which governs the time-dependent characteristics of the deformation of the Earth.

For an elastic lithosphere, not only the loading above a certain point on the lithosphere is taken into account, but also the contributions of more remote locations. The downward bedrock deformation w , created by a point load m for a (floating)

elastic plate is a solution of:

$$D\nabla_h^4 w = m - \rho_a g w. \quad (2.6)$$

Here, D is the flexural rigidity, ρ_a is the asthenosphere density (3300 kg m^{-3}) and g is the gravitational constant (9.81 m s^{-2}). Consequently, $\rho_a g w$ is the upward buoyancy force exerted on the deflected part of the lithosphere. The deformation at a normalised distance $x = r/L_r$ from the point load is then given by:

$$w(x) = \frac{mL_r^2}{2\pi D} \chi(x), \quad (2.7)$$

with $\chi(x)$ a Kelvin function of zero order at x , r the real distance from the load m and L_r the radius of relative stiffness, given by

$$L_r = \left(\frac{D}{\rho_a g} \right)^{1/4}. \quad (2.8)$$

In this way, a load will cause a depression within a distance of four times L_r with a minimum at the location of the load. Beyond this distance a small bulge appears. Since Equation 2.6 is a linear differential equation, the total deflection at each point is simply calculated as the sum of the contributions of all neighbouring points within a distance of about 6 times L_r . Typical values for the flexural rigidity D are 10^{24} - 10^{25} Nm (Stern and ten Brink, 1989), with smaller values for thinner parts of the lithosphere, and 75 to 130 km for L_r .

Equation 2.7 holds for an instantaneous reaction of the bedrock to a load, but in reality the adaptation to a load is delayed due to the viscosity of the asthenosphere underneath the lithosphere. We assume that the bedrock adjusts exponentially to a new loading situation. Furthermore, we state that the speed of adjustment is proportional to the difference between the equilibrium profile $h_0 + w$ (where h_0 is the initial bedrock profile) and the current profile h and inversely proportional to a time constant τ :

$$\frac{dh}{dt} = \frac{1}{\tau}(w + h_0 - h), \quad (2.9)$$

where w is the bedrock deflection, given by Equation 2.7, h and h_0 are positive upward and τ is the Maxwell relaxation time or e-folding response time. The relaxation time can be calculated from $\tau = \eta/G$ (Ranalli, 1995), where η is the viscosity of the upper part of the asthenosphere, in the range of $0.5 - 4 \cdot 10^{21}$ Pa s (Forte and Mitrovia, 2001) and G is the shear modulus, ranging from 2 to $11 \cdot 10^{10}$ Pa. These numbers yield relaxation times between 150 and 6000 years approximately.

Combining Equation 2.9 with Equation 2.7 yields a differential equation:

$$\frac{dh}{dt} = \frac{1}{\tau} \left(\sum_{i,j} \left(\frac{m_{i,j} L_r^2}{2\pi D} \chi(x_{i,j}) \right) + h_0 - h \right), \quad (2.10)$$

which is solved in ANICE. Here, the sum is taken over all i, j within a distance of about six times L_r . The loading m is equal to the weight of the water column where there is no ice, or where the ice is floating $m = (H_o - H_b) \cdot \sigma \cdot \rho_o \cdot g$, with $H_o - H_b$ the height of the water column (ocean-water level minus the bedrock elevation) and σ the surface area of the column, equal to 400 km^2 . Where the ice is grounded, m is equal to the weight of the ice: $m = H_i \cdot \sigma \cdot \rho_i \cdot g$.

2.5 SIA and SSA

To calculate the ice velocities in ANICE we assume the ice to be shallow, i.e., the horizontal scales are much larger than the vertical scales. This is expressed in the shallow ice approximation (SIA) and the shallow shelf approximation (SSA). The assumption of shallowness leads to simplifications in the stress tensor, i.e. for the SIA the shear stresses in the horizontal plane are supported by the basal drag and for the SSA the horizontal velocities do not change with depth. The SIA and SSA velocities in ANICE are based on Glen's flow law (Glen, 1958). For the ice shelves, the ice velocity is equal to the SSA velocity, whereas for grounded ice the total ice velocity is the sum of the SIA and the SSA velocity.

2.5.1 SIA

The SIA velocity is given by (Hutter, 1983):

$$\vec{V}_{SIA} = -2(\rho_i \cdot g)^n \cdot |\nabla H_s|^{n-1} \cdot \nabla H_s \int_b^z E_{SIA} \cdot A(T^*) \cdot (H_s - z)^n d\zeta, \quad (2.11)$$

where ∇H_s is the surface slope and ζ is the scaled vertical coordinate running from the bed (b) to height z . $A(T^*)$ is the flow-rate factor, dependent on the temperature, which is corrected for pressure melting. E_{SIA} is the SIA enhancement factor. This factor determines by how much the deformational flow of the ice is enhanced. This is necessary because the velocity calculations of both the SIA and the SSA make use of Glen's isotropic flow law, while ice is a highly anisotropic material (Ma et al, 2010). The enhancement factors are different for grounded ice and sliding or floating ice because SIA velocities are generally underestimated and SSA velocities are overestimated.

2.5.2 SSA

The SSA velocity equations are given by (Morland, 1987):

$$\frac{\partial}{\partial x} \left[2\mu H_i \left(2\frac{\partial u}{\partial x} + \frac{\partial v}{\partial y} \right) \right] + \frac{\partial}{\partial y} \left[\mu H_i \left(\frac{\partial u}{\partial y} + \frac{\partial v}{\partial x} \right) \right] + \tau_{b,x} = \rho g H_i \frac{\partial H_s}{\partial x} \quad (2.12)$$

and,

$$\frac{\partial}{\partial y} \left[2\mu H_i \left(2\frac{\partial v}{\partial y} + \frac{\partial u}{\partial x} \right) \right] + \frac{\partial}{\partial x} \left[\mu H_i \left(\frac{\partial v}{\partial x} + \frac{\partial u}{\partial y} \right) \right] + \tau_{b,y} = \rho g H_i \frac{\partial H_s}{\partial y}. \quad (2.13)$$

Here, μ is the vertically averaged viscosity:

$$\mu = \frac{1}{2(E_{SSA} \cdot \bar{A})^{1/n}} \left[\left(\frac{\partial u}{\partial x} \right)^2 + \left(\frac{\partial v}{\partial y} \right)^2 + \frac{\partial u}{\partial x} \frac{\partial v}{\partial y} + \frac{1}{4} \left(\frac{\partial u}{\partial y} + \frac{\partial v}{\partial x} \right)^2 \right]^{\frac{1-n}{2n}}, \quad (2.14)$$

with E_{SSA} the SSA enhancement factor.

In Equation 2.14, \bar{A} is the vertical mean of $A(T^*)$, u and v are the SSA velocities in the x- and y-direction respectively, and $\tau_{b,x}$ and $\tau_{b,y}$ are the basal shear stresses in the x- and y-direction. The basal shear stress is dependent on the ice velocity, but also on the properties of the till, i.e., the bed material underneath the ice, which deforms when the ice moves over it. Thus, τ_b is determined as a function of the basal yield stress and the basal sliding velocity, as in Bueller and Brown (2009) and is given by:

$$\tau_b = \tau_c \cdot \frac{|V_{SSA}^{q-1}|}{u_{threshold}^q} \cdot \vec{V}_{SSA}, \quad (2.15)$$

where $u_{threshold}$ is a threshold velocity of 100 m/yr, $q = 0.3$ is a power-law parameter for basal stress and τ_c is the yield stress:

$$\tau_c = (\tan \phi) \cdot (\rho_i g H_i - p_w). \quad (2.16)$$

Here, ϕ is the till friction angle and p_w is the pore water pressure:

$$p_w = 0.96 \cdot \lambda_p \cdot \rho_i \cdot g \cdot H_i, \quad (2.17)$$

where λ_p is a scaling factor between 0 and 1 which represents the pore water pressure and is 1 when the ice is resting on bedrock below sea level because the pores in the till are assumed to be saturated with water there. λ_p is then scaled with the height above sea level up until 1000 m. Above 1000 m λ_p is equal to 0. The till

friction angle in Equation 2.16 (ϕ) is parameterised by:

$$\phi = \begin{cases} \phi_{min} & \text{if } H_b \leq -1000, \\ \phi_{min} + (\phi_{max} - \phi_{min}) \cdot \left(1 + \frac{H_b}{1000}\right) & \text{if } -1000 < H_b < 0, \\ \phi_{max} & \text{if } 0 < H_b. \end{cases} \quad (2.18)$$

Thus, ϕ_{min} determines the sliding below -1000 metres and partly between -1000 and 0 metres, and henceforth controls the sliding on large parts of the WAIS. The assumption here is that the till is weaker when situated below sea level and therefore the friction angle is smaller, and sliding more dominant.

2.6 Thermodynamics

Before starting a simulation, the model is run to a thermodynamic equilibrium, which means that the ice temperature is in equilibrium with the surface temperature and ice velocity. This is achieved by keeping the surface or geometry of the ice sheet fixed and by applying a constant climate forcing in time. The thermodynamics in ANICE are described by the thermodynamical equation, which is discussed in this section (based on Reerink (2013)). There are five processes that determine the thermal state of an ice sheet:

1. Molecular diffusion
2. Energy fluxes entering the ice sheet through its boundaries due to thermal contact with air, water and bedrock
3. Radiation penetrating the ice sheet
4. Friction due to the movement of ice, leading to local internal heating
5. Phase transitions

Firn compaction and refreezing of water due to radiation penetration in the snow pack are neglected in ANICE. The thermodynamical equation is given by:

$$\frac{dE}{dt} = -\nabla \cdot \vec{\phi}_q + \Phi, \quad (2.19)$$

with E the internal energy, $\vec{\phi}_q$ the heat flux in $\text{Jm}^{-2}\text{s}^{-1}$, and Φ the rate of internal heat production in $\text{Jm}^{-3}\text{s}^{-1}$. As the kinetic contribution to the internal energy is negligible, only the thermal part of the internal energy is kept:

$$E = \rho_i c_i T_i. \quad (2.20)$$

Here, T_i is the ice temperature and c_i is the specific heat capacity which is dependent on the temperature through an empirical relation (Zwinger et al, 2007):

$$c_i = c_0 + c_\Delta(T_i - T_0), \quad (2.21)$$

with $c_0 = 2127.5 \text{ J kg}^{-1} \text{ K}^{-1}$, $c_\Delta = 7.253 \text{ J kg}^{-1} \text{ K}^{-1}$ and $T_0 = 273.16 \text{ K}$. We assume the ice to be incompressible, so the density remains constant. Therefore:

$$\frac{dE}{dt} = \rho_i \frac{d(c_i T_i)}{dt}. \quad (2.22)$$

Using Equation 2.21 and the fact that $dT_i/dt = \partial T_i/\partial t + \vec{v} \cdot \nabla T_i$, with \vec{v} the ice velocity, we get:

$$\frac{dE}{dt} = \rho_i \cdot (2c_i - c_0 + c_\Delta T_0) \cdot \left(\frac{\partial T_i}{\partial t} + \vec{v} \cdot \nabla T_i \right). \quad (2.23)$$

Furthermore, we use Fourier's law of heat conduction, which states that the heat conduction is proportional to and in opposite direction of the temperature gradient:

$$\vec{\phi}_q = -\kappa_i \nabla T_i, \quad (2.24)$$

with κ_i the thermal conductivity of ice (Cuffey and Paterson, 2010):

$$\kappa_i = \kappa_0 e^{-\kappa_e T}. \quad (2.25)$$

Here, $\kappa_0 = 9.828 \text{ J m}^{-1} \text{ K}^{-1} \text{ s}^{-1}$ and $\kappa_e = 0.0057 \text{ K}^{-1}$.

Combining Equations 2.19, 2.23 and 2.24 yields:

$$\rho_i \cdot (2c_i - c_0 + c_\Delta T_0) \cdot \left(\frac{\partial T_i}{\partial t} + \vec{v} \cdot \nabla T_i \right) = \kappa_i \nabla^2 T_i + \Phi, \quad (2.26)$$

where the term with $(\nabla T_i) \cdot (\nabla \kappa_i)$ has been omitted because it is negligibly small. The internal heating (or shear heating) rate, Φ , is given by:

$$\Phi = \sum_{ij} \dot{\epsilon}_{ij} \tau'_{ij}, \quad (2.27)$$

with i and j representing the three different directions x , y and z , $\dot{\epsilon}_{ij}$ the strain rate tensor:

$$\dot{\epsilon}_{ij} = \frac{1}{2} \left(\frac{\partial v_i}{\partial j} + \frac{\partial v_j}{\partial i} \right), \quad (2.28)$$

and τ'_{ij} the deviatoric stress tensor:

$$\tau'_{xz} = -\rho_i g (s - z) \frac{\partial s}{\partial x}, \quad (2.29)$$

$$\tau'_{yz} = -\rho_i g (s - z) \frac{\partial s}{\partial y}, \quad (2.30)$$

from some point at altitude z to the surface altitude s . This leads to:

$$\Phi = -\rho_i g (s - z) \left(\frac{\partial u}{\partial z} \frac{\partial s}{\partial x} + \frac{\partial v}{\partial z} \frac{\partial s}{\partial y} \right). \quad (2.31)$$

Here, u and v are the ice velocity components in the x- and y-direction respectively. On the right hand side of Equation 2.26, the term $\kappa_i \nabla^2 T_i$ represents the diffusion. The horizontal diffusion is neglected in ANICE because the temperature difference per unit distance is much smaller in the horizontal direction than in the vertical direction, and the horizontal heat transport by diffusion is much smaller than by advection.

2.7 Coupling of the model components

All the different components mentioned in this chapter are linked through different variables. As input the model needs the SMB, the geothermal heat flux, the air and ocean temperature and the initial ice temperature, bed topography and ice thickness (see Figure 2.3).

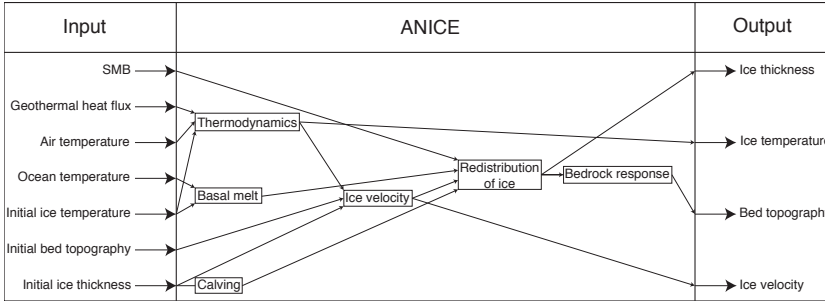


Figure 2.3: Scheme of the input and output of ANICE and how they are linked through the different components of the model.

From the ocean and ice temperature the basal melt can be calculated, whereas the calving parameterisation only needs the ice thickness. The thermodynamics of the ice sheet are mostly determined by the air and initial ice temperature and the geothermal heat flux. Eventually, the ice is redistributed through the application of basal melt, calving, SMB and ice movement. The velocity of the ice is calculated by using the SIA and the SSA, and depends on the thermodynamics, the bedrock

topography and the ice thickness. Finally, the bedrock responds to the redistribution of the ice after which a new time step can be started with the new state of the ice sheet serving as initial fields. The output of the model consists of the ice thickness, ice velocity, bed topography and ice temperature, from which the position of the grounding line can be deduced for instance.

CHAPTER 3

A climate model intercomparison for the Antarctic region: present and past

Eighteen General Circulation Models (GCMs) are compared to reference data for the present, the Mid-Holocene (MH) and the Last Glacial Maximum (LGM) for the Antarctic region. The climatology produced by a regional climate model is taken as a reference climate for the present. GCM results for the past are compared to ice-core data. The goal of this study is to find the best GCM that can be used to drive an ice-sheet model that simulates the evolution of the Antarctic Ice Sheet. Because temperature and precipitation are the most important climate variables when modelling the evolution of an ice sheet, these two variables are considered in this chapter. This is done by ranking the models according to how well their output corresponds with the references. In general, present-day temperature is simulated well, but precipitation is overestimated compared to the reference data. Another finding is that model biases play an important role in simulating the past, as they are often larger than the change in temperature or precipitation between the past and the present. Considering the results for the present-day as well as for the MH and the LGM, the best performing models are HadCM3 and MIROC 3.2.2.

This chapter is based on: A climate model inter comparison for the Antarctic region: present and past, by M.N.A. Maris, B. de Boer and J. Oerlemans, *Climate of the Past*, 9, 803-814, 2012, doi:10.5194/cp-8-803-2012.

3.1 Introduction

Variations in ice volume of the Antarctic Ice Sheet (AIS) have a large impact on sea level and ocean circulation. Since the Last Glacial Maximum (LGM), at approximately 21 kyr ago, the AIS has undergone many changes (e.g., Huybrechts, 2002; Bentley, 1999). This is especially true for the West Antarctic Ice Sheet, which is potentially unstable (see for example, Hughes, 1975; Thomas, 1979; Bamber et al, 2009). To study variations in the AIS with a dynamical ice-sheet model, realistic (near-surface) air temperature and precipitation are needed as input. These variables may be given by a General Circulation Model (GCM) or a Regional Climate Model (RCM), which in its turn may be driven by a GCM at its lateral boundaries. Therefore it is important to know which GCMs perform well in the Antarctic region.

It is generally accepted that a model performs well when it is close to the ensemble mean, as was done by Zweck and Huybrechts (2005). However, the best GCM for a specific study or use might not be the one closest to the ensemble mean. For instance, when using a GCM to drive an RCM, it is important that the GCM produces realistic output close to the boundaries of the RCM, whereas certain regional biases in the GCM may play a bigger role when studying a part of the AIS. In the literature, different criteria have been described for a GCM to perform 'well', such as high resolution (Ren et al, 2011) and low bias (Murphy et al, 2002). However, these studies focus on either only one model or one criterion, instead of intercomparing a larger set of GCMs.

Comparisons of larger sets of GCMs have been done through the Paleoclimate Modelling Intercomparison Project Phase II (PMIP2, Braconnot et al (2007)), which has a large database with output from GCMs for the present, the Mid-Holocene (MH) and the LGM. Intercomparison studies of the models in this database have been done by, amongst others, Braconnot et al (2007), Yanase and Abe-Ouchi (2007), Brewer et al (2007) and Masson-Delmotte et al (2006). Only the study of Masson-Delmotte et al (2006) focuses on the polar regions (and therefore Antarctica). They conclude that the PMIP2 models' simulations agree reasonably well with ice-core signals for both the MH and the LGM, although there are uncertainties in the models' ice-sheet topography, which is based on ICE-5G (Peltier, 2004). However, their study focuses on the ensemble mean of all the models under consideration and less on the differences between models.

In order to decide which GCMs perform best in the Antarctic region, we compare the individual output of the models to ice-core reconstructions for the MH and LGM. Furthermore, as ice-core data have large uncertainty and do not cover the entire Antarctic region, we compare present-day GCM data to a reference state from RACMO2/ANT (Lenaerts et al, 2012a). RACMO2/ANT is a regional climate model, which has been developed especially for polar regions and has been thoroughly validated (e.g., Van de Berg et al, 2005; Lenaerts et al, 2012b).

Model name in PMIP2 database	Abbreviation	Resolution lon x lat	Averaging time (yr)	6 kyr ago	21 kyr ago
CCSM	CCSM	2.81° x 2.81°	100	X	X
CNRM-CM33	CNRM	2.81° x 2.81°	300		X
CSIRO-Mk3L-1.0	CSIRO-1.0	5.63° x 3.22°	100	X	
CSIRO-Mk3L-1.1	CSIRO-1.1	5.63° x 3.22°	50	X	
ECBILTCLIO	Ecbiltclio	5.63° x 5.63°	50		X
ECBILTCLIOVE-CODE	Ecbiltcliove	5.63° x 5.63°	100	X	
ECHAM5-MPIOM1	ECHAM5	3.75° x 3.75°	50	X	
ECHAM53-MPIOM127-LPJ	ECHAM53	3.75° x 3.75°	100	X	X
FGOALS-1.0g	FGOALS	2.81° x 3°	100	X	X
FOAM	FOAM	7.5° x 4.5°	100	X	
GISSmodelE	GISS	5° x 3.92°	50	X	
HadCM3M2	HadCM3	3.75° x 2.5°	100		X
IPSL-CM4-V1-MR	IPSL	3.75° x 2.5°	100	X	X
MIROC 3.2	MIROC 3.2	2.81° x 2.81°	50	X	X
MIROC 3.2.2	MIROC 3.2.2	2.81° x 2.81°	100		X
MRI-CGCM2.3.4fa	MRI-fa	2.81° x 2.81°	100	X	
MRI-CGCM2.3.4nfa	MRI-nfa	2.81° x 2.81°	100	X	
UBRIS-HadCM3M2	UBRIS	3.75° x 2.5°	100	X	

Table 3.1: *The models evaluated in this study, with the abbreviations used in this chapter, their horizontal resolution and the length of the period used to determine the climatological mean. Crosses indicate whether the model provided output for 6 kyr ago and/or 21 kyr ago.*

3.2 Method

Eighteen models from the PMIP2 database, see Table 3.1, are compared with reference data from RACMO2/ANT for the present-day climate and with ice-core climate reconstructions for the past. The GCM data used for this study originate from coupled ocean-atmosphere models. Some of the models are closely related to others: UBRIS-HadCM3 and HadCM3 are much alike; CSIRO-1.1 is the same as CSIRO-1.0, but with a doubled oceanic resolution; MRI-fa uses flux adjustments for heat and water fluxes and wind stress, whereas MRI-nfa does not; and MIROC 3.2.2 is the same as MIROC 3.2, but an error in the land surface scheme of MIROC 3.2 has been corrected in MIROC 3.2.2, affecting the wind stress calculation over ice sheets and resulting in somewhat lower temperatures. Nonetheless, MIROC 3.2 has been included in this study because there are additional (Mid-Holocene) simulations available for this model.

The present-day reference state originates from RACMO2/ANT, at a horizontal resolution of 27 km. RACMO2/ANT is forced at its lateral boundaries by ERA-Interim reanalysis data for 20 years (1989-2009). RACMO2/ANT has been chosen because it provides data at a high resolution. Furthermore, temperature and precipitation have a smaller bias than reanalysis products such as ERA-40 or ERA-Interim

(Van de Berg et al, 2006, 2007; Van de Berg, 2008; Ettema et al, 2010; Lenaerts et al, 2012b). The uncertainty in RACMO2/ANT precipitation is about 10% (Lenaerts et al, 2012b). The uncertainty in 2m air temperature is more difficult to determine, a plot of the difference between yearly average RACMO2/ANT skin temperature and observed temperatures at 10 m depth is shown in Figure 3.1. The difference between modelled and observed temperatures is small, except for parts of the Western Antarctic Ice Sheet.

The RACMO2/ANT-domain runs from 90° South to approximately 47° South. We compared 2m air temperature and annual mean precipitation from the GCMs with RACMO2/ANT-data. To this purpose all GCM data are interpolated on the RACMO2/ANT grid. No lapse rate correction has been applied to the GCM data to compensate for the mismatches in surface height between the GCMs and RACMO2/ANT. This is because when the same analysis as the one described in this chapter was performed on the GCM data with a lapse rate correction of -11.6 K/km (Masson-Delmotte et al, 2011), this did not change the results much and introduced uncertainties that were not in the GCM output initially.

The data are compared regarding bias, root mean square deviation (rmsd), and correlation coefficient (ρ):

$$\text{bias} = \frac{\sum_{i=1}^N x_{G_i} - x_{R_i}}{N}, \quad (3.1)$$

$$\text{rmsd} = \sqrt{\frac{\sum_{i=1}^N (x_{G_i} - x_{R_i})^2}{N}}, \text{ and} \quad (3.2)$$

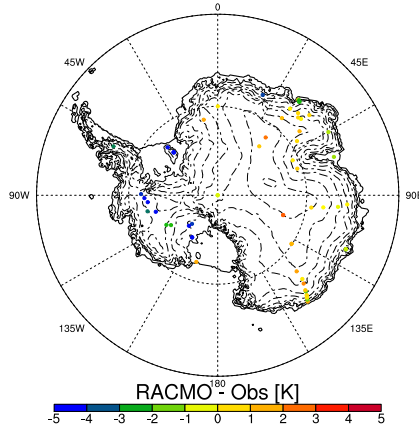


Figure 3.1: A map of the Antarctic continent showing the yearly average temperature difference between RACMO2/ANT and observations, at locations where observations have been made.

$$\rho = \frac{\sum_{i=1}^N (x_{G_i} - \bar{x}_G) \cdot (x_{R_i} - \bar{x}_R)}{\sqrt{\sum_{i=1}^N (x_{G_i} - \bar{x}_G)^2 \cdot \sum_{i=1}^N (x_{R_i} - \bar{x}_R)^2}}, \quad (3.3)$$

in which the subscripts G and R stand for GCM and RACMO2/ANT respectively and \bar{x} indicates the average of the variable x over all grid points i .

The correlation coefficient indicates how well temperature and precipitation patterns are simulated by a model, whereas the bias (mean deviation of the model from the reference) and the rmsd (a measure for the absolute deviation of the model from the reference) quantify how much the model output deviates from the reference state as a whole. A distinction is made between results over the ice sheet, including ice shelves (Figure 3.2) and results over the ocean (Figure 3.3). The bias, rmsd and correlation coefficient have been chosen because together they give a good overview of whether the GCMs can reproduce the correct patterns and realistic absolute values of temperature and precipitation.

In the second part of this study, GCM output for the MH (6 kyr ago) and the LGM (21 kyr ago) is compared to the present. Differences between the past and the present are evaluated, using reconstructions from ice cores (see Figure 1.1 for their locations). Temperature data are available from six ice cores for both the MH and the LGM:

- EPICA Dome C (EDC), a deuterium excess based temperature reconstruction by Jouzel et al (2007).
- EPICA Dronning Maud Land (EDML), a deuterium and $\delta^{18}\text{O}$ based temperature reconstruction. The ΔT for the MH was read from Figure 7b by Stenni et al (2010), the ΔT for the LGM is mentioned in their paper as well.
- Dome Fuji (Fuji), a deuterium and $\delta^{18}\text{O}$ based temperature reconstruction by Kawamura et al (2007).
- Law Dome (LD), a $\delta^{18}\text{O}$ reconstruction is given in Figure 5 in Van Ommen et al (2004). Past temperatures may be calculated from this graph by using a conversion of $0.44\text{‰} \text{ } ^\circ\text{C}^{-1}$. Details were communicated in Van Ommen (2011).
- Vostok, a deuterium temperature reconstruction by Petit et al (1999).

Precipitation records are scarce as they are more difficult to derive from ice cores. The precipitation reconstructions used in this study are:

- Law Dome, the accumulation rate is determined from a flow model together with age-ties in Van Ommen et al (2004), the reconstructions are given in Table 2 of their paper.
- Talos Dome, a $\delta^{18}\text{O}$ based precipitation reconstruction is given in Figure 7 in Buiron et al (2011) in cm ice equivalent per year. To get the precipitation change in mm water equivalent per year, the number is multiplied by 9.2.

- Vostok, a reconstruction based on ^{10}Be , given in Figure 7 in Steig et al (2000).

The model output is compared to ice-core data with respect to the temperature difference between the past and the present, the precipitation difference between the past and the present and the ratio of past to present precipitation, where both past and present-day data originate from the GCMs. The precipitation ratio is given because some models give a correct change in precipitation, but overestimate the actual amount both in the past and for the present-day. In this case the modelled ratio will be larger than the ratio deduced from the corresponding ice core. The comparison is carried out by interpolating the data from the four grid points of the GCM closest to the location of the ice core.

The goal of this study is to find the best models regarding simulations of temperature and precipitation. To do this a simple ranking system is introduced: The best model for a certain variable, e.g. temperature bias of the present-day output, gets 10 points, the next gets 9 points, etc. For every period (i.e. present-day, MH and LGM) these points are added up per model, resulting in a ranking of the models for each of the periods. When multiple models have the same amount of points, the spread is taken into account. That is to say, a model is judged to be better when an intermediate number of points is scored for all the variables than the maximum number of points for only half of the variables.

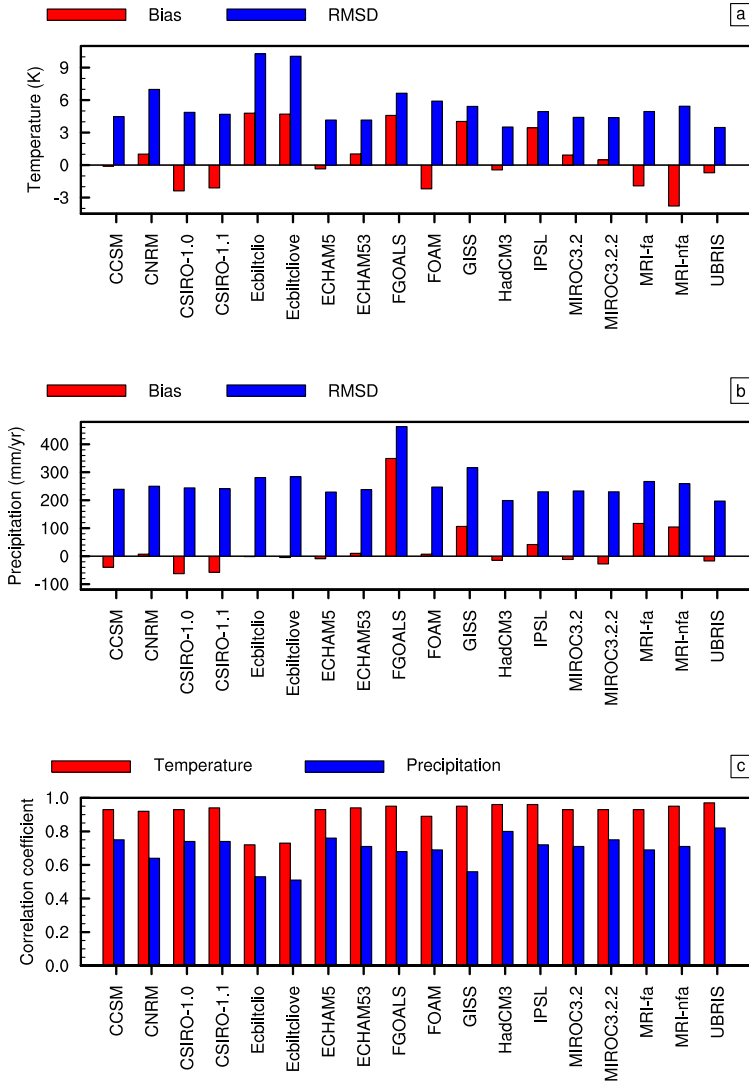


Figure 3.2: The bias (red) and rmsd (blue) for a) temperature and b) precipitation. c) Spatial correlation coefficients (c) for temperature (red) and precipitation (blue) for all PMIP2 models, as compared to the RACMO2/ANT reference state. These results apply to the ice sheet, for the present-day climate.

3. GCM intercomparison

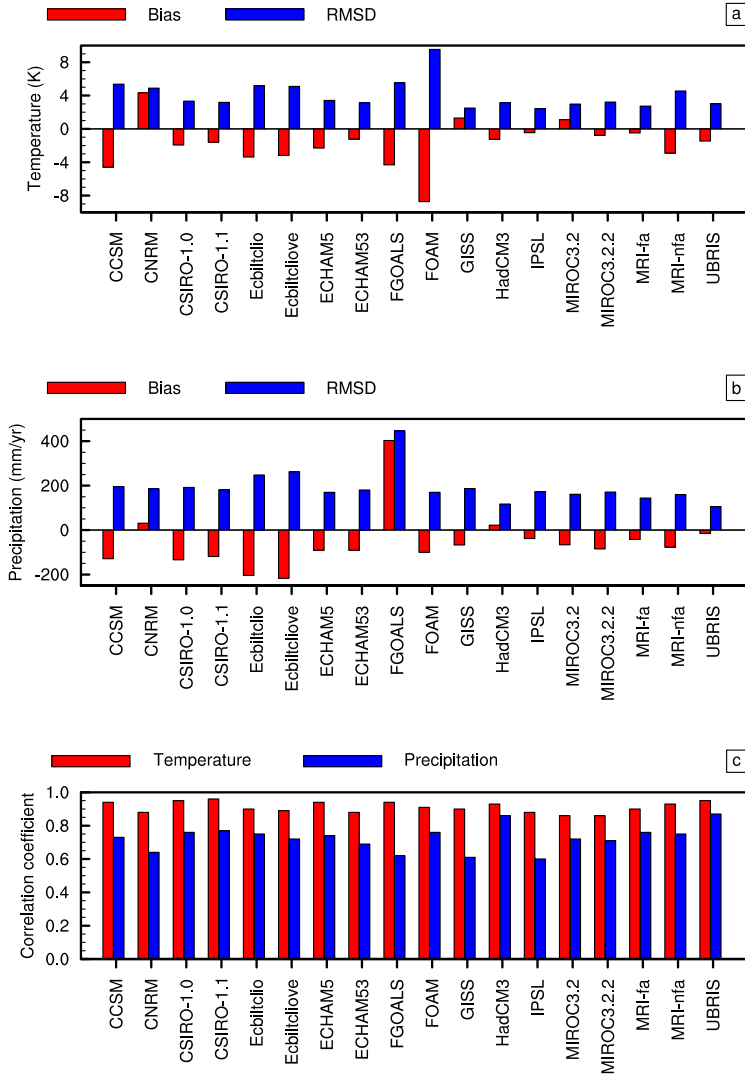


Figure 3.3: The bias (red) and rmsd (blue) for a) temperature and b) precipitation. c) Spatial correlation coefficients (c) for temperature (red) and precipitation (blue) for all PMIP2 models, as compared to the RACMO2/ANT reference state. These results apply to the ocean, for the present-day climate.

3.3 Present-day results

Figure 3.2a shows the bias (in red) and the rmsd (in blue) for the present-day temperature comparison between the PMIP2-models and RACMO2/ANT over the ice sheet

and ice shelves. The biases range from -3.8 K (MRI-nfa) to +4.8 K (Ecbiltclio) and the rmsd values go up to 10.3 K (Ecbiltclio) for the temperature. Temperature correlation coefficients (shown in Figure 3.2c in red for the temperature) are close to 1, ranging from 0.89 to 0.97, for all models except for Ecbiltclio and Ecbiltcliove-code.

Precipitation bias and rmsd are presented in Figure 3.2b. The highest bias is +349 mm/yr for FGOALS, which also shows the highest rmsd value of 463 mm/yr. Precipitation correlation coefficients show a larger spread than for temperature, from 0.51 to 0.82. The largest bias and rmsd are found for the precipitation output of FGOALS and the temperature output of FOAM, which might be due to the low resolution of the model. As mentioned before, the model MIROC 3.2.2 should give lower temperatures (and therefore a smaller temperature bias) than MIROC 3.2 due to a corrected error in MIROC 3.2.2, which is indeed the case.

In Figure 3.3 the same variables are presented as in Figure 3.2, but for a domain that only incorporates the ocean grid points of RACMO2/ANT. Again, the temperature correlation coefficients are mostly close to 1, ranging from 0.86 to 0.96. Precipitation correlation coefficients are slightly larger here than over the ice sheet (from 0.60 to 0.87). Rmsd values are smaller, while bias values are generally somewhat larger, i.e. more negative, over the ocean.

The four models that simulate the present-day climate best are UBRIS, HadCM3, ECHAM5 and IPSL for temperature and UBRIS, HadCM3, ECHAM5, and MIROC 3.2 for precipitation. This is based on the ranking method, applied on the combination of the results over the ice sheet and the ocean. The difference fields between these best models and RACMO2/ANT are shown in Figure 3.4 for temperature and Figure 3.5 for precipitation.

A notable feature in Figure 3.4 is that the modelled temperatures over the Ross ice shelf (see Figure 1.1) are too high, which is the case for almost all models. At the locations of these ice shelves, land is modelled by the GCMs, which is only partly covered with ice. In contrast, over the Amery Ice Shelf region the models simulate too low temperatures. This is something to take into account when deciding on which model to use. For example, when focussing on West-Antarctica, HadCM3 shows less (negative) bias there than the other models and might be a better choice because RACMO2/ANT shows a negative bias here as well when compared to observations. The modelled temperatures are closer to the reference data over the ocean, at the edges of the domain.

Precipitation is generally overestimated inland. It is underestimated close to the coasts and strongly underestimated at the western side of the Antarctic Peninsula by all models. This is probably due to the fact that the steep orography of the Peninsula is not well represented in the GCMs. Consequently, the orographically enhanced precipitation is underestimated (Rojas et al, 2009).

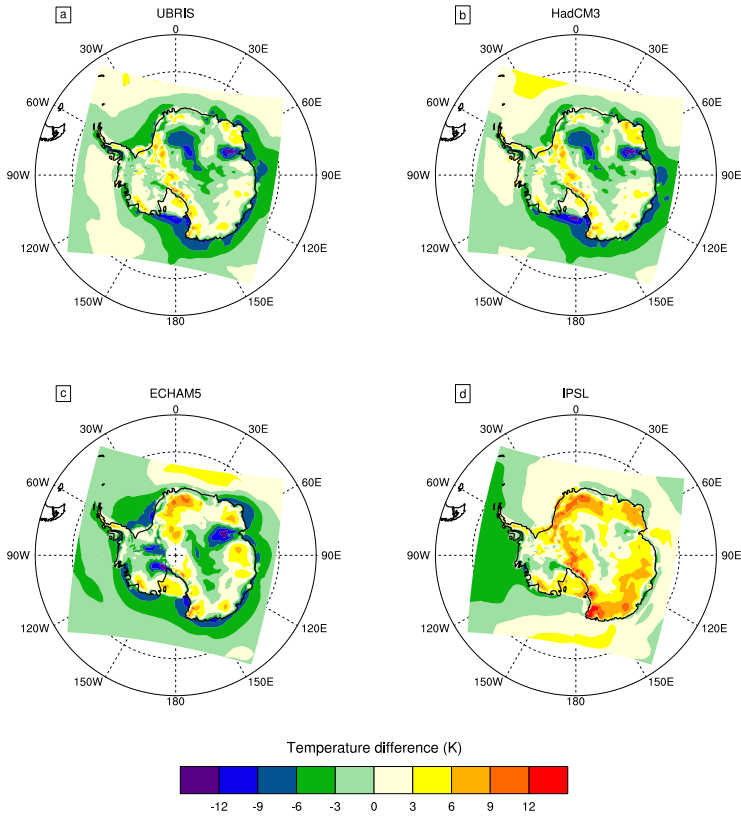


Figure 3.4: Present-day temperature difference fields of a) UBRIS, b) HadCM3, c) ECHAM5 and d) IPSL with RACMO2/ANT, interpolated on the RACMO2/ANT grid.

3.4 Mid-Holocene results

Mid-Holocene temperature output from the models is compared to reconstructions from five ice cores in Table 3.2. The uncertainty ranges of these reconstructions are probably larger than the small differences in temperature between the MH and the present. The models also simulate small temperature differences between the MH and the present. However, the models do not capture the change in sign of the temperature differences between different locations, i.e. EDC and Fuji were colder in the MH than in the present and the temperature difference was largest at Law Dome.

For temperature, the best models according to the ranking method are CSIRO-1.1 and IPSL. The spatial distribution of the temperature difference between the MH and the present (both MH and present temperature values are from GCM output) are shown in Figure 3.6. Temperature differences are mainly positive, but small,

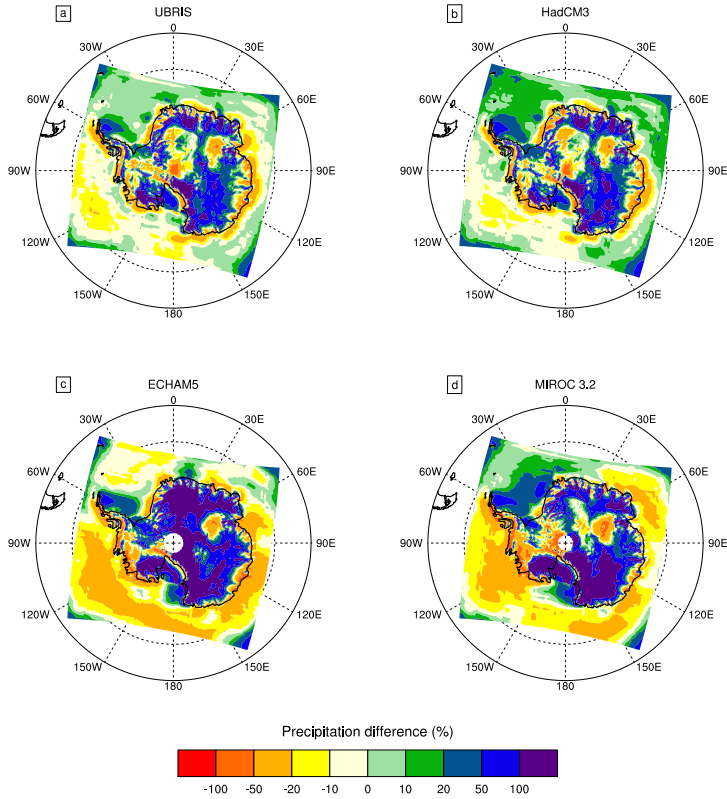


Figure 3.5: Relative present-day precipitation difference fields of a) UBRIS, b) HadCM3, c) ECHAM5 and d) MIROC 3.2 with RACMO2/ANT (as a percentage of RACMO2/ANT precipitation).

except over the western South Pacific Ocean in Figure 3.6b (IPSL). Although this difference between the models may not be of much importance when using GCM output in an ice-sheet model, it is important when only using the output to provide boundary conditions for an RCM. The negative temperature differences over the western ocean in IPSL cannot be affirmed nor negated by ice-core reconstructions. It may therefore be concluded that the comparison of model output with ice-core reconstructions gives an indication of which models are better than others, but it is not conclusive. This is even more true for precipitation, as is argued below.

In Table 3.3 precipitation data are shown for three ice-core locations. The Law Dome data are not very accurate as only the average accumulation between age ties (2545 and 6778 years ago) is known (Van Ommen et al, 2004). At the Talos Dome location, the difference in precipitation between 6 kyr ago and the present is captured by most GCMs, but the ratios are too high. This means that, at this location, the absolute amounts of precipitation are overestimated by the models in

	EDC	EDML	Fuji	LD	Vostok
Ice core	-0.4	0.5	-0.4	1.3	0.4
CCSM	0.1	0.0	0.1	0.0	0.3
CSIRO-1.0	0.4	0.3	0.4	0.3	0.4
CSIRO-1.1	0.2	0.9	0.0	0.4	0.4
Ecbiltcliove	0.3	0.3	0.1	0.4	0.1
ECHAM5	0.2	0.2	0.6	0.4	0.4
ECHAM53	0.4	0.0	0.4	0.3	0.5
FGOALS	0.1	0.3	0.5	0.2	0.2
FOAM	0.5	0.7	0.6	0.9	0.7
GISS	-0.3	-0.6	-0.2	-0.1	-0.1
IPSL	0.6	0.6	0.5	0.4	0.4
MIROC 3.2	0.2	0.1	0.3	0.4	0.4
MRI-fa	0.2	0.1	0.4	0.9	0.3
MRI-nfa	-0.4	-0.4	-0.5	-0.9	-0.2
UBRIS	0.7	0.8	0.8	0.1	0.7

Table 3.2: Reconstructed and modelled temperature differences (in Kelvin) between the MH and the present at five ice-core locations. Modelled temperature differences are calculated by interpolating the four closest model data points.

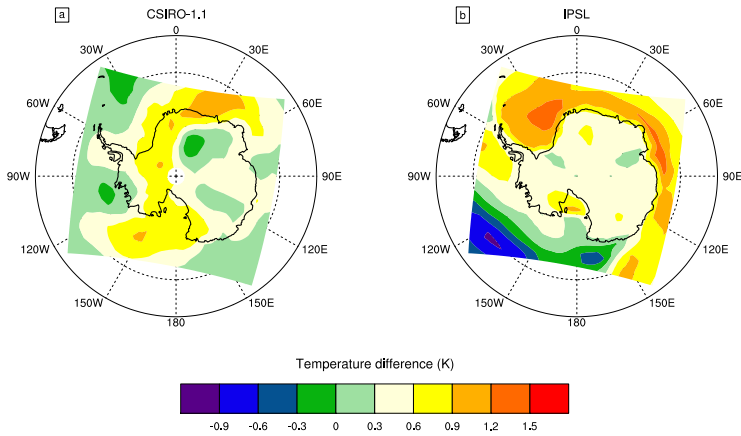


Figure 3.6: Temperature difference fields between 6 kyr ago and the present for a) CSIRO-1.1 and b) IPSL.

both present and past. This can be seen in Figure 3.5 as well. Precipitation at the Vostok location is simulated quite accurately by most of the GCMs.

CCSM and Ecbiltcliove precipitation differences between the MH and the present are shown in Figure 3.7, as these are the best models according to the ranking method. It is clearly visible that the patterns are not the same for these two models. The question remains which model is the better one. The differences between 6 kyr

3.4. Mid-Holocene results

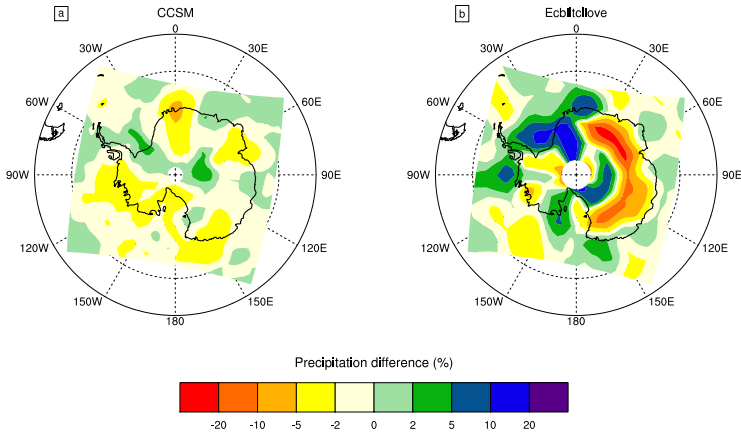


Figure 3.7: Relative precipitation difference fields (as a percentage of the present-day precipitation) between 6 kyr ago and the present for a) CCSM and b) Ecbiltcliove.

	Law Dome		Talos		Vostok	
	difference	ratio	difference	ratio	difference	ratio
Ice core	0	1.0	-10	0.9	0.5	1.0
CCSM	-3	1.0	-4	1.0	0.1	1.0
CSIRO-1.0	9	1.0	11	1.1	0.3	1.0
CSIRO-1.1	14	1.0	14	1.1	1.0	1.1
Ecbiltcliove	-10	1.0	-15	1.0	0.7	1.0
ECHAM5	34	1.1	-4	1.0	-0.2	1.0
ECHAM53	18	1.0	5	1.0	0.1	1.0
FGOALS	10	1.0	29	1.1	0.6	1.0
FOAM	22	1.1	1	1.0	0.6	1.0
GISS	-15	1.0	39	1.1	-0.9	1.0
IPSL	44	1.1	14	1.1	1.0	1.1
MIROC 3.2	52	1.1	8	1.0	-0.1	1.0
MRI-fa	17	1.0	-6	1.0	-0.6	1.0
MRI-nfa	-21	1.0	-8	1.0	4.1	1.0
UBRIS	25	1.1	6	1.0	-0.7	1.0

Table 3.3: Reconstructed and modelled precipitation differences (in mm/yr) between 6 kyr ago and the present, and ratios of the 6 kyr ago to the present precipitation at three ice-core locations.

ago and the present are small, and the biases are of the same order of magnitude. This makes it hard to distinguish between the GCMs in terms of performance for the MH.

To investigate the influence of biases in simulating the present climate on model performance when simulating the past, a signal-to-noise ratio has been calculated for both temperature and precipitation. The signal is the difference, in temperature

	EDC	EDML	Fuji	LD	Vostok
Ice core	-9.3	-7.4	-7.6	-14.8	-8.1
CCSM	-10.4	-7.5	-9.4	-8.9	-11.0
CNRM	-4.4	-6.1	-3.8	-1.6	-5.4
Ecbiltclio	-3.8	-4.7	-4.3	-6.7	-2.7
ECHAM53	-12.0	-7.2	-11.1	-6.7	-11.6
FGOALS	-12.0	-12.4	-12.2	-11.0	-12.9
HadCM3	-9.3	-6.9	-8.0	-4.0	-11.0
IPSL	-5.4	-3.9	-5.4	-2.5	-6.7
MIROC 3.2	-6.6	-5.0	-6.3	-4.2	-6.7
MIROC 3.2.2	-8.5	-6.7	-7.6	-5.4	-7.8

Table 3.4: Reconstructed and modelled temperature differences (in Kelvin) between the LGM and the present at five ice-core locations.

or precipitation, between 6 kyr ago and the present. The noise is the present-day bias of a model, as shown in Figures 3.2 and 3.3. For precipitation the average signal-to-noise ratio of all GCMs is 0.09, which is very low. This means that the signal is practically indistinguishable from the data. The mean signal-to-noise ratio for temperature is 0.21. Combining this with the presumably large uncertainties in the ice-core reconstructions, compared to the signal, judgements about which models achieve the best results for the MH cannot be accurately made.

3.5 LGM results

In Table 3.4 modelled temperature differences between the LGM and the present are compared to data from five ice cores. At Law Dome the temperature difference is the largest, which is not captured by any of the GCMs, except for Ecbiltclio. However, Ecbiltclio generally simulates too small temperature differences between the LGM and the present. This holds for CNRM as well, whereas FGOALS overestimates the temperature differences at four of the five locations. According to the ranking method, MIROC 3.2.2 and CCSM are the best models. Output from these models is shown in Figure 3.8.

MIROC 3.2.2 simulates smaller temperature differences than CCSM, which is also visible in Table 3.4. Both models show larger temperature differences over West Antarctica, which is the case for almost all models with LGM output. This is probably due to the change in topography, as the difference between the LGM and the present in ice thickness of the West Antarctic Ice Sheet is larger than the difference of the East Antarctic Ice Sheet. This agreement between the models regarding the temperature pattern over the ice sheet gives some confidence when using either one as input in an ice-sheet model. However, when using the data to drive an RCM, the boundaries become important, as has been noted before, and the differences between MIROC 3.2.2 and CCSM might play a bigger role.

	Law Dome		Talos		Vostok	
	difference	ratio	difference	ratio	difference	ratio
Ice core	-584	0.1	-39	0.4	-8	0.6
CCSM	-118	0.6	-119	0.5	-20	0.3
CNRM	-99	0.8	22	1.1	-9	0.7
Ecbiltclio	6	1.0	-186	0.6	-103	0.5
ECHAM53	-148	0.7	-104	0.6	-23	0.3
FGOALS	-919	0.4	-226	0.6	-43	0.4
HadCM3	-165	0.7	-36	0.7	-17	0.3
IPSL	18	1.0	-8	1.0	-9	0.5
MIROC 3.2	-106	0.8	-37	0.9	-14	0.5
MIROC 3.2.2	-137	0.7	-77	0.7	-13	0.5

Table 3.5: Reconstructed and modelled precipitation differences (in mm/yr) between the LGM and the present, and the ratios of the LGM to the present precipitation at three ice-core locations.

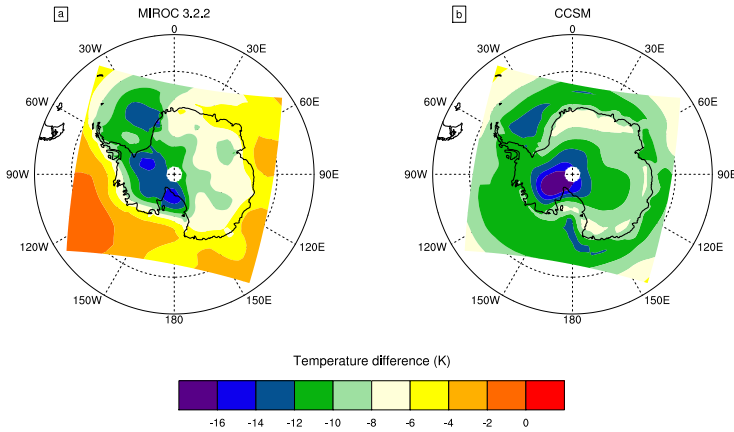


Figure 3.8: Temperature difference fields between the LGM and the present GCM-output for a) MIROC 3.2.2 and b) CCSM.

Modelled precipitation differences between the LGM and the present are compared to reconstructions for Law Dome, Talos Dome and Vostok data in Table 3.5. For Law Dome the LGM-precipitation was less than 10% of the present-day value. Law Dome is located near the coast, where it receives precipitation from cyclonic systems. These systems have probably changed since the LGM, causing a large change in precipitation in coastal regions (Van Ommen et al, 2004). None of the models has captured this change, suggesting that the representation of cyclonic systems is deficient, something also noted by Rojas et al (2009).

Figure 3.9 shows the precipitation difference fields between the LGM and the present-day climate for HadCM3 and MIROC 3.2.2, which appear to be the best models regarding this variable. Overall, the LGM was drier than the present, while

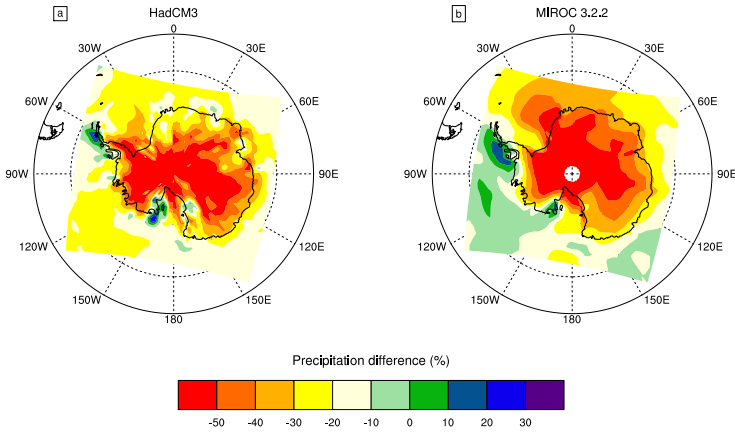


Figure 3.9: Relative precipitation difference fields (as a percentage of the present-day precipitation) between the LGM and the present for a) HadCM3 and b) MIROC 3.2.2.

the tip of the Antarctic Peninsula is modelled to have been wetter. This applies to most of the models and might be related to the underestimation of western Antarctic Peninsula precipitation in the present-day output.

Signal-to-noise ratios have been calculated for the LGM as well to study the influence of the biases of the models on the simulation of precipitation and temperature patterns at 21 kyr ago. The average signal-to-noise ratio for temperature is 3.8, which is significantly larger than 1. Overall this ratio means that the signal of temperature change from the LGM to the present is discernible when studying the model output. For precipitation the mean signal-to-noise ratio is 1.4, which is lower than the temperature signal-to-noise ratio. The precipitation signal-to-noise ratios are lower than the temperature signal-to-noise ratios for both the MH and the LGM. The reason for this is probably that precipitation is harder to model correctly than temperature, and therefore the biases are relatively larger. Although the signal-to-noise ratios for the LGM are higher than for the MH, it is still essential to be aware of the (present-day) bias of a model to correctly assess its output for the LGM.

3.6 Conclusions

In this chapter we compared present-day output from GCMs to a reference state from the regional climate model RACMO2/ANT for the Antarctic region. We found that air-temperature patterns are generally well simulated, as the correlation coefficients between the GCM output and the reference data are close to 1. Temperature is generally more correctly simulated over the ocean than over the ice sheet. The temperature over the ice shelves is too high in most of the models, which is probably due to the fact that there is land at the locations of the ice shelves in the GCMs,

which is only partly covered with ice.

Precipitation patterns are also well simulated in general, but the amount of precipitation is often underestimated over the ocean. In addition, a strong negative bias is observed over the western coast of the Antarctic Peninsula. The GCMs probably do not resolve the circulation pattern and the orography well enough to simulate the additional precipitation in this region (Rojas et al, 2009). Considering temperature and precipitation results for the present-day, the top five models are HadCM3, UBRIS, which is a HadCM3-based model, ECHAM5, MIROC 3.2, and IPSL.

The differences in temperature and precipitation between the Mid-Holocene and the present are small in ice-core reconstructions and in the output from the GCMs. Generally, both temperature and precipitation are higher during the MH than in the present climate. The differences between the MH and the present are small, and the biases of the GCMs are of the same order of magnitude or even larger. Therefore, it is hard to judge individual model performances. For the MH, the signal-to-noise ratios are 0.21 for temperature and 0.09 for precipitation. These low signal-to-noise ratios indicate that to find a model that performs well when modelling the past, it is important to take its present-day performance into account. Furthermore, the uncertainties in ice-core data are presumably as large as the signal as well, making it even harder to judge the performance of the models. Based on the comparison between the output of the GCMs and the ice-core reconstructions for the MH, the five best models are Ecbiltcliove, CCSM, MRI-fa, MRI-nfa and CSIRO-1.0. However, in the final judgement which GCMs perform best overall, the MH will not be taken into consideration as the biases in the models are too large to make the intercomparison trustworthy.

During the LGM, temperatures were lower and there was less precipitation than in the present-day climate, according to both ice-core reconstructions and GCM output. Also, the temperature difference between the LGM and the present is modelled to be larger over the West Antarctic Ice Sheet than over the East Antarctic Ice Sheet by most GCMs. The precipitation differences between the LGM and the present over the Antarctic Peninsula are generally modelled to be smaller than elsewhere, or even positive (wetter at the LGM than in the present). The differences between the past and the present are larger for the LGM than for the MH, and therefore the signal-to-noise ratios are higher: 3.8 for temperature and 1.4 for precipitation. This means that more confidence can be had in the ranking of the models, which points out MIROC 3.2.2, CCSM, HadCM3, ECHAM53 and MIROC 3.2 as the five best GCMs for the LGM.

The low signal-to-noise ratios indicate large uncertainties in the output of the models, but there are other sources of uncertainties in the comparison between model results and ice-core reconstructions. The first source, important to the judgement of present-day performance of the GCMs, is the uncertainty in RACMO2/ANT-data. This is negligible in this particular study according to Van de Berg (2008); Lenaerts et al (2012a). The second source is the uncertainty in the ice-core recon-

structions; part of this is due to the uncertainty in temperature and precipitation reconstruction and part is due to the uncertainty in the determination of the age of the ice in the ice core. The third source is the elevation. As Masson-Delmotte et al (2006) state in their paper, there probably is a discrepancy between the elevation at which the surface was in the past and the elevation that is used in the models. However, the past elevation of the ice sheet is not known with great accuracy either, nor is the lapse rate, so we decided not to correct for this discrepancy, which is probably within the uncertainty margin of the ice-core reconstructions.

To conclude, some models simulate temperature and precipitation significantly better than others, according to our ranking methods. Not all models provided data for the MH or the LGM, but the results for the MH are judged to be less significant due to large relative uncertainty in model output. Finally, considering both present-day and past simulations, the best performing models according to our comparison, in simulating temperature and precipitation in the Antarctic region, are HadCM3 and MIROC 3.2.2.

Acknowledgements

We acknowledge the international modelling groups for providing their data for analysis and the Laboratoire des Sciences du Climat et de l'Environnement (LSCE) for collecting and archiving the model data. The PMIP2 Data Archive is supported by CEA, CNRS and the Programme National d'Etude de la Dynamique du Climat (PNEDC). The analyses were performed using version 03-01-2011 of the database. More information is available on <http://pmip2.lsce.ipsl.fr/>. We also greatly appreciate the suggestions and detailed comments by S.J. Phipps and two anonymous reviewers, which led us to significant improvements of the manuscript. Additionally, we would like to thank J. Lenaerts for providing us with data from RACMO2/ANT.

Model sensitivity regarding the evolution of the Antarctic Ice Sheet since 120 000 years ago

We present the effects of changing two sliding parameters, a deformational velocity parameter and two bedrock deflection parameters on the evolution of the Antarctic Ice Sheet over the period from the last interglacial until the present. These sensitivity experiments have been conducted by running the ice-dynamical model ANICE forward in time. The climatological forcing over time is established by interpolating between two climate states from a regional climate model over time. The interpolation is done in such a way that both temperature and surface mass balance follow the Epica Dome C ice-core proxy record for temperature. We have determined an optimal set of parameter values, for which a realistic grounding-line retreat history and present-day ice sheet can be simulated, the simulation with this set of parameter values is defined as the reference simulation. An increase of sliding with respect to this reference simulation leads to a decrease of the Antarctic ice volume due to enhanced ice velocities on mainly the West Antarctic Ice Sheet. The effect of changing the deformational velocity parameter mainly yields a change in East-Antarctic ice volume. Furthermore, we have found a minimum in the Antarctic ice volume during the mid-Holocene, in accordance with observations. This is a robust feature in our model results, where the strength and the timing of this minimum are both dependent on the investigated parameters. More sliding and a slower responding bedrock lead to a stronger minimum which emerges at an earlier time. From the model results we conclude that the Antarctic Ice Sheet has contributed 10.7 ± 1.3 m of eustatic sea level to the global ocean from the Last Glacial Maximum (about 16 kyr ago for the Antarctic Ice Sheet) until the present.

This chapter is based on: Modelling the evolution of the Antarctic Ice Sheet since the Last Glacial Maximum, by M.N.A. Maris, B. de Boer, S.R.M. Ligtenberg, M. Crucifix, W.J. van de Berg and J. Oerlemans, *The Cryosphere*, 8, 1347-1360, 2014, doi: 10.5194/tc-8-1347-2014.

4.1 Introduction

The variability of the Antarctic Ice Sheet (AIS) has a large impact on sea level and ocean circulation. Its state depends strongly on geometric and climatic parameters. Many model studies have examined how the state and evolution of the AIS depend on those parameters (e.g. Ritz et al, 2001; Golledge et al, 2012; Whitehouse et al, 2012). In most evolutionary studies of the AIS over glacial timescales the climatological forcing is produced by shifting temperatures linearly following proxy records from an ice core such as Vostok, or Epica Dome C (e.g. Ritz et al, 2001; Huybrechts, 2002; Philippon et al, 2006), often corrected by applying a lapse rate to account for differences in the surface elevation. In these cases a constant lapse rate is assumed for the entire ice sheet and no spatial correction is made to account for the differences between, for example, grounded ice and ice shelves. Some other studies couple an ice-sheet model to a climate model, see for instance Aschwanden et al (2013), which is a computationally expensive exercise. In this study we use the regional atmospheric climate model RACMO2/ANT (Van Meijgaard et al, 2008) to produce a detailed climate forcing for the Last Glacial Maximum (LGM, 21 kyr ago), as well as for the present-day (PD). We assume the end of the last interglacial (120 kyr ago) to have the same climate as the PD. An interpolation method is used to create a climatological forcing that is continuous in time, making use of the Epica Dome C ice core record (Jouzel et al, 2007). This method leads to a realistic simulation of the climate while still being computationally feasible. The interpolation method is described in detail in Section 4.2.2.

Despite numerous studies on the subject, little is known about the sediment beneath the AIS and its effects on the magnitude and the variations in sliding. Consequently, the effect of the sediment on sliding is heavily parameterised in ice-dynamical models (e.g. Bueler and Brown, 2009; Pollard and DeConto, 2012b). Furthermore, ice-dynamical models generally make use of Glen's isotropic flow law (Glen, 1958), while ice is a highly anisotropic material. Therefore, so-called enhancement factors are introduced (see for instance Huybrechts (1992); Ma et al (2010); De Boer (2012); Pollard and DeConto (2012a)). These factors are different for grounded ice (which can be described by the Shallow Ice Approximation, the SIA) and sliding or floating ice (both described by the Shallow Shelf Approximation, the SSA). Additionally, the lithosphere is thinner under the West Antarctic Ice Sheet (WAIS) than under the East Antarctic Ice Sheet (EAIS) (Huerta and Harry, 2007). However, little is known about the lithospheric structure under Antarctica and how it influences the ice sheet (Morelli and Danesi, 2004). A thinner lithosphere is associated with smaller response times of the bed elevation to the ice load and to less rigidity, i.e. the amplitude of the deflection is larger for a given ice load (Le Meur and Huybrechts, 1996).

In this study we use the dynamical ice-sheet model ANICE (De Boer et al, 2013) to investigate how the AIS reacts to different lithospheric and sliding parameters

by doing sensitivity experiments on the period 120 kyr ago to present. The last interglacial period ended around 120 kyr ago, when temperature and sea level were close to PD values. The goal of this study is to learn how sensitive the AIS is to changes in different model parameters. Additionally, we want to find an optimal set of parameter values for which a realistic grounding-line retreat history and PD ice sheet are simulated. With these parameter values a more focussed study on the behaviour of the AIS during the last deglaciation can be facilitated.

4.2 Method

Starting with an initial state of the AIS 120 kyr ago, see Section 4.2.1, the ice-dynamical model ANICE has been run forward to the present. The applied climatological forcing combines the output of a regional atmospheric climate model with the Epica Dome C ice core record and will be discussed in Section 4.2.2. The surface mass balance is part of this climatological forcing, whereas the basal mass balance is deduced from the basal heat flux where the ice is grounded and from the ocean heat flux (see Section 4.2.3) where ice is in contact with water. Calving is parameterised by removing all floating ice below a threshold thickness of 250 m, at the end of every period of 300 yr. Other values for these two calving parameters have been tested as well, where the threshold thickness has been varied between 100 and 300 m and the period between 100 and 500 yr. These parameterisations did not change the grounding line or the grounded ice volume significantly, and therefore we decided to use the original parameterisation with a threshold ice thickness of 250 m and a calving period of 300 yr.

Ice velocities are calculated in ANICE by using both the SIA and the SSA (Bueler and Brown, 2009). The SIA is used as a basis for the velocities on the grounded part of the ice sheet and the SSA is used for ice-shelf and sliding velocities. The SSA velocity, which is assumed to be the basal velocity, and the SIA velocity are superposed as in PISM-PIK (Winkelmann et al, 2011). Both approximations include an enhancement factor because, generally, the SIA underestimates the ice velocity and the SSA overestimates it (Ma et al, 2010). We varied both enhancement factors in the sensitivity experiments.

Whether the ice is sliding or not and how fast it is sliding also depends on the sediments underneath the ice. Almost nothing is known about the material of which these sediments consist, but the assumption is that the subglacial sediments (till) are weaker when the bed is beneath sea level. Below sea level the bed is assumed to have a marine history, leading to a smaller grain size and clay-like till with little pore space. Therefore, water stays mostly on top of the till, enhancing the sliding potential of the ice (Clarke, 2005). The weakness of the till has been varied in the sensitivity experiments as well.

In addition to the enhancement factors and the till, there is another factor influencing the evolution of the AIS: the thickness of the lithosphere. In ANICE an ELRA

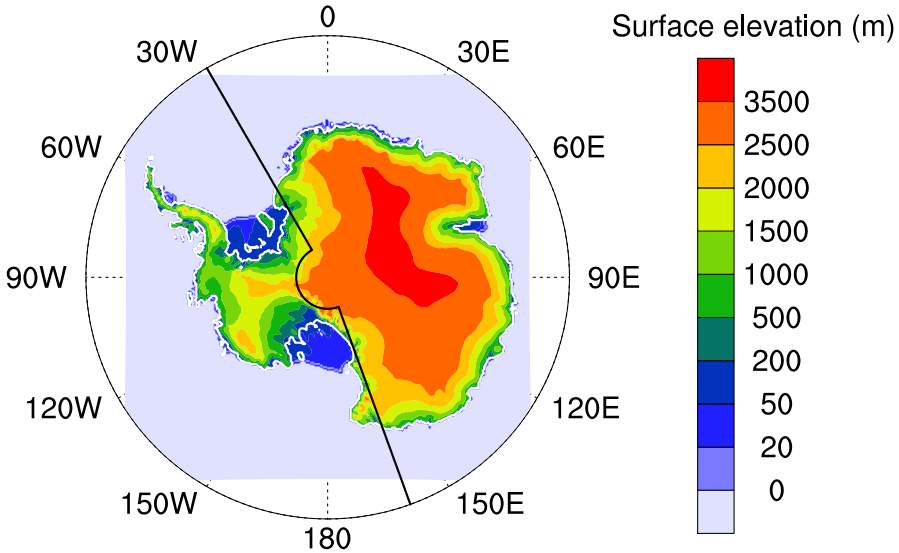


Figure 4.1: The PD surface elevation, used as an initial configuration 120 kyr ago. The white line indicates the grounding line and the black line separates the WAIS from the EAIS. The light blue box shows the ANICE model domain.

(Elastic Lithosphere, Relaxed Asthenosphere) model is included to describe the response of the bed elevation to the ice loading history (Le Meur and Huybrechts, 1996). The bed underneath the ice sheet is described as a thin, elastic lithosphere, controlling the geometric shape of a deformation, the elasticity is determined by the flexural rigidity in the model. The lithosphere floats on a viscous asthenosphere, which governs the time-dependent characteristics of a deformation. In the sensitivity experiments the response time and the flexural rigidity of the bedrock have been varied. The theory behind the sensitivity experiments will be discussed in Section 4.2.4.

4.2.1 Initial state

As an initial state for the last interglacial we use the PD configuration of the ice sheet as described in ALBMAP (Le Brocq et al, 2010), see Figure 4.1. We interpolated the bed topography, ice thickness and surface elevation from this data set onto the ANICE grid, a regularly spaced polar stereographic grid of 281×281 at a 20 km resolution. In the figure a black line is drawn where we define the separation between the EAIS and the WAIS. This line is drawn at: $30^\circ\text{W} \rightarrow 86^\circ\text{S} \rightarrow 160^\circ\text{E}$. ANICE is run forward in time with the PD surface temperatures and a fixed geometry (the ice thickness is kept fixed), such that the 3-D temperature field within the ice reaches a thermodynamical equilibrium. The output of this simulation has been used as the initial state.

4.2.2 Climatological forcing

We use the PD climate as an initial forcing at 120 kyr ago and a simulation of the LGM climate at the LGM. The climatological forcing of ANICE consists of the 2m-air temperature and the surface mass balance (SMB). The two climate states (PD and LGM) are a product of the regional atmospheric climate model RACMO2/ANT. This model includes a sophisticated snow model (Ettema et al, 2009) and albedo scheme (Kuipers Munneke et al, 2011) in order to realistically simulate snow-air interactions and liquid water processes (melt, percolation, retention, refreezing and runoff). In combination with a better horizontal grid resolution (55 km), RACMO2/ANT is therefore able to simulate a more realistic Antarctic climate than a general circulation model (GCM) (Ligtenberg et al, 2013). When forced with re-analysis data for the recent past, RACMO2/ANT has yielded realistic results over Antarctica, compared to in-situ observations (Van de Berg et al, 2006; Lenaerts et al, 2012b).

For the simulation of the Antarctic LGM climate, RACMO2/ANT is forced with a GCM simulation from HadCM3. HadCM3 was chosen because it consistently performs among the better GCMs above the Antarctic region (see Chapter 3). The method of laterally forcing RACMO2/ANT with GCM data was previously successfully used in future scenario simulations for the AIS (Ligtenberg et al, 2013). RACMO2/ANT is forced at the lateral boundaries of the domain with fields of temperature, wind components, surface pressure and specific humidity from the GCM simulation. Every six hours, the model value is linearly interpolated with the external forcing. Sea-ice concentration and sea-surface temperature are also prescribed by HadCM3. The extent and surface height of the AIS are part of the RACMO2/ANT input as well, but these variables are not well known for the LGM. We used the ICE-5G reconstruction by Peltier (2004) to provide RACMO2/ANT with topographical data because this topography was also used to produce the HadCM3 data. For the PD, ALBMAP data provided the topography, see Figure 4.1. The output of RACMO2/ANT has been integrated over 25 years to yield a representative climate for the LGM and PD periods.

The output of RACMO2/ANT is shown in Figure 4.2a-d. It is clear from these figures that both the temperature and the SMB have increased from the LGM to the PD over the ice sheet. Furthermore, the SMB is strongly influenced by the topography of the ice sheet, which is most pronounced along the western coast of the AIS. If the SMB were simply a function of the temperature this topographical influence would be much smaller, and hence the SMB would be less realistic. As it is too computationally expensive to couple RACMO2/ANT to ANICE multiple times throughout the glacial cycle, we use an interpolation technique that is described below.

We use this interpolation method instead of a simple ice-core based interpolation of the temperature and SMB fields because the patterns should evolve with the topography of the ice sheet. As the topography of the ice sheet lags behind the air temperature, evolving the patterns with air temperature instead of linearly in time would change them too quickly. The changing climate (temperature and SMB)

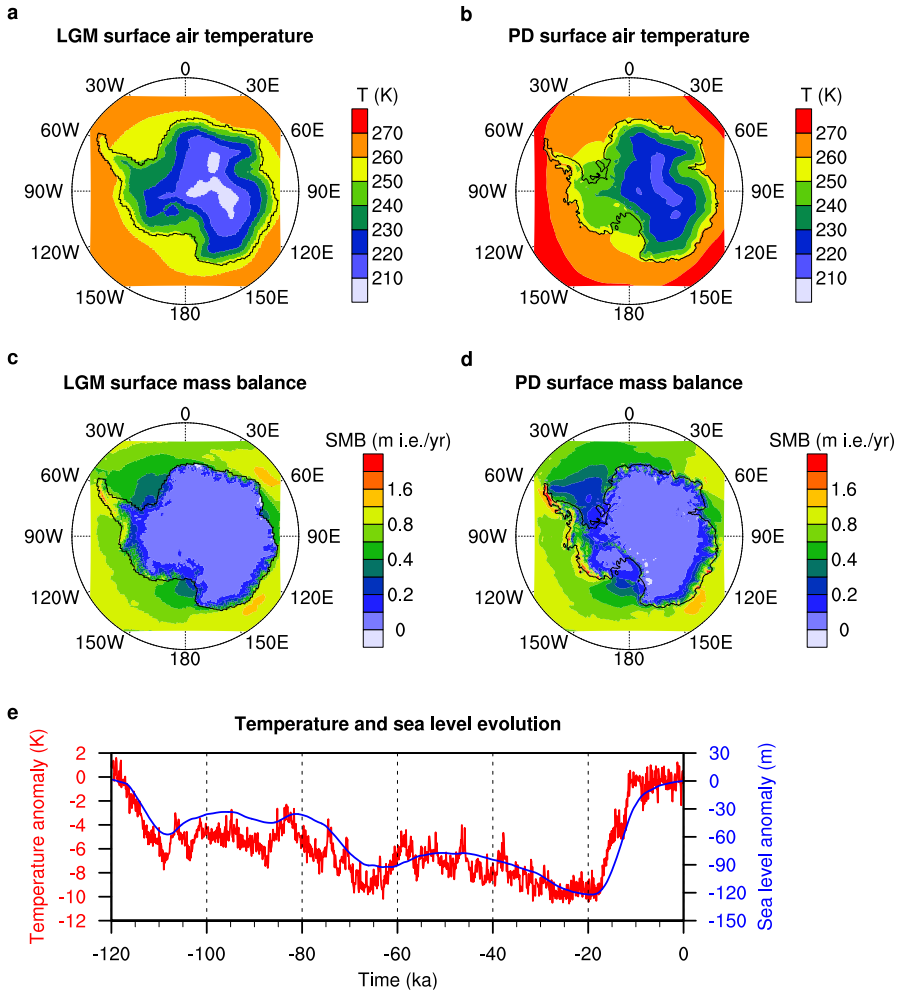


Figure 4.2: RACMO2/ANT output fields of a) the LGM temperature, b) the PD temperature, c) the LGM surface mass balance in metres ice equivalent per year and d) the PD surface mass balance, with in black the grounding line. e) The temperature evolution according to the Epica Dome C ice core (Jouzel et al, 2007) is shown in red and the sea-level evolution according to Bintanja and van de Wal (2008) in blue.

between 120 kyr ago, the LGM and the PD is derived from the two RACMO2/ANT climate states by a linear interpolation technique in three steps, which is done for each spatial point (i,j):

1. Normalisation of the data (division by the mean) to determine the temperature

and SMB patterns:

$$T_{norm}(i, j, \text{LGM}) = \frac{T(i, j, \text{LGM})}{T_{mean}(\text{LGM})}, \quad (4.1)$$

$$T_{norm}(i, j, \text{PD}) = \frac{T(i, j, \text{PD})}{T_{mean}(\text{PD})}. \quad (4.2)$$

Here, T is the temperature (in K), and the means are taken over the continent. The same equations hold for the SMB (in m i.e./yr).

2. Linear interpolation through time from one normalised state to the next. In the normalised data only the spatial patterns are visible (e.g. it is colder in the interior of the ice sheet than near the coast). With the interpolation those patterns are evolved through time. For temperature from the last interglacial (the reference (ref), where the temperature is the same as the PD temperature) to the LGM:

$$\begin{aligned} T_{norm}(i, j, t) = & \left(1 - \frac{t - t_{ref}}{t_{LGM} - t_{ref}}\right) \cdot T_{norm}(i, j, \text{PD}) \\ & + \frac{t - t_{ref}}{t_{LGM} - t_{ref}} \cdot T_{norm}(i, j, \text{LGM}). \end{aligned} \quad (4.3)$$

For temperature from the LGM to the present, where $t_{PD} = 0$:

$$\begin{aligned} T_{norm}(i, j, t) = & \left(1 - \frac{t - t_{LGM}}{-t_{LGM}}\right) \cdot T_{norm}(i, j, \text{LGM}) \\ & + \frac{t - t_{LGM}}{-t_{LGM}} \cdot T_{norm}(i, j, \text{PD}). \end{aligned} \quad (4.4)$$

Again, the same equations are applied to the SMB.

3. Multiplication by a factor in such a way that the original states remain the same. For temperature:

$$T(i, j, t) = T_{norm}(i, j, t) \cdot (T_{mean}(\text{PD}) + f_T \cdot \Delta T), \quad (4.5)$$

and for the SMB (in metres ice equivalent per year):

$$\text{SMB}(i, j, t) = \text{SMB}_{norm}(i, j, t) \cdot (\text{SMB}_{mean}(\text{PD}) + f_{\text{SMB}} \cdot \Delta T). \quad (4.6)$$

Here, ΔT is the temperature anomaly as given by the EDC ice core record from Jouzel et al (2007). The multiplication factors before ΔT are chosen in such a way that multiplying them with ΔT , they give the difference between the LGM and PD

mean values. That is,

$$f_T = \frac{T_{mean}(LGM) - T_{mean}(PD)}{\Delta T(LGM)}. \quad (4.7)$$

We use this interpolation method instead of a simple ice-core based interpolation of the temperature and SMB fields because the patterns should evolve with the topography of the ice sheet. As the topography of the ice sheet lags behind the air temperature, evolving the patterns with air temperature instead of linearly in time would change them too quickly.

The temperature anomaly 21 kyr ago was -9.2 K according to the the EDC record. Filling this in for $\Delta T(LGM)$, and subtracting the mean PD temperature of 254.8 K from the LGM mean temperature of 247.9 K, this gives a value for f_T of 0.75. The mean SMB at the LGM is 0.12 m i.e./yr and presently it is 0.21 m i.e./yr, so using

$$f_{SMB} = \frac{SMB_{mean}(LGM) - SMB_{mean}(PD)}{\Delta T(LGM)} \quad (4.8)$$

gives a value for f_{SMB} of 0.0098.

4.2.3 Oceanic forcing

The basal mass balance (BMB) of floating ice is determined by the influence of the ocean water on the ice following Holland and Jenkins (1999):

$$BMB = F_{melt} \cdot \rho_o \cdot c_{p_o} \cdot \gamma_T \cdot (T_o - T_f) / (L \cdot \rho_i). \quad (4.9)$$

The BMB depends on the difference between the water temperature (T_o) and the freezing temperature (T_f). A more detailed list of model parameters and variables, and the symbols used to represent them in this chapter, is given in Table 4.1. The ocean temperature is given by:

$$T_o = (\theta_o - 1.7) + 0.3 \cdot \Delta T - 0.12 \cdot 10^{-3} \cdot D_{shelf}. \quad (4.10)$$

The PD ocean potential temperature (θ_o), is provided by ECHAM53, from the PMIP2 project (Braconnot et al, 2007). A cross-section of θ_o at 300 m depth is shown in Figure 2.1. ECHAM53 was chosen because both the vertical and horizontal patterns match observations from the WOCE-atlas (Orsi and Whitworth III, 2004). However, θ_o is on average too high by about 1.7 degrees, so this value is subtracted from the θ_o -field. Furthermore, the coarse resolution (which is already higher in ECHAM53 than in most other GCMs) precludes the output of θ_o beneath the innermost ice shelves. Therefore, the data have been interpolated for these regions by simple inverse distance interpolation. The temperature anomaly with respect to the present (ΔT) is retrieved from the EDC ice core record, see Figure 4.2e. Furthermore, to go from potential temperature to real temperature, a lapse rate is included, multiplied by the

depth of the ice shelf (D_{shelf}). The mean lapse rate in water is $0.12 \cdot 10^{-3} \text{ K m}^{-1}$ (Knauss, 1997) and the freezing temperature is given by:

$$T_f = T_0 + 0.0939 - 0.057 \cdot S + 7.64 \cdot 10^{-4} \cdot D_{shelf}. \quad (4.11)$$

The height of the sea level changes with time and plays a key role in the evolution of the AIS (Pollard and DeConto, 2009; De Boer et al, 2013). In this study, the sea-level anomaly is taken from work by Bintanja and van de Wal (2008). They used an ice-sheet model in combination with an ocean-temperature model to extract a 3 Myr record of air temperature and sea level from benthic oxygen isotopes. The part of the record that is used in this study is presented in Figure 4.2e. This record is representative of eustatic sea-level change.

4.2.4 Varied parameters in the sensitivity experiments

Ice-flow enhancement factors

As mentioned before, the SIA and SSA velocities in ANICE are superposed to calculate the ice velocity. The SIA velocity is given by:

$$\vec{V}_{SIA} = -2(\rho_i \cdot g)^n \cdot |\nabla H_s|^{n-1} \cdot \nabla H_s \int_b^z E_{SIA} \cdot A(T^*) \cdot (H_s - z)^n d\zeta, \quad (4.12)$$

where ∇H_s is the surface slope and ζ is the scaled vertical coordinate running from the bed (b) to height z . The flow-rate factor ($A(T^*)$) depends on the temperature, which is corrected for pressure melting. The SIA enhancement factor (E_{SIA}) is varied between 7 and 11 in the sensitivity experiments. This factor determines how much the deformational flow of the ice is enhanced. There is also an SSA enhancement factor, E_{SSA} , which appears in the vertically averaged viscosity μ :

$$\mu = \frac{1}{2(E_{SSA} \cdot \bar{A})^{1/n}} \left[\left(\frac{\partial u}{\partial x} \right)^2 + \left(\frac{\partial v}{\partial y} \right)^2 + \frac{\partial u}{\partial x} \frac{\partial v}{\partial y} + \frac{1}{4} \left(\frac{\partial u}{\partial y} + \frac{\partial v}{\partial x} \right)^2 \right]^{\frac{1-n}{2n}}, \quad (4.13)$$

in the SSA velocity equations:

$$\frac{\partial}{\partial x} \left[2\mu H_i \left(2 \frac{\partial u}{\partial x} + \frac{\partial v}{\partial y} \right) \right] + \frac{\partial}{\partial y} \left[\mu H_i \left(\frac{\partial u}{\partial y} + \frac{\partial v}{\partial x} \right) \right] + \tau_{b,x} = \rho_i g H_i \frac{\partial H_s}{\partial x} \quad (4.14)$$

and,

$$\frac{\partial}{\partial y} \left[2\mu H_i \left(2 \frac{\partial v}{\partial y} + \frac{\partial u}{\partial x} \right) \right] + \frac{\partial}{\partial x} \left[\mu H_i \left(\frac{\partial v}{\partial x} + \frac{\partial u}{\partial y} \right) \right] + \tau_{b,y} = \rho_i g H_i \frac{\partial H_s}{\partial y}. \quad (4.15)$$

In Equation 4.13, \bar{A} is the vertical mean of $A(T^*)$, u and v are the SSA velocities in the x and y direction respectively, and $\tau_{b,x}$ and $\tau_{b,y}$ are the basal shear stresses in

Symbol	Description	Value	SI units
c_{p_o}	Ocean mixed layer specific heat capacity	3974	$\text{J kg}^{-1} \text{K}^{-1}$
F_{melt}	Melt parameter	$-5.0 \cdot 10^{-3}$	m s^{-1}
g	Gravitational acceleration	9.81	m s^{-2}
L	Latent heat of fusion	$3.335 \cdot 10^5$	J kg^{-1}
n	Flow exponent in Glen's flow law	3	
q	Power-law parameter for basal stress	0.3	
S	(Southern) Ocean water salinity	34.0	
T_0	Triple point of water	273.16	K
$u_{threshold}$	Threshold velocity for basal stress	100	m y^{-1}
γ_T	Thermal exchange velocity	$1.0 \cdot 10^{-4}$	m s^{-1}
ρ_a	Asthenosphere density	3300	kg m^{-3}
ρ_i	Ice density	910	kg m^{-3}
ρ_o	Ocean water density	1028	kg m^{-3}
BMB	Basal mass balance		m s^{-1}
D	Flexural rigidity		N m
D_{shelf}	Ice shelf depth		m
E_{SIA}	SIA enhancement factor		
E_{SSA}	SSA enhancement factor		
H_b	Bed elevation		m
H_i	Ice thickness		m
H_o	Sea level		m
H_s	Surface elevation		m
p_w	Pore water pressure		$\text{kg m}^{-1} \text{s}^{-2}$
m	Ice load on the bedrock		kg
SMB	Surface mass balance		m s^{-1}
T	Surface temperature		K
T_f	Freezing temperature		K
T_o	Ocean temperature		K
w	Bedrock deformation		m
ΔT	Temperature anomaly w.r.t. PD		K
μ	Ice viscosity		$\text{kg m}^{-1} \text{s}^{-1}$
θ_o	Ocean potential temperature		K
λ_p	Pore water pressure scaling factor		
τ	Bedrock relaxation time		yr
τ_b	Basal stress		$\text{kg m}^{-1} \text{s}^{-2}$
τ_c	Yield stress		$\text{kg m}^{-1} \text{s}^{-2}$
ϕ	Till friction angle		°

Table 4.1: List of used symbols, their descriptions and values and SI units when applicable

the x and y direction. E_{SSA} is varied between 0.6 and 1.0. The variations of both enhancement factors for the sensitivity experiments have been established following the work of Ma et al (2010). They suggest that the SIA enhancement factor should lie between 5 and 6, and the SSA enhancement factor should lie between 0.5 and

0.7 for ice shelves and between 0.6 and 1 for ice streams. As ANICE uses the same enhancement factor for ice streams and ice shelves, E_{SSA} has been chosen in the range of the ice streams, as these are the most important for the evolution of the AIS over time. An E_{SSA} of 5 or 6 would yield too much ice on the EAIS, therefore a range of higher values has been chosen for this parameter, see Section 4.4.

Basal stress

In ANICE, the basal stress (τ_b in Equations 4.14 and 4.15) is determined as a function of the yield stress and the basal sliding velocity, as in Bueler and Brown (2009). The basal stress is given by:

$$\tau_b = \tau_c \cdot \frac{|V_{SSA}^{q-1}|}{u_{threshold}^q} \cdot \vec{V}_{SSA}, \quad (4.16)$$

where τ_c is the yield stress:

$$\tau_c = (\tan \phi) \cdot (\rho_i g H_i - p_w), \quad (4.17)$$

and p_w is the pore water pressure:

$$p_w = 0.96 \cdot \lambda_p \cdot \rho_i \cdot g \cdot H_i. \quad (4.18)$$

Here, λ_p is a scaling factor such that the pore water pressure is maximal when the ice is resting on bedrock at or below sea level. Below sea level, the pores in the till are assumed to be saturated with water so λ_p is then equal to 1. λ_p is scaled with the height above sea level up until 1000 m. At and above 1000 m λ_p is equal to 0. Finally, the till friction angle in Equation 4.17 (ϕ) is parameterised by:

$$\phi = \begin{cases} \phi_{min} & \text{if } H_b \leq -1000, \\ \phi_{min} + (\phi_{max} - \phi_{min}) \cdot \left(1 + \frac{H_b}{1000}\right) & \text{if } -1000 < H_b < 0, \\ \phi_{max} & \text{if } 0 < H_b. \end{cases} \quad (4.19)$$

ϕ_{max} is kept constant at a value of 30° in the sensitivity experiments, ϕ_{min} is varied between 8° and 12° . ϕ_{min} determines the sliding below -1000 metres and partly between -1000 and 0 metres, and henceforth controls the sliding on large parts of the WAIS. The assumption here is that the till is weaker when situated below sea level and therefore the friction angle is smaller, and sliding more dominant. This effect can clearly be seen in Figure 4.3, where the fraction of sliding velocity with respect to the total ice velocity is shown for the reference simulation (see Section 4.3) at the PD. For ice shelves, sliding is the only displacement mechanism, so the sliding velocity is 100 % of the total velocity. Additionally, sliding is present where the bed elevation is below sea level and most dominant near the coast because the ice is thinner there.

Bedrock response

Additionally, the flexural rigidity and the relaxation time of the bedrock have been varied in the sensitivity experiments. These are parameters in the ELRA-model incorporated in ANICE. For an elastic lithosphere, not only the loading above a certain point on the lithosphere is taken into account, but also the contributions of more remote locations. The downward bedrock deformation w , created by a point load m for a (floating) elastic plate is a solution of (Le Meur and Huybrechts, 1996):

$$D\nabla^4 w = m - \rho_a g w. \quad (4.20)$$

Here, $\rho_a g w$ is the upward buoyancy force exerted on the deflected part of the lithosphere inside the asthenosphere. The deformation at a normalised distance $x = r/L_r$ from the point load is then given by:

$$w(x) = \frac{mL_r^2}{2\pi D}\chi(x), \quad (4.21)$$

with $\chi(x)$ a Kelvin function of zero order at x , r the real distance from the load m , and L_r the radius of relative stiffness, given by

$$L_r = \left(\frac{D}{\rho_a g} \right)^{1/4}. \quad (4.22)$$

In this way, a load will cause a depression within a distance of four times L_r with a minimum at the location of the load. Beyond this distance a small bulge appears. Lithospheric deformation is a linear process, so the total deflection at each point is simply calculated as the sum of the contributions of all neighbouring points within a distance of about 6 times L_r . In the sensitivity experiments, D is varied between $1 \cdot 10^{24}$ and $1 \cdot 10^{25}$ Nm, based on estimates by Stern and ten Brink (1989).

Equation 2.7 holds for an instantaneous reaction of the bedrock to a load, but in reality the adaptation to a load is delayed due to the viscosity of the asthenosphere underneath the lithosphere. We assume that the bedrock adjusts exponentially to a new loading situation. Furthermore, we state that the speed of adjustment is proportional to the difference between the equilibrium profile w and the current profile h and inversely proportional to a time constant τ :

$$\frac{dh}{dt} = \frac{1}{\tau}(w - h), \quad (4.23)$$

where w is the bedrock deflection, given by Equation 4.21, h is positive upward and τ is the Maxwell relaxation time in which the bedrock has adapted to the new load with a factor e . The relaxation time can be calculated from $\tau = \eta/G$ (Ranalli, 1995), where η is the viscosity of the upper part of the asthenosphere, in the range of 0.5 to $4 \cdot 10^{21}$ Pa s (Forte and Mitrovica, 2001) and G is the shear modulus, ranging

from 2 to $11 \cdot 10^{10}$ Pa. These numbers yield relaxation times between 150 and 6000 years approximately. Crucifix et al (2001) showed that the values used in other ice-dynamical models range from 3000 to 12000 years. However, these seem to be at the high end of geological estimates, so we varied the relaxation time between 1000 and 3000 years, after Whitehouse et al (2012).

Combining Equation 4.23 with Equation 4.21 yields a differential equation:

$$\frac{dh}{dt} = \frac{1}{\tau} \left(\sum_{i,j} \left(\frac{m_{i,j} L_r^2}{2\pi D} \chi(x_{i,j}) \right) - h \right), \quad (4.24)$$

which is solved in ANICE. Here, the sum is taken over all i,j within a distance of about six times L_r . The loading m is equal to the weight of the water column where there is no ice or where the ice is floating: $m = (H_o - H_b) \cdot \sigma \cdot \rho_o \cdot g$, with $H_o - H_b$ the height of the water column and σ the surface of the column, equal to 400 km^2 . Where the ice is grounded, m is equal to the weight of the ice: $m = H_i \cdot \sigma \cdot \rho_i \cdot g$.

4.3 The reference simulation

Before presenting the sensitivity of the model, a reference simulation is described in this section. We defined the reference simulation as the simulation that showed the best results regarding the PD grounding-line location and surface elevation, after varying the parameters used in this sensitivity study, with a climate forcing as described in Section 4.2.2 and running the model from 120 kyr ago until the PD. The settings for the reference simulation in this study are: $\phi_{min} = 10^\circ$, $E_{SSA} = 0.8$, $E_{SSA} = 9$, $D = 5.0 \cdot 10^{24} \text{ N m}$ and $\tau = 2000 \text{ yr}$. Figure 4.4a shows the modelled PD surface elevation of the AIS, and b shows the ice sheet as observed (from the ALBMAP dataset). For comparison, Figure 4.4c shows the modelled minus the observed surface elevation.

The modelled and observed surface elevation are very similar. However, the plateau of the EAIS is slightly lower in ANICE, whereas the east coast of the Weddell Sea, the Antarctic Peninsula and the region around the Amery Ice Shelf are higher (see Figure 1.1 for a map of these regions). This is probably due to the resolution of ANICE being insufficient to catch the detailed topography of these areas. Furthermore, the grounding line of the Filchner-Ronne Ice Shelf is located slightly too far inland.

The PD grounding line is shown in more detail in Figure 4.5 (red line). Also, the ALBMAP grounding line (in black) and grounding lines at other time slices are shown here. The grounding line has moved very little along the EAIS, therefore a zoom on the WAIS is shown in Figure 4.5a. The grounding line on the western side of the Antarctic Peninsula has not retreated far enough, which is probably also due to the low resolution of the model. However, the PD grounding line along most of the rest of the coast, including the Ross Ice Shelf is well modelled in ANICE. The

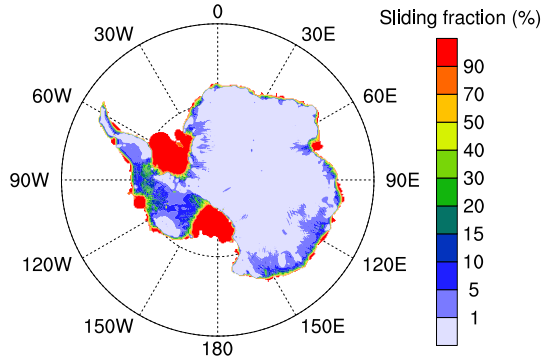


Figure 4.3: The fraction of sliding velocity ($\vec{V}_{SSA}/\vec{V}_{tot}$) with respect to the total vertically averaged ice velocity at the LGM for the reference simulation ($\phi_{min} = 10^\circ$).

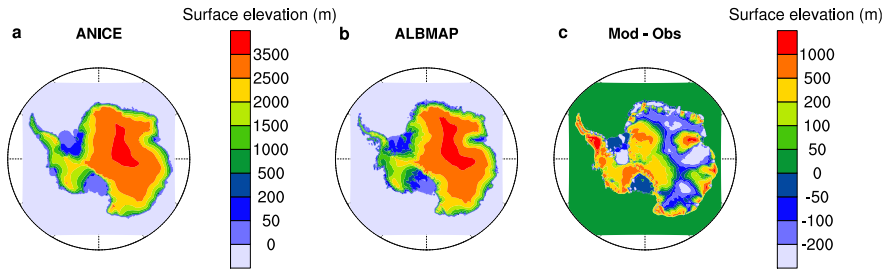


Figure 4.4: Surface elevation of the PD ice sheet *a*) as modelled, *b*) as observed (ALBMAP), and *c*) the difference between *a*) and *b*).

grounding line of the southern part of the Filchner-Ronne Ice Shelf has retreated too far inland, but the timing of the onset of retreat (around 13 kyr ago) is in agreement with Anderson et al (2002). However, a more recent study by Weber et al (2011) suggests that the onset of retreat took place around 19 kyr ago in the Weddell Sea, which indicates a too late retreat in ANICE. Additionally, they find that the margin of the ice shelf had retreated to halfway the continental shelf around 14 kyr ago and to its PD position around 11 kyr ago, which does agree with the model results. The onset of retreat of the Ross Ice Shelf is timed at 18 kyr ago in ANICE. This is in accordance with the results of Anderson et al (2002), but they indicate that the PD position of the grounding line was not reached until 7 kyr ago, while in ANICE the PD position is already reached around 10 kyr ago. Additionally, the study by McKay et al (2008) suggests a fast retreat of the Ross Ice Shelf between 11 and 10 kyr ago. This fast retreat is also modelled by ANICE, but too early by about 3 kyr.

In Figure 4.5b the grounding-line retreat in Prydz Bay (where the Amery Ice Shelf is located) is shown. There is too little retreat here, due to the coarse resolution of the model, a complication that is also described by Whitehouse et al (2012) who use

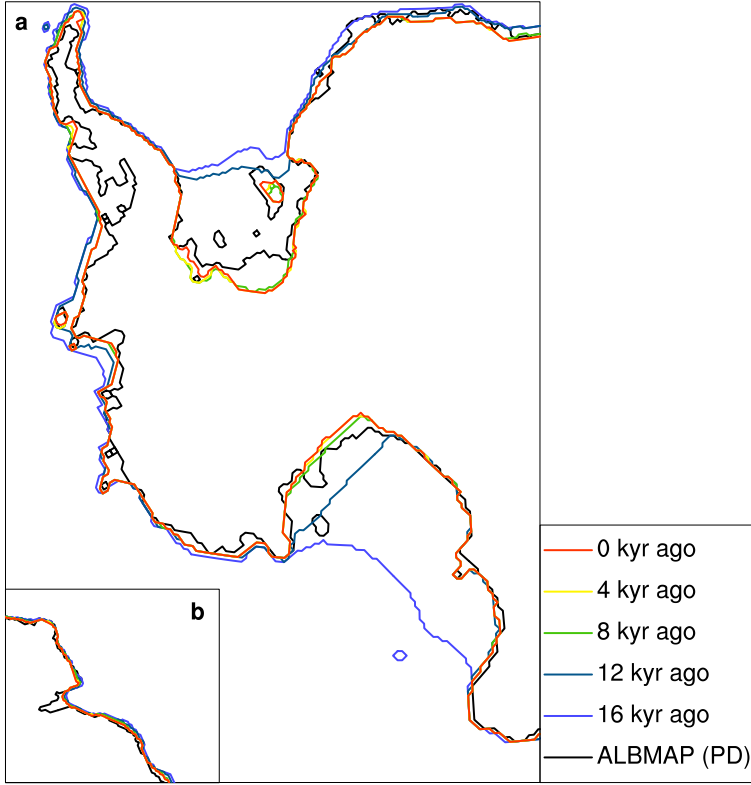


Figure 4.5: *Grounding line retreat from 16 kyr ago until the PD, with in black the PD grounding line from ALBMAP in a) West Antarctica and b) Prydz Bay (the Amery Ice Shelf region).*

a horizontal resolution of 20x20 km as well. Furthermore, the MIS-MIP (Pattyn et al, 2012) and MIS-MIP3d (Pattyn et al, 2013) experiments show that using the superposition of the SIA and the SSA velocity without a special treatment of the grounding line (e.g. using a much finer resolution around the grounding line) leads to sticking of the grounding line. The MIS-MIP experiments were done on a rather small spatial scale and by perturbing the sliding parameters instead of studying the reaction of the entire AIS on changes in the sea level and the discharge. However, the MIS-MIP experiments do indicate uncertainties in our simulation of the grounding-line motion, including the retreat in Prydz Bay.

In Section 4.4, results of the sensitivity experiments will be discussed with the aid of the evolution of the grounded ice volume for different simulations. Grounded ice volume change is attributed to SMB, BMB, ice discharge over the grounding line and grounding-line retreat or advance. These four components are shown in Figure 4.6 for the reference simulation. The BMB (in blue) gives a minor contribution to the ice volume. The SMB (in red) and the discharge over the grounding line (in

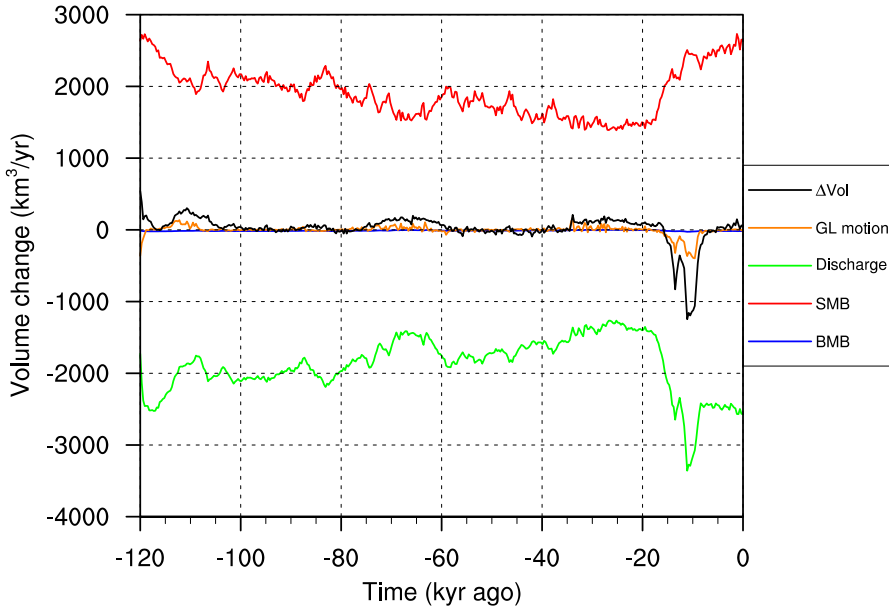


Figure 4.6: Evolution of the different contributions to grounded ice volume change (in black): Grounding line motion (orange), ice discharge over the grounding line (green), surface mass balance (red) and basal mass balance (blue).

green) give the largest contributions, but as they are opposite and almost equal, their combined contribution is approximately as large as the contribution of the grounding-line motion (in orange). Volume change (in black) is mostly positive until the LGM, due to the SMB being slightly larger than the discharge and a gradual grounding-line advance. Around 16 kyr ago the volume change becomes negative and stays negative until the mid-Holocene. In the period from 16 to 7 kyr ago the grounding line strongly retreats in the Weddell and Ross Seas (see Figure 4.5) due to sea-level rise. A lot of ice is then discharged over the grounding line, while the SMB is still growing to its PD level. At the PD, the ice discharge is almost stable, albeit more pronounced than before the LGM. Grounding line motion is negligible at the present, while the SMB seems to be still slightly growing.

4.4 Results of the sensitivity experiments

4.4.1 Ice-flow enhancement factors and basal stress

The first sensitivity experiment involves the SIA enhancement factor. The evolution in time of the WAIS and EAIS ice volume for different values of E_{SIA} is shown in Figure 4.7a. The reference simulation is represented by the black solid line and the PD ice volume by the black dashed line. The ice volume in the figure is split into

the volume of the EAIS (upper part) and of the WAIS (lower part). The figure shows clearly that higher deformational velocities (larger E_{SIA}) lead to faster ice flow and therefore to less volume. The effect of changing E_{SIA} is strongest on the EAIS, where the movement of ice is mainly driven by deformation (Figure 4.3). The PD ice volume is somewhat overestimated due to an overestimation of the ice thickness on the Antarctic Peninsula, the Amery Ice Shelf region and the east coast of the Weddell Sea (Figure 4.4c).

In the second sensitivity experiment the SSA enhancement factor has been varied as shown in Figure 4.7b. The figure shows clearly that more sliding (larger E_{SSA}) leads to less volume. This is due to sliding causing the ice on especially the WAIS to flow faster and therefore the ice sheet loses more mass. The timing of the LGM is also different for different values of E_{SSA} . This is because high ice velocities are reached earlier in time for higher values of E_{SSA} , preventing the ice sheet from advancing. Hence, the ice sheet starts retreating earlier and therefore the LGM is timed earlier than for lower values of E_{SSA} .

Between 9 kyr ago and 5 kyr ago a minimum in ice volume is visible in all simulations in Figure 4.7, especially for the EAIS volume. This dip is less pronounced in the simulations with less sliding, and it appears later. Other modelling studies that show the evolution of the grounded ice volume do not seem to find the same results (see for instance Philippon et al (2006) and Ritz et al (2001)), but there is sufficient observational evidence for a re-advance as shown by e.g. Ingólfsson et al (1998), Hall (2009), and Ackert Jr. et al (2013). From these studies it seems likely that the minimum should be timed around the mid-Holocene, which is consistent with the results for $\phi_{min} = 10$ to 12° . Most of the grounding-line re-advance in ANICE is located on the eastern and western side of the Filchner-Ronne Ice Shelf and on the western side of the Ross Ice Shelf. This is in accordance with the observations, but other re-advances that have been observed are not modelled (e.g. on the Antarctic Peninsula), due to the too coarse resolution of the model. This mid-Holocene re-advance and, at other locations, stagnation of the grounding line leads to less discharge while the surface mass balance increases due to higher temperatures. Together, these two effects lead to an increase in ice volume.

The WAIS and EAIS grounded ice volume for different values of ϕ_{min} is shown in 4.7c. More sliding (smaller ϕ_{min}) again leads to a smaller ice volume. However, the total ice volume is affected less by variations in ϕ_{min} than in E_{SSA} . This is because varying ϕ_{min} mostly affects the ice that is grounded on a bed below -1000 metres, while varying E_{SSA} affects all grounded ice below 0 metres. The mid-Holocene minimum is present in these simulations as well, and less sliding again leads to a less pronounced dip that appears later.

4.4.2 Bedrock response

The effect of changing the flexural rigidity and the relaxation time on the ice volume evolution is shown in Figure 4.7d. A thinner lithosphere implies both a smaller value

4. Model sensitivity

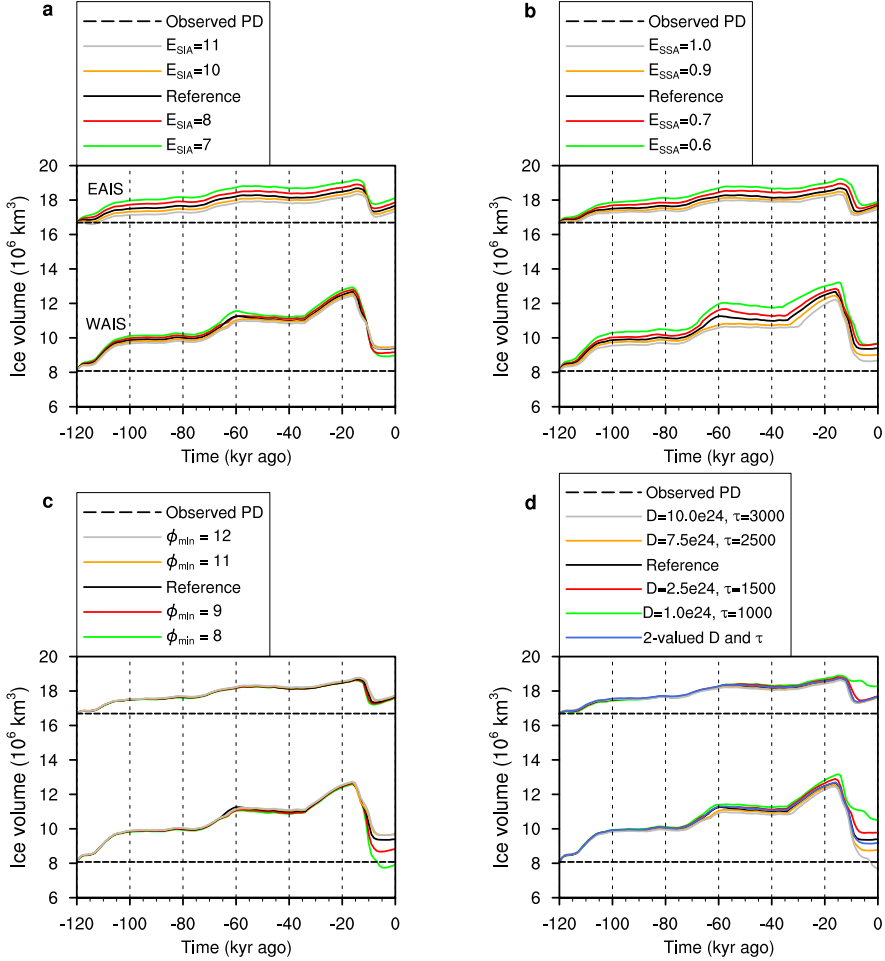


Figure 4.7: EAIS (upper lines) and WAIS (lower lines) grounded ice volume from 120 kyr ago until the present for different values of the a) SLA enhancement factor (E_{SIA}), b) SSA enhancement factor (E_{SSA}), c) sliding parameter ϕ_{min} and d) flexural rigidity (D) and relaxation time (τ), with an extra blue line indicating the simulation with $D = 5.0 \cdot 10^{24}$ Nm, $\tau = 2000$ yr for the WAIS and $D = 1.0 \cdot 10^{25}$ Nm, $\tau = 3000$ yr for the EAIS. The reference simulation (black solid line) has $E_{SIA} = 9$, $E_{SSA} = 0.8$, $\phi_{min} = 10^\circ$ and $D = 5 \cdot 10^{24}$ Nm and $\tau = 2000$ yr. Dashed lines have been drawn in black at the level of the PD grounded ice volume for both the EAIS and the WAIS.

for D and for τ . As these two parameters are coupled, we chose to show the simulations where both parameters have been changed in the same direction. However, we have done simulations with independently varied D and τ and it should be noted that the effect of varying D is smaller than the effect of varying τ , which indicates that the speed of the lithosphere reaction is more important for the evolution of the ice sheet than the amplitude.

From Figure 4.7d it is clear that a thinner lithosphere leads to a higher PD ice volume, especially on the WAIS. Here, the largest changes in ice loading take place (relative with respect to the EAIS), so it makes a large difference how much and how fast the bedrock elevation adapts to changes in the ice loading. A less rigid and faster reacting bedrock leads to faster rebound of the bedrock after the ice has retreated. This induces a shallower grounding-line and therefore a reduction in the ice flux across the grounding line and eventually a larger PD ice volume. Figure 4.7d also shows the results of a simulation that assumes a thinner lithosphere under the WAIS than under the EAIS, as observed by e.g. Morelli and Danesi (2004). The values for D and τ in this simulation are $D = 5.0 \cdot 10^{24}$ Nm, $\tau = 2000$ yr for the WAIS and $D = 1.0 \cdot 10^{25}$ Nm, $\tau = 3000$ yr for the EAIS. On the EAIS the effect is insignificant, but on the WAIS the effect is visible. The WAIS ice volume for this extra simulation is close to that of the reference simulation because the reference values for D and τ are used for this part of the ice sheet, but it is influenced by the higher values for D and τ used for the EAIS, leading to a slightly smaller PD ice volume.

For the EAIS, there seems to be a threshold value between $D = 1.0 \cdot 10^{24}$ Nm, $\tau = 1000$ yr and $D = 2.5 \cdot 10^{24}$ Nm, $\tau = 1500$ yr, where the ice sheet hardly shrinks from the LGM to the PD. Because of this, the simulation with $D = 1.0 \cdot 10^{24}$ Nm, $\tau = 1000$ yr is not regarded as realistic. The bedrock model parameters also have an influence on the ice volume minimum in the mid-Holocene. A thinner lithosphere causes a less pronounced dip which occurs later.

4.4.3 Ice volume and grounding-line retreat

In ALBMAP, the PD WAIS grounded ice volume is $8.1 \cdot 10^6$ km³ and the EAIS volume is $16.7 \cdot 10^6$ km³. Together they make up $24.8 \cdot 10^6$ km³ of ice for the entire AIS. Both the WAIS and the EAIS PD grounded ice volume are overestimated, by $1.3 \cdot 10^6$ km³ and $0.7 \cdot 10^6$ km³ respectively. A large part of the overestimation of the WAIS volume (about 30%) is due to a too low resolution to model the topography of the Antarctic Peninsula correctly, which can be seen from Figure 4.4c.

The additional grounded ice volume present on the AIS during the LGM is estimated to be between 14 m and 24.5 m sea-level equivalent (s.l.e.), or 5.6 to $9.8 \cdot 10^6$ km³ by Clark and Mix (2002), about 8 m s.l.e. or $3.2 \cdot 10^6$ km³ by Whitehouse et al (2012) and Golledge et al (2013), between 6.3 and 10.5 m s.l.e. or between 2.5 and $4.2 \cdot 10^6$ km³ by Briggs and Tarasov (2013) and between 7 and 12 m s.l.e. or between 2.8 and $4.9 \cdot 10^6$ km³ by Gomez et al (2013). This means there was 27.3 to $34.6 \cdot 10^6$ km³ of ice present on the AIS at the LGM. For all simulations the total AIS LGM ice volume falls within this range; the LGM grounded ice volume from our sensitivity simulations ranges between 30.5 and $32.4 \cdot 10^6$ km³. If the extremes are not taken into account (i.e. the results for $\phi_{min} = 8^\circ$, $\phi_{min} = 12^\circ$, $E_{SIA} = 7$, $E_{SIA} = 11$, $E_{SSA} = 0.6$, $E_{SSA} = 1.0$ and the upper and lower values for D and τ), to filter out unrealistic simulations like the simulation with $D = 1.0 \cdot 10^{24}$ Nm, $\tau = 1000$ yr (see Section 4.4.2), the LGM grounded ice volume ranges between 31.0

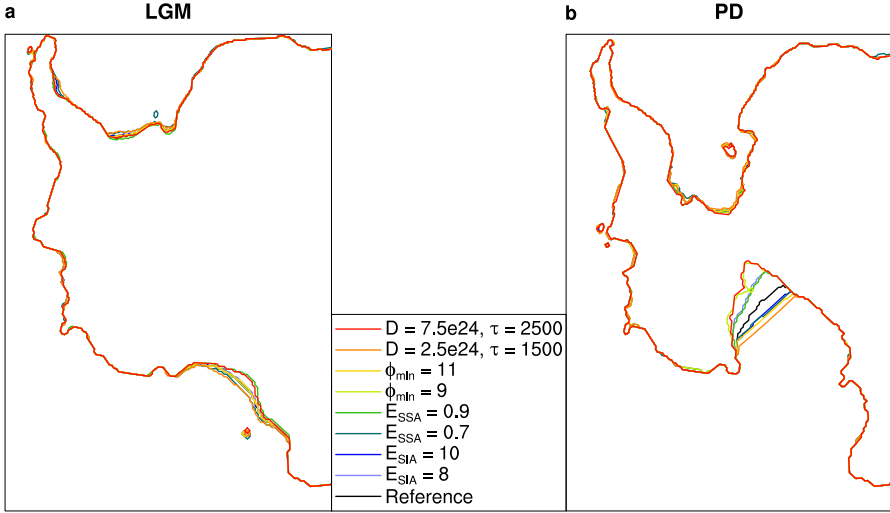


Figure 4.8: Grounding line positions at a) the LGM, 16 kyr ago and b) the PD, for the reference simulation and for simulations with variations of the indicated parameters.

and $31.8 \cdot 10^6 \text{ km}^3$. For these simulations, the change in ice volume from the LGM to the PD is $-4.3 \pm 0.5 \cdot 10^6 \text{ km}^3$, which is equivalent to $10.7 \pm 1.3 \text{ m s.l.e.}$ and falls within the range found in the literature. Our model predicts that the maximum ice volume on the AIS was reached between 15 and 16 kyr ago, which is in good agreement with e.g. Verleyen et al (2005), who found that the maximum ice volume occurred at 16 kyr ago.

A comparison of the grounding-line positions at the LGM and the PD for different values of the investigated parameters is shown in Figure 4.8. At the LGM, there is not much difference between the grounding-line positions because they are all close to the continental shelf and hence cannot advance further. Anderson et al (2002) and Denton and Hughes (2002) both show LGM grounding-line reconstructions, which agree with our modelled grounding-line positions. However, the grounding lines for the simulations with $D = 7.5 \cdot 10^{24} \text{ Nm}$, $\tau = 2500$ and the $E_{SSA} = 0.9$ simulations seem to be located slightly too far inland in the Ross Sea. The PD grounding-line locations only vary substantially in the Ross Sea, indicating that the Ross Ice Shelf is more sensitive than the Filchner-Ronne Ice Shelf. The location of the grounding line is strongly correlated with the WAIS ice volume, i.e. a lower WAIS ice volume with respect to the reference simulation is connected to a grounding line that is situated further inland.

4.5 Conclusions

We investigated the effect of the friction angle of the bed below sea level, the SSA and SIA enhancement factors and the flexural rigidity and the relaxation time of the bedrock on the evolution of the AIS. We did this by first defining a reference simulation with the following settings of the studied parameters: $\phi_{min} = 10^\circ$, $E_{SSA} = 0.8$, $E_{SSA} = 9$, $D = 5.0 \cdot 10^{24}$ N m and $\tau = 2000$ yr. The reference simulation gives satisfactory results for the LGM and the PD. The effect of the aforementioned parameters has been tested by doing sensitivity experiments.

The effect of the amount of sliding on the ice sheet has been studied by changing two different parameters, the friction angle of the bed below sea level (ϕ_{min}) and the SSA enhancement factor (E_{SSA}). More sliding generally leads to less volume due to the ice flowing faster away from the ice sheet. Between the LGM and the PD the AIS loses mass until a minimum ice volume is reached around the mid-Holocene (5-6 kyr ago) after which the ice re-advances. The timing and the strength of this minimum is dependent on the amount of sliding, where less sliding leads to a less pronounced and later minimum. These results are in good agreement with observations, which point out that the onset of this re-advance was indeed timed in the mid-Holocene.

Furthermore, we studied the effect of changing the SIA enhancement factor (E_{SIA}) and two bedrock model parameters on the ice sheet. The effect of the SIA enhancement factor is mostly seen on the EAIS, where the ice moves due to deformation. A larger value of E_{SIA} leads to less volume over the entire simulation period from 120 kyr ago to the present.

The effect of the changes in the flexural rigidity and the relaxation time of the bedrock are most pronounced on the WAIS where the largest changes in ice loading take place. A thinner lithosphere (modelled by a smaller flexural rigidity and relaxation time) leads to a higher PD ice volume due to a faster rebounding of the bed, which causes a shallower grounding line and therefore a reduction in the ice flux across the grounding line.

We compared grounding-line positions for different sensitivity experiments. From this we conclude that the grounding-line position at the LGM is not very sensitive to changes in the investigated parameters. For the PD ice sheet the largest differences occur for the grounding line in the Ross Sea. The grounding-line position is correlated to the WAIS ice volume, where a smaller PD ice volume is connected to a grounding line located further inland.

The maximum grounded ice volume for the entire AIS occurred between 15 and 16 kyr ago and lies between 30.5 and $32.4 \cdot 10^6$ km³, which is within the range of 27.3 to $34.6 \cdot 10^6$ km³ found in the literature. The PD grounded ice volume is overestimated in the model by about 8%, which is probably mainly due to the fact that with a resolution of 20x20 km the details of the topography of the Antarctic Peninsula and the Amery Ice Shelf area cannot be modelled correctly. The difference between the modelled LGM and the PD grounded ice volume is $-4.3 \pm 0.5 \cdot 10^6$ km³,

equivalent to 10.7 ± 1.3 m s.l.e., which is also within the range found in the literature (6.3 to 24.5 m s.l.e.)

We conclude that ANICE performs well, regarding the PD grounding line, grounding-line retreat and LGM grounded ice volume. The optimal set of parameters we used in this study to define the reference simulation can be applied to study the deglaciation of the AIS from LGM to PD in more detail. In such a subsequent study it would be interesting to perform ensemble runs and compare results from ANICE to observations, as has been done by e.g. Briggs et al (2013).

Acknowledgements

The figures in this chapter were produced with NCL (UCAR/NCAR/CISL/VETS, 2013). We thank SURFsara (www.surfsara.nl) for the support in using the Cartesius Compute Cluster. Furthermore, computational resources required for experiments with HadCM3 have been provided by the supercomputing facilities of the Universit  catholique de Louvain (CISM/UCL). We also want to thank an anonymous reviewer, James Fastook and the editor, Eric Larour for their suggestions and detailed comments, which led us to significant improvements of the manuscript.

CHAPTER 5

The effect of climate and sea-level change on the evolution of the Antarctic Ice Sheet from the Last Glacial Maximum until 2100

Due to a scarcity of observations and its long memory of uncertain past climate, the Antarctic Ice Sheet remains a largely unknown factor in the prediction of global sea-level change. As the history of the ice sheet plays a key role in its future evolution, in this study we model the Antarctic Ice Sheet from the Last Glacial Maximum (21 kyr ago) until the year 2100 with the ice-dynamical model ANICE. We force the model with different temperature, surface mass balance and sea-level records to investigate the importance of these different aspects for the evolution of the ice sheet. Additionally, we compare the model output from 21 kyr ago until the present with observations to assess model performance in simulating the total grounded ice volume and the evolution of different regions of the Antarctic Ice Sheet. Although there are some clear limitations of the model, we conclude that sea-level change has driven the deglaciation of the ice sheet, whereas future temperature change and the history of the ice sheet are the primary cause of changes in ice volume in the future. We estimate the change in grounded ice volume between its maximum (around 15 kyr ago) and the present-day to be between 8.4 and 12.5 m sea-level equivalent and the contribution of the Antarctic Ice Sheet to the global mean sea level in 2100, with respect to 2000, to be -22 to 63 mm.

This chapter is based on: A model study of the effect of climate and sea-level change on the evolution of the Antarctic Ice Sheet from the Last Glacial Maximum to 2100, by M. N. A. Maris, J. M. van Wessem, W.J. van de Berg, B. de Boer, J. Oerlemans, *Climate Dynamics*, doi: 10.1007/s00382-014-2317-z.

5.1 Introduction

The Antarctic Ice Sheet (AIS) remains an uncertain factor in predicting global sea-level change (Church et al, 2014). The scarcity of observations and its long memory of largely unknown past climate change play a key role in the uncertainty of the future of the ice sheet (Huybrechts et al, 2004; Bentley, 2010). Other studies found a likely contribution to sea-level rise over the 21st century of -190 to 50 mm (Huybrechts et al, 2004), 0 to 144 mm (Bindschadler et al, 2013), and -20 to 185 mm (Little et al, 2013). However, these studies had their shortcomings: Little et al (2013) kept the Surface Mass Balance (SMB) constant, whereas the change in SMB over the coming century will probably be of the same order of magnitude as the dynamical change (Church et al, 2014, Table 13.5). Huybrechts et al (2004) and Bindschadler et al (2013) did allow for the SMB to change but both used only one emission scenario. Therefore, in this study we investigate how the AIS reacts to the four future climate scenarios (Representative Concentration Pathways or RCP scenarios) as proposed by the IPCC AR5 (Collins et al, 2014) using the ice-dynamical model ANICE.

Predictions of the future sea-level contribution have mainly focussed on different mass balance components of the AIS until now (Church et al, 2014). However, from these techniques it is hard to take into account the ice-dynamical change of the AIS and the memory of past climate and sea-level change to which the ice sheet is still reacting as well (Huybrechts et al, 2004; Bentley, 2010). Therefore, it is relevant to investigate the effect of different past climate reconstructions on the evolution of the ice sheet. For example, Briggs et al (2013) investigated the effect of different temperature and SMB parameterisations from which they concluded that changing the climate forcing parameters has a relatively large impact compared to changing other model parameters such as the sliding and calving coefficients. However, they did not vary the sea-level forcing. In this study, we use temperature and sea-level reconstructions from various sources to evaluate the AIS evolution from the Last Glacial Maximum (LGM) to the present-day (PD). All simulations from LGM to PD are then continued until 2100 using the four RCP scenarios to study the influence of the climatic history of the ice sheet on its future evolution.

To assess the performance of ANICE, its output is compared to observations from the AntIcedat database (Briggs and Tarasov, 2013) for the past and to the ALBMAP dataset (Le Brocq et al, 2010) for the present. The evaluation technique is described in Section 5.2.2 and follows Briggs and Tarasov (2013). Through this assessment we gain some insight into the performance of the model regarding different regions of the AIS and its total ice volume.

5.2 Methods

ANICE is a finite distance ice-dynamical model, run at a 20 km horizontal resolution, which comprises the AIS and a large part of the Southern Ocean, see e.g. Figure 5.1a

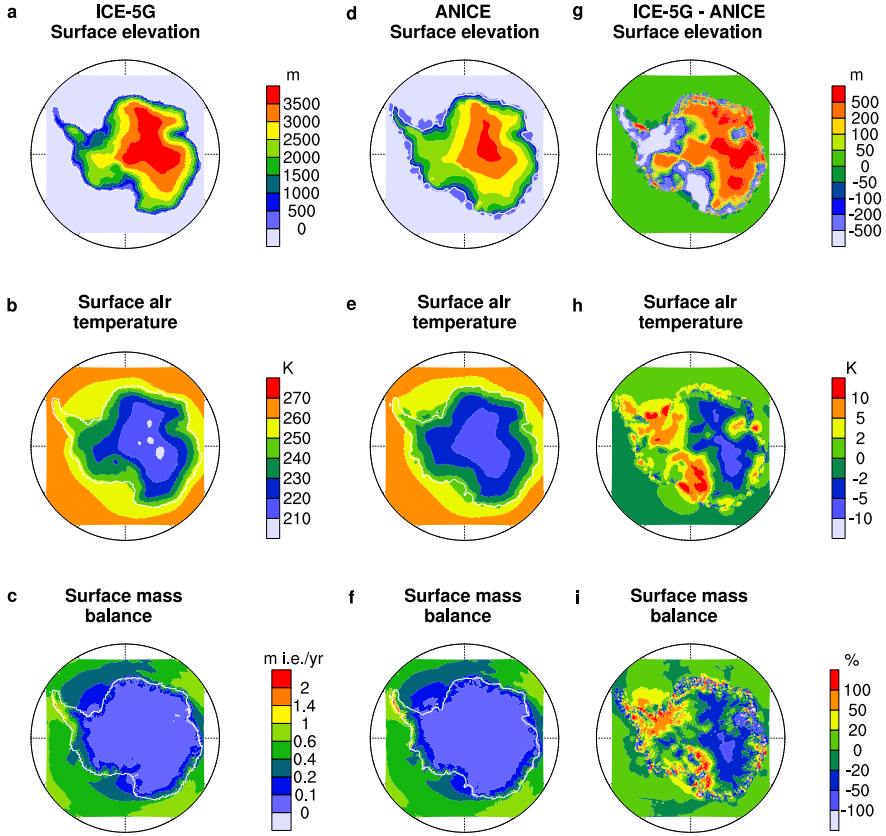


Figure 5.1: Input surface elevation into RACMO2/ANT based on a) ICE-5G and d) ANICE output, with g) the difference field (ICE-5G - ANICE). Output of RACMO2/ANT: b) and e) surface air temperature in Kelvin, with h) the difference field and c) and f) SMB in metres ice equivalent (m.i.e.) per year, with i) the difference field as a percentage of the SMB in f, from RACMO2/ANT with the ANICE surface elevation.

where the light blue square indicates the ANICE domain. The vertical levels in the model are split between levels in the ice, the bedrock and the ocean. The ice thickness is divided into 14 levels, with a spacing of 10 % of the ice thickness at the top and 1% of the ice thickness at the bottom to ensure a higher vertical resolution at the base of the ice. The bedrock is modelled until a depth of 1500 metres, divided into 5 evenly spaced levels. The ocean has a vertical resolution of 100 metres, and is modelled until a depth of 3000 metres.

In ANICE the evolution of the AIS is externally forced by, amongst others, air and ocean water temperature, SMB and sea-level height. These forcings will be discussed individually for the period from the LGM to the PD in Section 5.2.1 and for the period from the PD until 2100 in Section 5.2.3.

ANICE initialisation

ANICE is initialised at the LGM with the result of a spin-up from 120 kyr ago until the PD (see Chapter 4). This spin-up was done with a PD temperature and SMB at 120 kyr ago and 0 kyr ago, from the regional atmospheric climate model RACMO2/ANT (see Section 5.2.1). The climate from RACMO2/ANT for the LGM (21 kyr ago) was based on a smoothed ICE-5G topography (Peltier, 2004). Interpolation between the climate states was achieved with the EDC ice-core temperature reconstruction and the sea-level record was taken from Bintanja and van de Wal (2008). In Chapter 4, sensitivity experiments have been carried out by changing different flow parameters in ANICE. The LGM ice sheet from the simulation with the best fitting set of parameters (regarding PD grounding-line position and ice volume evolution) has been chosen to provide RACMO2/ANT with an LGM topography for this study and to initialise ANICE.

5.2.1 Climate forcing LGM-PD

Air temperature and SMB

The air temperature and the SMB are derived from a combination of two climate states, one at the LGM and one at the PD, from the most recent version of the regional atmospheric climate model RACMO2/ANT (Van Meijgaard et al, 2008) and a temperature reconstruction from an ice core. RACMO2/ANT is preferred over a general circulation model (GCM) because it simulates a more realistic Antarctic climate due to its higher horizontal resolution and the incorporation of more physical processes (Ligtenberg et al, 2013). When forced with re-analysis data for the recent past, RACMO2/ANT has yielded realistic results for the temperature and the SMB over Antarctica, compared to in-situ observations (Van de Berg et al, 2006; Lenaerts et al, 2012b). For the simulation of the Antarctic LGM climate, RACMO2/ANT is forced with a GCM simulation from HadCM3, see Chapter 4.

RACMO2/ANT is run over 30 years for both the LGM and the PD to yield a representative climate state at both times. It uses the ice-sheet topography as input to calculate the temperature and SMB fields. However, the ice-sheet topography is not well known for the LGM. Therefore, we have used two different topographies as boundary conditions for the LGM climate simulations with RACMO2/ANT. The first topography is the smoothed version of the ICE-5G topography and the second topography is derived with ANICE by the spin-up simulation.

The two LGM topographies, temperature and SMB-output are shown in Figure 5.1. Figure 5.1a, b and c show the ICE-5G topography with the resulting temperature and SMB fields, whereas Figure 5.1d, e and f show the ANICE topography with the resulting temperature and SMB fields. Figure 5.1g, h and i show the differences between the RACMO2/ANT simulations with ICE-5G and ANICE topography. The main differences between the two topographies are the elevation

of the Antarctic Peninsula and of the East-Antarctic plateau. The plateau is higher in ICE-5G and probably overestimated, as it should be somewhat lower than at the PD (e.g. Ritz et al, 2001). ANICE probably overestimates the ice surface elevation on the Antarctic Peninsula because of the limited horizontal resolution, which makes the detailed topography in this region hard to capture by the model. Because of the high elevation of the East Antarctic Ice Sheet (EAIS) in ICE-5G, the surface air temperature is lower there than for the ANICE topography. The SMB is lower on the EAIS for the ICE-5G topography for the same reason, while the orographically enhanced precipitation on the Antarctic Peninsula makes the SMB higher for the ANICE topography.

The LGM and PD fields given by RACMO2/ANT and the ice core temperature reconstructions are combined as in Chapter 4:

1. Normalisation of the data (division by the mean) to determine the temperature and SMB patterns.
2. Linear interpolation through time from one normalised state to the next. In the normalised data only the spatial patterns are visible. With the interpolation those patterns are evolved through time.
3. Multiplication by a factor dependent on the temperature anomaly (as given by an ice core record) in such a way that the original states remain the same.

The equations for temperature and SMB over time are:

$$T(t) = T_{norm}(t) \cdot (T_{mean}(PD) + f_T \cdot \Delta T), \quad (5.1)$$

and for the SMB (in metres ice equivalent per year):

$$SMB(t) = SMB_{norm}(t) \cdot (SMB_{mean}(PD) + f_{SMB} \cdot \Delta T). \quad (5.2)$$

Here, T_{norm} and SMB_{norm} are the interpolated, normalised temperature and SMB fields and

$$f_T = \frac{T_{mean}(PD) - T_{mean}(LGM)}{\Delta T(LGM)}, \quad (5.3)$$

$$f_{SMB} = \frac{SMB_{mean}(PD) - SMB_{mean}(LGM)}{\Delta T(LGM)}. \quad (5.4)$$

For the PD, the mean temperature is 254.8 K, and the mean SMB is 0.21 m i.e./yr. The mean temperature and SMB at the LGM depend on the used RACMO2/ANT-output (with ICE-5G topography or with ANICE topography). The values for T and SMB at the LGM are indicated in Table 5.1. Furthermore, the table shows the values of the factors f_T and f_{SMB} for each of the four used ice cores for the two RACMO2/ANT-output fields.

Topography	ICE-5G		ANICE	
	Mean $T_{21} = 247.82$ K Mean $SMB_{21} = 0.104$ m yr ⁻¹		Mean $T_{21} = 247.05$ K Mean $SMB_{21} = 0.106$ m yr ⁻¹	
Ice core record	f_T	f_{SMB}	f_T	f_{SMB}
EDC	0.76	0.0108	0.84	0.0106
Fuji	0.90	0.0128	0.99	0.0125
Vostok	0.87	0.0123	0.96	0.0121
WDC	0.89	0.0127	0.99	0.0124

Table 5.1: f_T and f_{SMB} factors for combinations of the four used temperature reconstructions with the two different topographies used in RACMO2/ANT to produce a climate state at 21 kyr ago (the ICE-5G and the ANICE topography). Average values of the temperature and the SMB are also shown for both topographies.

The ice core reconstructions we use in this study are Epica Dome C (EDC, Jouzel et al, 2007), Fuji (Kawamura et al, 2007), Vostok (Petit et al, 1999) and the West Antarctic Divide Core (WDC, WAIS Divide Project Members, 2013). The WDC ice core has been drilled very recently, so a complete temperature reconstruction is not available yet. Therefore, we assume a linear relation between the available $\delta^{18}O$ -record and the temperature, with a temperature of -8°C at 21 kyr ago, following Figure S3 of the supplementary material of WAIS Divide Project Members (2013). The reconstructions are shown in Figure 5.2a-d. These temperature reconstructions do not differ much from each other, except for the WDC reconstruction which gives a higher temperature at 21 kyr ago. Thereafter temperature increases more slowly for this reconstruction, so it gives lower temperatures from about 15 kyr ago until the PD.

Sea level and ocean temperature

Additionally, we use two different sea-level reconstructions. The first sea-level record comes from SPECMAP (Imbrie et al, 1984), for which the spectral properties of deep-sea sediments have been studied to reconstruct past sea levels. The second sea-level record comes from Bintanja and van de Wal (2008). They used an ice-sheet model in combination with an ocean-temperature model to extract a 3 Myr record of air temperature and sea level from benthic oxygen isotopes. The two sea-level reconstructions are both eustatic sea-level records and are shown in Figure 5.2e and f. The SPECMAP record starts out with a higher sea level than the record from Bintanja and van de Wal (2008), but rises more slowly. Therefore, the sea level from SPECMAP becomes lower from about 15 kyr ago. Frankcombe et al (2013) describe a coupling process between the AIS and the westerlies over the Southern Ocean which also caused the sea level to rise between the LGM and the PD. However, this process has not been taken into account in this study as the additional sea-level rise is only 0.5 m, which is negligible compared to the 120 m total sea-level rise and falls within the uncertainties of the records from SPECMAP and Bintanja and van de Wal

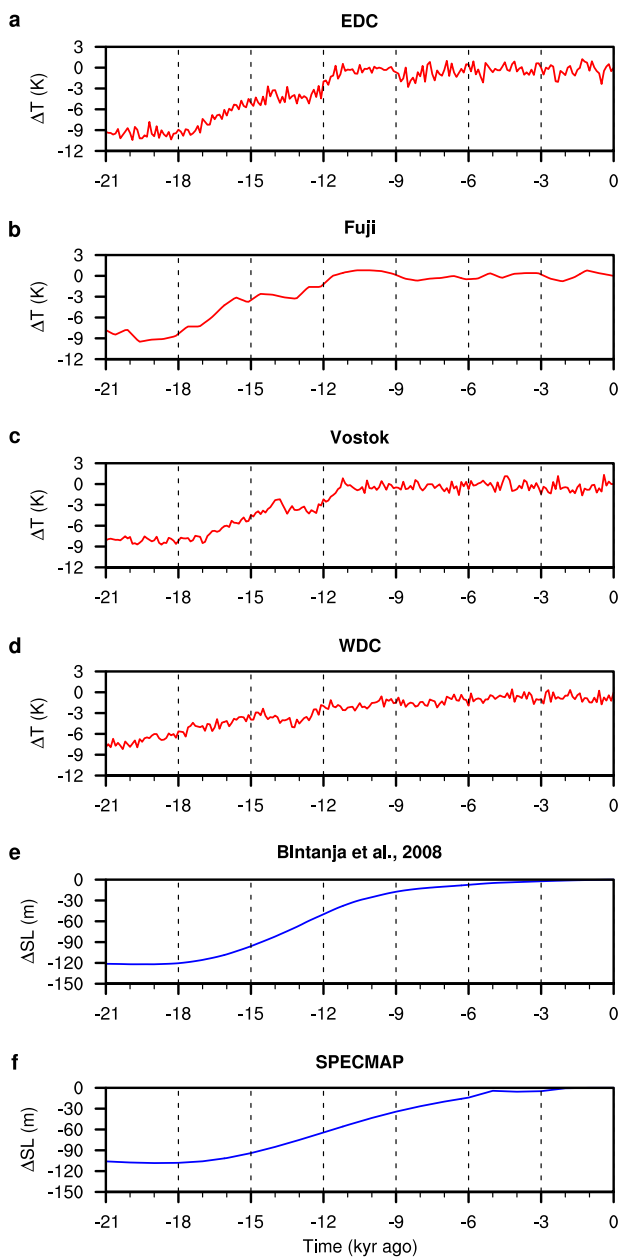


Figure 5.2: *a-d)* Ice core temperature anomaly reconstructions with respect to the PD from 21 kyr ago to present. *e-f)* Sea-level anomaly reconstructions with respect to the PD from 21 kyr ago to present.

(2008).

The ocean-water temperature is dependent on the air temperature, and hence

on the used temperature reconstruction, through:

$$T_o = (\theta_o - 1.7) + 0.3 \cdot \Delta T - 0.12 \cdot 10^{-3} \cdot D_{shelf}. \quad (5.5)$$

Here, ΔT is the air temperature anomaly and D_{shelf} is the ice shelf depth, multiplied by the mean lapse rate in water of $0.12 \cdot 10^{-3} \text{ K m}^{-1}$ (Knauss, 1997). The ocean potential temperature, θ_o , is provided by ECHAM53 from the PMP2 project (Brannon et al, 2007). ECHAM53 was chosen because both the vertical and horizontal patterns match observations from the WOCE-atlas (Orsi and Whitworth III, 2004). However, θ_o is too high by about 1.7 degrees, and the coarse resolution (which is already higher than for most other GCMs) disables the output of θ_o beneath the innermost ice shelves. Therefore, the data have been interpolated for these regions by simple inverse distance interpolation. Note that the temperature is adjusted through a scaling ($0.3 \cdot \Delta T$) instead of using the aforementioned interpolation technique. The scaling factor of 0.3 compares well with Waelbroeck et al (2009), who found a sea surface temperature of 2 to 4 degrees lower during the LGM and at the PD. However, Annan and Hargreaves (2013) find a sea surface temperature of only 1 degree lower to 2 degrees higher at the the LGM with respect to the PD, probably due to the insulating effect of sea ice.

The ocean-water temperature partly determines the basal mass balance (BMB) of floating ice (Holland and Jenkins, 1999):

$$\text{BMB} = F_{melt} \cdot \rho_o \cdot c_{p_o} \cdot \gamma_T \cdot (T_o - T_f) / (L \cdot \rho_i), \quad (5.6)$$

where F_{melt} is the melt parameter, equal to $-5.0 \cdot 10^{-3} \text{ m s}^{-1}$, $\rho_o = 1028 \text{ kg m}^{-3}$ is the ocean-water density, $c_{p_o} = 3974 \text{ J kg}^{-1} \text{ K}^{-1}$ is the ocean mixed layer specific heat capacity, $\gamma_T = 1.0 \cdot 10^{-4} \text{ m s}^{-1}$ is the thermal exchange velocity and T_f is the freezing temperature given by:

$$T_f = T_0 + 0.0939 - 0.057 \cdot S + 7.64 \cdot 10^{-4} \cdot D_{shelf}. \quad (5.7)$$

Here, $T_0 = 273.16 \text{ K}$ is the triple point of water and $S = 34$ is the ocean-water salinity.

Performed simulations

The two LGM topographies in RACMO2/ANT, together with four ice-core temperature reconstructions and two sea-level records give a total of 16 standard simulations. To understand the significance of the temperature and the sea-level reconstructions, we carried out two additional experiments with either the sea level or the temperature kept constant at its LGM level. Furthermore, one simulation combines the EDC-reconstruction for the EAIS and the WDC-reconstruction for the WAIS. The separation between the EAIS and the WAIS runs from the top left of the domain to the bottom right as: $30^\circ \text{W} \rightarrow 86^\circ \text{S} \rightarrow 160^\circ \text{E}$, see Figure 5.3b.

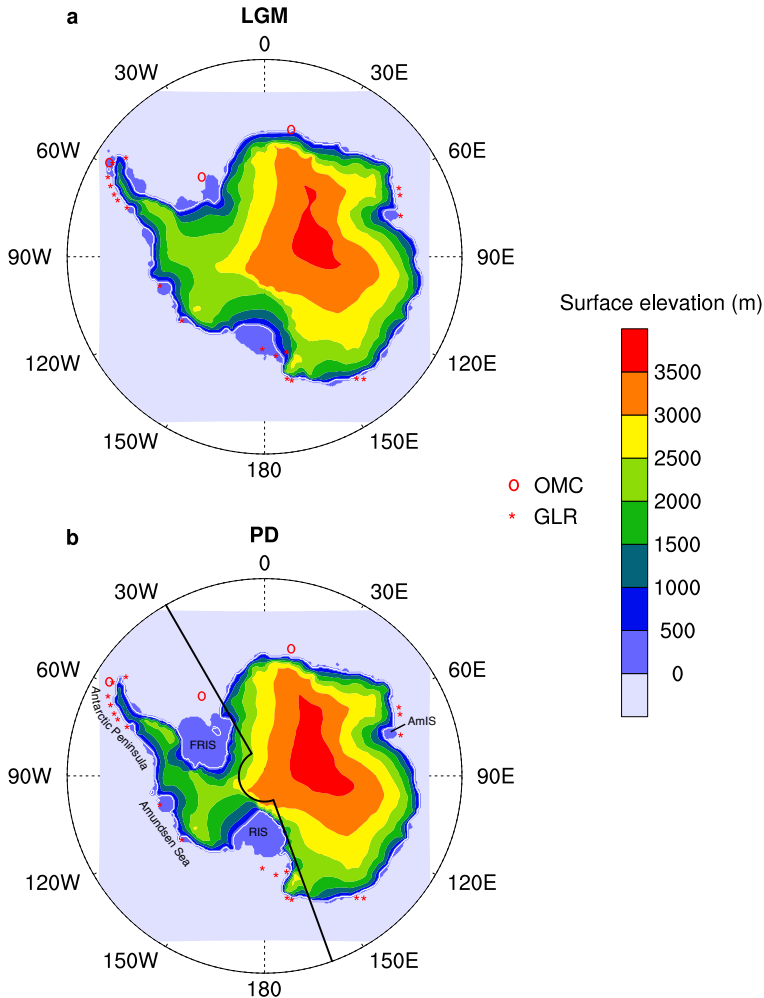


Figure 5.3: Surface elevation of the AIS *a*) at its maximum ice volume (15 kyr ago) and *b*) at the PD from the IFS simulation with in black the division between the WAIS and the EAIS and the names of some regions and of the three major ice shelves (RIS = Ross Ice Shelf, FRIS = Filchner-Ronne Ice Shelf and AmIS = Amery Ice Shelf). The locations of the used OMC and GLR-observations from the AntICEdat database are indicated with red circles and stars respectively and the grounding line is illustrated by the white line.

5.2.2 Evaluation method

The model results are compared to observations from the database AntICEdat (Briggs and Tarasov, 2013). This dataset provides dates for the onset of open marine conditions (OMC), grounding-line retreat (GLR), and ice thickness at certain locations on and around the AIS. The locations of these observations are indicated in Figures 5.3a and b (ice extent, which combines the OMC and GLR observations)

and 5.6b (ice thickness). There are 22 ice extent observations and 92 ice thickness observations (divided over 24 regions) that fall within the studied period of 21 kyr ago until the PD. Additionally, observations of relative sea-level rise are available, but as two different sea-level reconstructions are prescribed in this study and inter-compared (instead of solving the sea-level equation), results would depend too much on the sea-level record instead of the modelled evolution of the ice sheet. Therefore, the relative sea-level rise observations are not used here.

Additionally, we compared the PD output of ANICE with the ALBMAP dataset (Le Brocq et al, 2010), which has been re-gridded on the ANICE grid, and henceforth called ALBMAP₂₀. The PD comparison consists of three aspects, following the method of Briggs and Tarasov (2013):

- The surfaces of the three largest ice shelves: the Ross Ice Shelf (RIS, $4.15 \cdot 10^5$ km²), the Filchner-Ronne Ice Shelf (FRIS, $3.86 \cdot 10^5$ km²) and the Amery Ice Shelf (AmIS, $4.8 \cdot 10^5$ km²).
- The mean ice thickness of the EAIS (2325 m), the grounded part of the WAIS (2193 m) and the floating part of the WAIS (374 m).
- The location of the eastern grounding line of the RIS at 81 °S (in ALBMAP₂₀ it is at 155 °W)

The comparison makes use of misfit scores which are calculated for the ice extent in the following way:

$$\text{Misfit}_{\text{EXT}} = \frac{1}{22} \cdot \sum_i \frac{(\text{Age}_{\text{mod}}(i) - \text{Age}_{\text{obs}}(i))^2}{\sigma(i)^2}, \quad (5.8)$$

with every i representing an observation, and the misfit being the average over the 22 OMC and GLR observations. Furthermore, $\sigma(i)$ given by:

$$\sigma(i)^2 = \begin{cases} \sigma_{\text{age}}(i)^2 + 500^2 & \text{if } \text{Age}_{\text{mod}}(\text{OMC}) < \text{Age}_{\text{obs}}(\text{OMC}), \\ \sigma_{\text{age}}(i)^2 + 500^2 + 500^2 & \text{if } \text{Age}_{\text{mod}}(\text{OMC}) > \text{Age}_{\text{obs}}(\text{OMC}), \\ \sigma_{\text{age}}(i)^2 + 250^2 & \text{if } \text{Age}(\text{GLR}). \end{cases}$$

Here, $\sigma_{\text{age}}(i)$ reflects the observational uncertainty, given in the dataset, which is supplemented by an extra uncertainty allowing for structural error and bathymetric uncertainty (Briggs and Tarasov, 2013). The GLR-observations provide a two-way constraint, while the OMC-observations only provide a one-way constraint (i.e. a minimum age of OMC). This leads to two different values for the uncertainty, as there is less certainty about the age of OMC when the modelled age is older than the observed age.

For the ice thickness, the misfit scores are calculated using:

$$\text{Misfit}_{\text{ELEV}}(i) = \frac{(\text{Thk}_{\text{mod}}(i) - \text{Thk}_{\text{obs}}(i))^2}{\delta h(i)^2} + \frac{(\text{Age}_{\text{mod}}(i) - \text{Age}_{\text{obs}}(i))^2}{\sigma_{\text{age}}(i)^2}. \quad (5.9)$$

Here, $\delta h(i) = \sqrt{\sigma_{\text{thk}}(i)^2 + \min[100, \epsilon(i)]^2}$, with ϵ a downscaling uncertainty (ranging from 0 to 450 m) associated with the difference between the ice thickness in the original ALBMAP-dataset at 5 km resolution and the interpolated ALBMAP₂₀-dataset. The misfit for every observation point is taken at its minimal value, regarding modelled age and ice thickness, at that location over 21 kyr. To calculate the total ice thickness misfit for every simulation, a weighted sum is taken over all observations, where the weights account for the differences in data density between different regions, see Briggs and Tarasov (2013). In this way, a region containing many data points does not dominate the misfit.

The PD misfit is a weighted sum of the three aforementioned misfits. Firstly, the squared error of the ice-shelf surface is calculated for the three major ice shelves (RIS, FRIS and AmIS). The squared error is then normalised over the ensemble to give a misfit per ice shelf. The average of these three misfit scores is the ice-shelf misfit score. Secondly, the mean squared error of the ice thickness is calculated for the EAIS, the grounded part of the WAIS and the floating part of the WAIS. This is done using the grounded/floating mask of the simulation under consideration. The mean squared errors are then normalised over the ensemble to give a misfit score per part of the ice sheet. Thirdly, the squared error is calculated for the position of the eastern grounding line of the RIS at 81 °S. Normalising these squared errors over the ensemble leads to the last misfit score for the PD. The total PD misfit is calculated as a weighted sum of the individual parts, where the weights are 1/3 for the surface of the ice shelves, 1 for the ice thickness of each part of the ice sheet and 1/3 for the grounding-line position.

The total misfit for the entire simulation is equal to the weighted sum of the misfit scores for the past ice extent, the past ice thickness and the PD:

$$\text{Misfit} = (0.2 \cdot \text{Misfit}_{\text{EXT}} + 0.44 \cdot \text{Misfit}_{\text{ELEV}} + 0.45 \cdot \text{Misfit}_{\text{PD}})/1.09. \quad (5.10)$$

The weights are taken from Briggs and Tarasov (2013), leaving out the misfit score for relative sea-level rise.

5.2.3 Climate and sea-level forcing until 2100

The 16 standard simulations from the LGM to the PD have been continued until 2100 with the temperature and sea-level forcing following the four RCP-scenarios from the IPCC (Collins et al, 2014) and with the forcing kept constant at its pre-industrial level in 1850, which makes a total of 80 simulations. More specifically, the temperature and sea level follow a reconstruction record from 21 kyr ago until

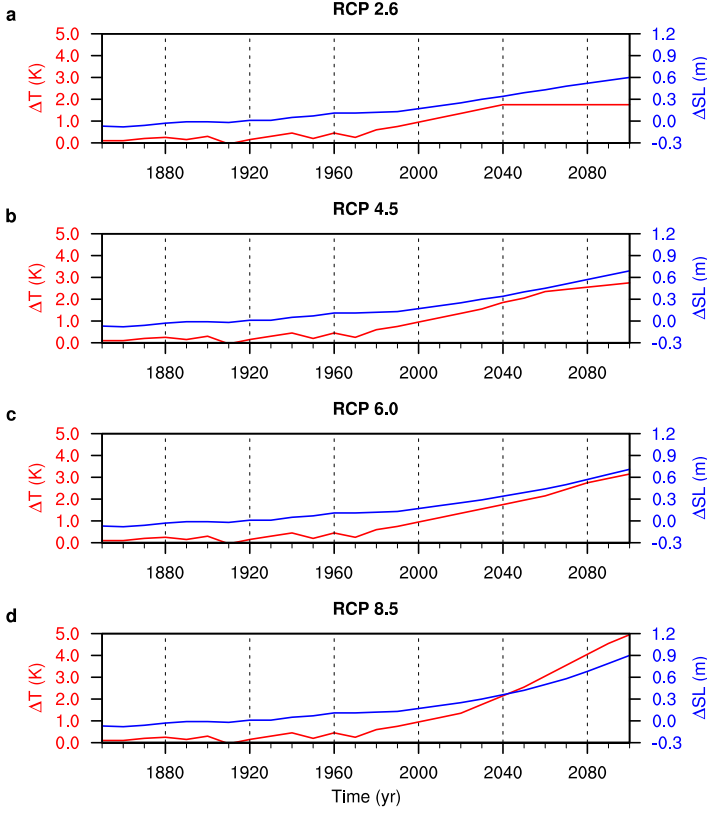


Figure 5.4: Temperature (in red) and sea-level (in blue) anomalies, w.r.t. the year 1850, until 2100 for the four RCP scenarios (Collins et al, 2014).

1850, after which the anomalies w.r.t. 1850, according to an RCP scenario, are added to the value at 1850 to get temperature and sea-level values until 2100. Keeping the forcing at the pre-industrial level means that the anomalies are zero until 2100. Between 2000 (0 kyr ago) and 2100, Equations 5.1 and 5.3 become:

$$T(t) = T(\text{PD}) + f_T \cdot \Delta T, \quad (5.11)$$

$$\text{SMB}(t) = \text{SMB}(\text{PD}) + f_{\text{SMB}} \cdot \Delta T. \quad (5.12)$$

This leads to an increase in SMB with temperature of $f_{\text{SMB}}/\text{SMB}_{\text{mean}}(\text{PD}) * 100\% = 5$ to 6% per $^{\circ}\text{C}$, equivalent to the estimates in Church et al (2014).

The temperature and sea-level forcing for the four RCP scenarios are shown in Figure 5.4. Sea level rises almost linearly for all scenarios, but shows a faster rise as the RCP number increases. The temperature rises until 2040 for RCP 2.6 and then becomes constant. For RCP 4.5, it rises somewhat faster until 2060 and then levels off. For RCP 6.0 and 8.5 the temperature keeps on rising steadily until 2100.

5.3 Results

We use coded names for the simulations in this chapter, consisting of three letters and optionally a fourth and a fifth symbol with the following meanings:

- First letter: I = ICE-5G topography or A = ANICE topography, to indicate which RACMO2/ANT-output was used to force ANICE.
- Second letter: E = EDC, F = Fuji, V = Vostok or W = WDC, to indicate the temperature reconstruction that was used, or 0 to indicate that a constant LGM temperature was used throughout the simulation.
- Third letter: B = Bintanja and van de Wal (2008) or S = SPECMAP, to indicate which sea-level reconstruction was used, or 0 to indicate that a constant LGM sea level was used throughout the simulation.
- Fourth and fifth symbol for the simulations until 2100: p = temperature and sea level were kept constant at pre-industrial levels, 26 = RCP scenario 2.6, 45 = RCP scenario 4.5, 60 = RCP scenario 6.0 or 85 = RCP scenario 8.5.

5.3.1 From the LGM to the PD

Figure 5.5 shows the grounded ice volume of the EAIS (upper lines) and the WAIS (lower lines) for all 19 simulations from 21 kyr ago until the PD. The ice volume is approximately the same for the simulations with different temperature reconstructions. Only the WDC temperature reconstruction makes the ice sheet retreat slightly later due to the temperatures being lower than in the other reconstructions during the deglaciation (from 15 to 6 kyr ago approximately). The SPECMAP record gives a lower sea level than with the sea-level record by Bintanja and van de Wal (2008), also leading to a late maximum of the ice volume, and hence a late retreat, for especially the EAIS in the SPECMAP simulations. The combination of the WDC and SPECMAP records in the IWS and AWS simulations therefore leads to the latest ice-volume maximum and latest retreat in the ensemble.

When using the RACMO2/ANT-output with the ICE-5G topography instead of the ANICE topography, the grounded ice volume is smaller during the entire simulation, especially the maximum is lower. This is because of the lower SMB from RACMO2/ANT using the ICE-5G topography. All simulations show a minimum ice volume for the EAIS in the mid-Holocene, which is consistent with observations (e.g. Hall, 2009; Ackert Jr. et al, 2013). These studies show re-advances of the grounding line around the mid-Holocene along the major ice shelves and on the Antarctic Peninsula. In ANICE the grounding line re-advances slightly on the eastern and western side of the FRIS and on the western side of the RIS. The grounding-line re-advance on the Antarctic Peninsula was not modelled, probably due to the coarse resolution of the model. This mid-Holocene re-advance and, at other locations, stagnation of the grounding line leads to less discharge over the grounding line while

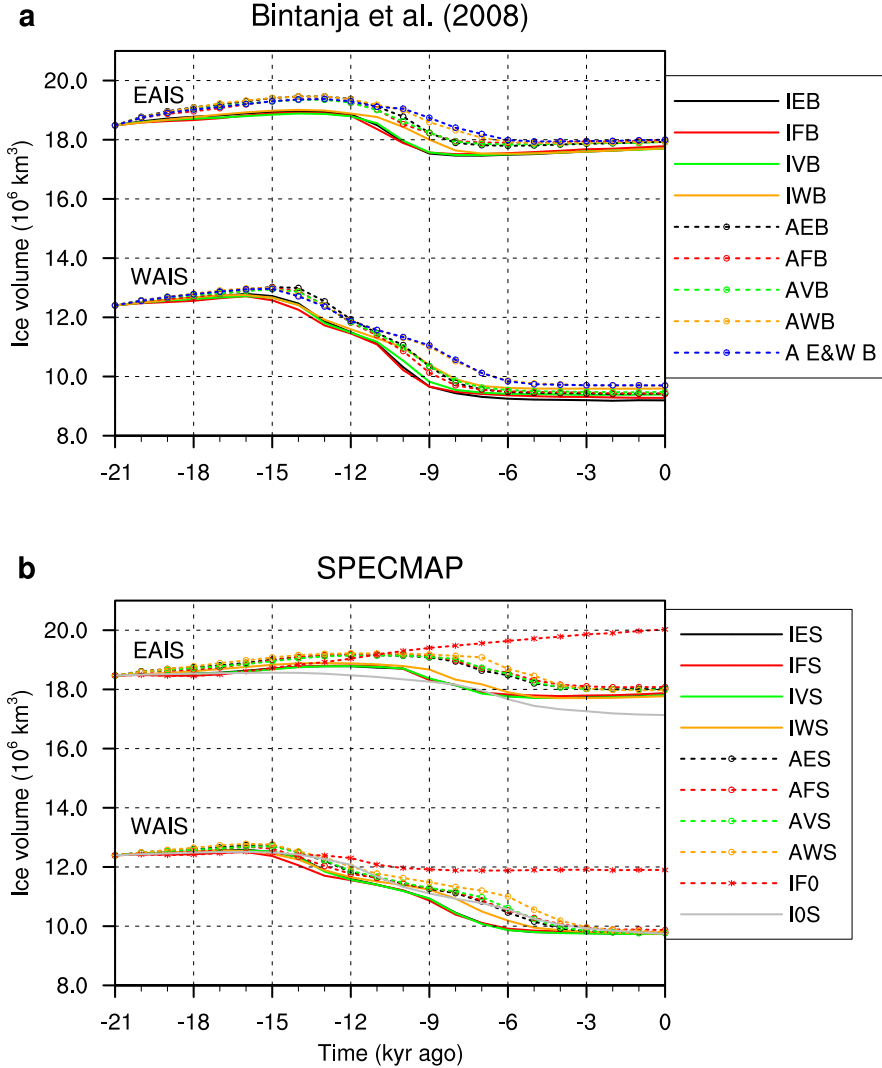


Figure 5.5: Grounded ice volume from 21 kyr ago until the PD for a) the eight simulations with the sea-level record from Bintanja and van de Wal (2008) and the extra simulation using the EDC temperature reconstruction for the EAIS and the WDC temperature reconstruction for the WAIS and b) the eight simulations with the SPECMAP sea-level record and the two extra simulations with a constant LGM sea level and a constant LGM temperature respectively. The colours indicate the used temperature reconstructions, while the dash patterns indicate the topography used to create the RACMO2/ANT climate.

the SMB increases due to increasing temperature. Together, these effects cause an increase in the ice volume of the EAIS (and the AIS as a whole) until the PD, leading to a background signal of increasing ice volume when simulating the future of the

ice sheet (see Section 5.3.3). The volume change between the maximum ice volume around 15 kyr ago and the PD ranges from 3.5 to $5.2 \cdot 10^6$ km³, equivalent to approximately 8.4 to 12.5 m s.l.e. (sea-level equivalent). This is on the high side of values found in recent literature (8.3 m from Gollledge et al (2013), 7 to 12 m from Gomez et al (2013) and 9 ± 1.5 m from Whitehouse et al (2012)), but significantly lower than older estimates, e.g., 14 to 24.5 m from Clark and Mix (2002).

To illustrate the effect of a changing temperature or sea level on the evolution of the AIS, we performed a simulation with a constant LGM temperature from the Fuji ice-core record and one with a constant LGM sea level from the SPECMAP sea-level record (I0S and IF0 in Figure 5.5b respectively). The IFS simulation has been selected as a reference because it is the simulation closest to the ensemble mean, regarding ice volume and comparison to observations (see Section 5.3.2). These two experiments are purely illustrative as the SMB and the surface-air temperature change from a pattern adapted to a glaciated state of the AIS to a pattern adapted to a deglaciated state and not with the evolving ice sheet. However, it can be concluded that the change in sea level has a larger effect than the change in temperature, which is also found by e.g. Ingólfsson et al (1998); Ritz et al (2001) and Pollard and DeConto (2009). When the sea level is kept constant at its LGM value, the EAIS does not retreat but grows further when temperatures rise due to an increase in the SMB. Only in the Ross Sea region of the WAIS, the ice sheet retreats a little with rising temperatures, due to increased basal melt and ice discharge. When keeping the temperature at the LGM value, the SMB remains small, which causes the EAIS to retreat even further than in the other simulations. The WAIS is more sensitive to air temperature through basal melt and ice discharge (De Boer et al, 2013) and therefore retreats less far than in most other simulations.

Figure 5.5a also shows a simulation with the RACMO2/ANT output over the ANICE topography, the sea-level record from Bintanja and van de Wal (2008), and the temperature reconstructions of both the EDC and the WDC ice cores (ANICE E&W Bintanja). In this simulation, the EDC reconstruction is used for the EAIS and the WDC reconstruction is used for the WAIS. The WAIS ice volume follows the ice volume from the AWB simulation, as expected. However, the EAIS ice volume also mainly follows the AWB simulation, but is slightly larger than both the AWB and the AEB ice volume at the PD. This is due to the fact that the WAIS is larger in the AWB simulation, which leads to less discharge from the EAIS. Additionally, the SMB is higher on the EAIS due to the slightly higher temperatures in the EDC reconstruction during the deglaciation.

5.3.2 Comparison to observations

The PD ice volume in ANICE is about $27 \cdot 10^6$ km³, which is somewhat higher than the observations (e.g. 58.3 m s.l.e., equivalent to about $24.5 \cdot 10^6$ km³, from Vaughan et al (2014) and $26.5 \cdot 10^6$ km³ from Fretwell et al (2013)). This overestimation is mostly due to too much ice on the Antarctic Peninsula and in the Amery basin,

Run	EXT	ELEV	Past	Ice shelves	EAIS	WAIS gr	WAIS fl	Ross gl	PD	Total
IEB	3062	321	960	9.8	39	5.8	13	3.55	16.8	582
IES	3062	319	960	8.4	40	8.2	12	0.01	17.1	582
IFB	3062	320	960	8.6	39	6.0	13	1.59	16.8	582
IFS	3063	319	960	7.4	40	8.4	12	0.01	17.3	582
IVB	3063	321	961	8.4	38	6.5	13	1.59	16.6	582
IVS	3063	316	960	8.3	40	8.2	12	0.01	17.1	582
IWB	3062	316	959	7.9	39	7.5	11	0.28	16.2	581
IWS	3063	314	959	7.8	40	8.3	10	0.01	16.6	581
AEB	3064	314	959	8.9	40	6.4	13	1.59	17.0	581
AES	3062	321	960	7.8	41	8.3	11	0.01	17.2	582
AFB	3063	324	961	8.8	40	6.5	13	1.59	17.1	583
AFS	3062	319	960	8.0	42	8.9	12	0.14	18.0	583
AVB	3063	322	961	8.3	40	6.8	13	1.59	17.0	582
AVS	3063	319	960	7.6	41	8.3	11	0.01	17.2	582
AWB	3063	319	960	8.2	40	7.8	11	0.07	16.7	582
AWS	3066	323	962	8.1	41	8.7	11	0.14	17.1	583

Table 5.2: Misfit scores per simulation (for the meaning of the abbreviations see Section 5.3). EXT is ice extent (OMC and GLR) and ELEV is ice thickness. Together they make up the misfit for the past (21 kyr ago until 500 yr ago, as the youngest data point is 500 yr old). The Ross, FRIS and Amery Ice Shelf misfits contribute to the misfit of the ice shelf surface at the PD, and the EAIS, WAIS gr and WAIS fl misfits represent the misfits in ice thickness of the EAIS, of the grounded part of the WAIS and the floating part of the WAIS respectively. The Ross grounding-line misfit at 81°S is shown under 'Ross gl'. The misfits from the 5th to the 11th column make up the PD misfit, which combines with the past misfit to produce a total misfit per simulation.

probably because of an insufficient horizontal model resolution to capture the detailed topography in these regions. Besides considering the PD volume of the ice sheet, the results of the simulations are compared to observations here, as described in Section 5.2.2.

The misfit scores for the 16 LGM-PD simulations are shown in Table 5.2. The first column shows the misfit scores for the past ice extent of each simulation. These numbers are high because most of the observed GLR events are not modelled within the 21 kyr period, as will be discussed later. The ICE-5G-topography simulations perform slightly better for the past (both the ice extent and the ice thickness), especially in the Amery region and the Ross Sea area, than the ANICE-topography simulations.

The fourth column of Table 5.2 shows the misfit in the PD ice shelf surface. The surface of the ice shelves is better modelled in the SPECMAP simulations, mostly due to a better match between the modelled and the observed RIS surface. The RIS surface is modelled with an average error of +10% (overestimated), while the AmIS surface has an error of around -20% (underestimated) and the FRIS surface has an error of about +60%. The average PD ice thickness is well modelled for the EAIS,

lat (°S)	lon (°E)	age (kyr ago)	distance to GL (km)	lat (°S)	lon (°E)	age (kyr ago)	distance to GL (km)
67	63	11.7	95	74	232	14.7	15
67	66	14.2	101	73	254	17.2	62
68	74	11.8	158	68	289	14.1	40
66	141	15.6	103	66	291	13.2	85
66	143	17.2	51	65	292	18.7	78
70	168	13.8	44	64	294	16.6	65
71	170	17.4	53	63	297	17.5	74
75	167	14.8	3	63	302	17.5	34
74	174	13.0	139	64	305	18.3	25
76	181	16.8	94				

Table 5.3: Latitude (*lat*) and longitude (*lon*) of the observed GLR ages (*age*), with the distance to the grounding line (GL) for the IFS simulation at that age.

but less so for the WAIS, compared to ALBMAP₂₀. The ensemble mean ice-thickness error is about +5% for the EAIS, +50% for the grounded part of the WAIS and -10% for the floating part of the WAIS. The misfit over the grounded part of the WAIS is largely due to the mismatch between modelled and observed ice thickness on the Antarctic Peninsula. The simulations with the sea-level reconstruction from Bintanja and van de Wal (2008) do better at simulating the ice thickness of the grounded part of the ice sheet, but the simulations with the SPECMAP sea-level reconstruction do better at simulating the floating part of the WAIS. Therefore, the position of the Ross grounding line, which is close to its observed position in every simulation (7 to 135 km difference between the observed and the modelled position), is also better modelled in the simulations using the SPECMAP sea-level reconstruction.

The grounded part of the ice AIS is better simulated with the sea-level reconstruction from Bintanja and van de Wal (2008), whereas the floating part of the AIS is better simulated with the SPECMAP record. This is probably due to the fact that the sea level from Bintanja and van de Wal (2008) causes an earlier retreat of the ice sheet than the SPECMAP sea-level record (see Section 5.3.1). As the ice thickness is overestimated for the grounded part of the ice sheet an earlier retreat would lead to a better fit. Additionally, the ice shelves retreat slightly too early and too far inland, so a later retreat would match the observations better. Overall, the simulations perform very similar, but the ICE-5G simulations perform slightly better than the ANICE simulations. We ascribe this to the fact that the model was tuned for the climate produced with the ICE-5G topography (see Chapter 4). However, there are large performance differences between different regions.

Figure 5.6a shows the performance of the IFS run in simulating grounding-line retreat and the onset of open marine conditions. This figure looks very similar for the other simulations. OMC is well modelled, at the observed age two of the three locations are modelled to be open ocean. At one location open ocean was modelled

around 2000 years later than was observed. Similar results were obtained by the other simulations. There are 19 observations of GLR, whereas only one is captured by ANICE. The GLR that has been captured by the model took place on the western side of the RIS embayment, see Figure 5.3. Other observed GLR events have not been modelled, mostly due to the fact that the ANICE grounding line did not extend far enough during the LGM. However, the distance between the modelled grounding line and the location of the GLR observation at the observed age is not very large, as is shown in Table 5.3. This shows that model resolution might also play a role here.

A comparison between modelled and observed ice thickness in the past is presented in Figure 5.6b. The figure is based on 92 observations, but only the 24 regional averages are shown for clarity. The bullets represent the regional average of the misfit of the model results, and show that past ice thickness is well modelled on the WAIS and on the East-Antarctic coast, whereas in the Amery region and the Antarctic Peninsula the errors are large.

5.3.3 From 2000 to 2100

ANICE has been run until 2100, using temperature and sea-level forcing from the IPCC AR5 (Collins et al, 2014; Church et al, 2014). Figure 5.7 shows the ensemble means of these simulations (solid lines) with respect to the 1986-2005 mean volume, with an envelope representing one standard deviation, for the four IPCC-scenarios and for a constant forcing from 1850 until 2100. For some time after 2000 the EAIS (and therefore the entire ice sheet) is still slowly growing as from the mid-Holocene (see Figure 5.5), but around 2030 sea-level rise and positive temperature forcing start to dominate for RCP scenarios 4.5, 6.0 and 8.5. However, for RCP 2.6 the ice sheet does not retreat and even grows larger due to a larger increase in SMB than in ice discharge.

The final change in volume by 2100 with respect to 2000 depends strongly on the history of the ice sheet, indicated by the large standard deviation. For instance, the simulations with the most negative sea-level contribution by 2100 (indicating a growing ice sheet) are the simulations with ICE-5G and Bintanja forcing. The ice volume for these simulations still grows relatively fast at the PD in Figure 5.5a. The simulations with the most positive sea-level contribution (indicating a retreating ice sheet) are the simulations with ANICE and SPECMAP forcing which show a constant ice volume at the PD in Figure 5.5b.

To separate the rising temperature effect from the effect of sea-level rise, two other simulations have been carried out. In one simulation the temperature is kept constant at the pre-industrial (1850) level and in one simulation the sea level is kept constant since 1850. These experiments have been done with the IFS run as a basis from the LGM until 1850. Results for the sea-level contribution from 2000 to 2100 are shown in Figure 5.8. The solid red line indicates the standard IFS85 run and the solid green and grey lines indicate the experiments where the sea level and the temperature are kept constant, respectively. When sea level is kept constant, the

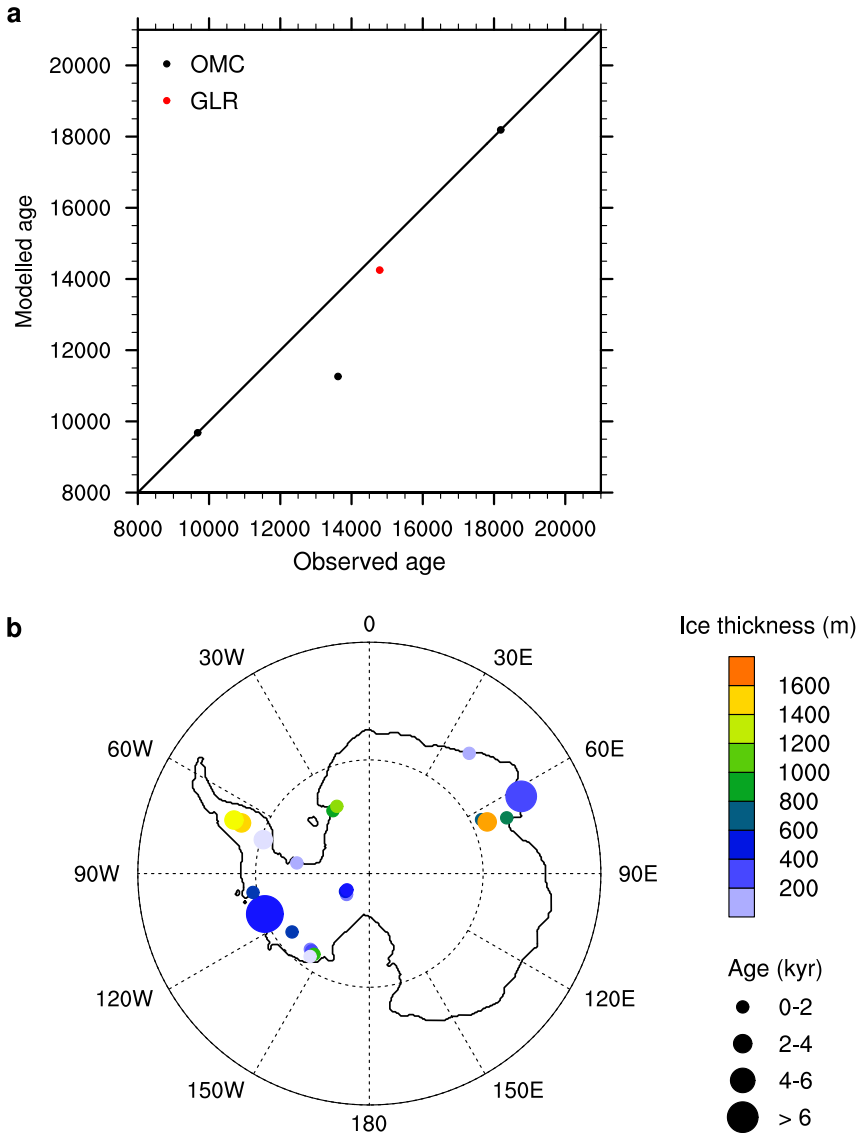


Figure 5.6: *a)* Modelled versus observed age of onset of marine open conditions (in black) and grounding-line retreat (in red) of the IFS-run. If the model did not produce grounding-line retreat during the modelled 21 kyr where it should have occurred, the data point is not shown. *b)* Map of Antarctica showing the IFS PD grounding line in black and the ice thickness and age misfit with respect to observations for the IFS-run, averaged per region. The size of the bullet shows the modelled age error and the colour indicates the modelled thickness error.

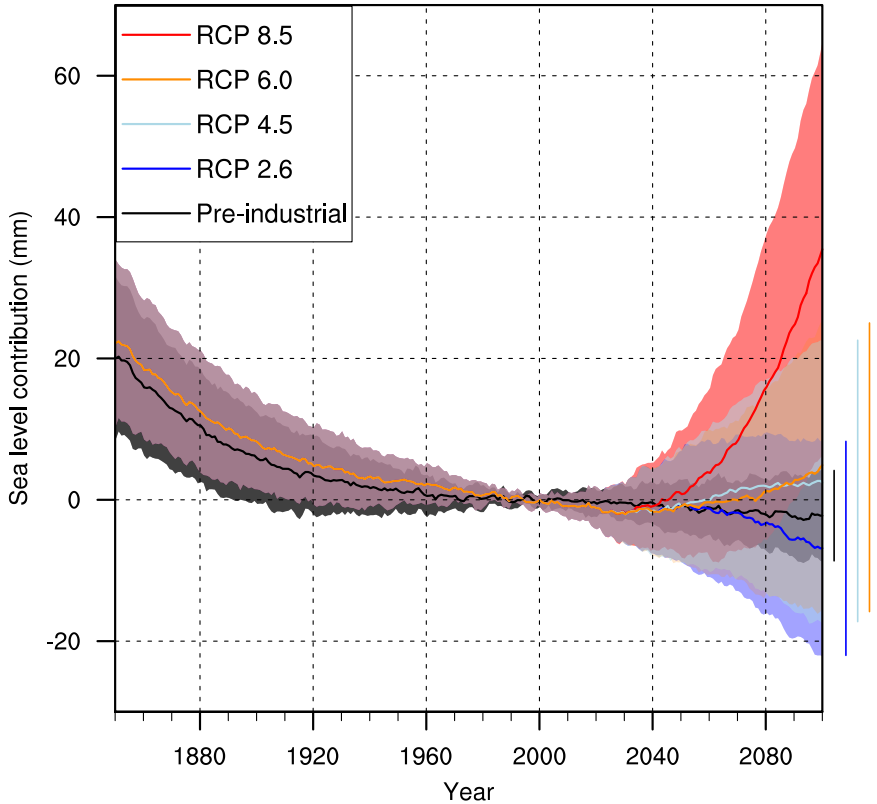


Figure 5.7: Grounded ice volume in mm s.l.e. from 1850 until 2100, with respect to the mean grounded ice volume over 1850-1900. The mean of the ensemble is shown in solid lines with an envelope indicating one standard deviation for each of the RCP scenarios and the pre-industrial climate forcing. The spread in 2100 is also indicated per scenario by the vertical lines to the right of the figure.

AIS grounded ice volume grows larger than for the standard IFS85 run, due to less ice discharge and less retreat of the grounding line. When the temperature is kept constant the SMB remains the same as well, i.e. does not increase. Additionally, the ice at the base is less warm than for the standard run, which especially affects the ice shelves and leads to smaller sliding velocities and hence to less discharge. The effect is a larger ice sheet for this simulation. Furthermore, this experiment makes clear that sea-level rise has now been replaced by temperature as the dominant factor in the evolution of the grounded ice volume (with respect to the period from the LGM to the PD). This is mostly due to the fact that sea level changes very little from 1850 to 2100 (less than 1 m as opposed to more than 100 m over the past 21 kyr), while temperature changes are relatively large (2 to 5°C as opposed to 8 to 10°C over the past 21 kyr).

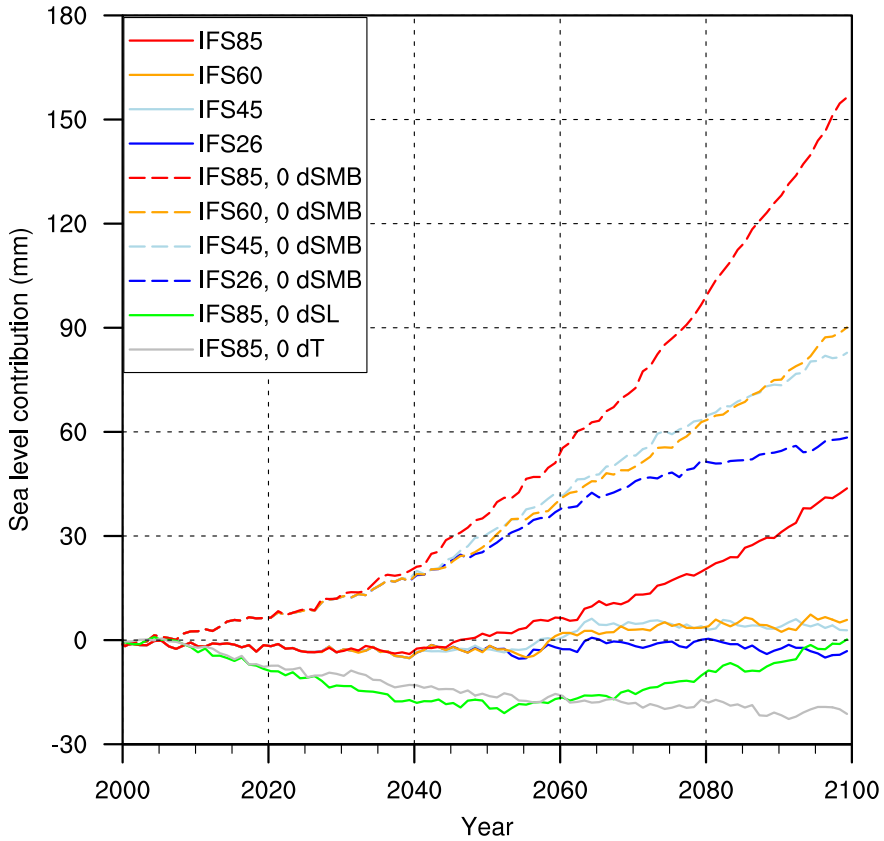


Figure 5.8: Grounded ice volume in mm s.l.e. from 2000 until 2100, with respect to the 1986–2005 mean grounded ice volume. The four RCP-scenario simulations are shown for the standard IFS simulation and a simulation where the SMB was not allowed to change after the year 2000 (0 dSMB). The green line indicates a simulation deduced from the IFS85-simulation, but the sea level was not allowed to change after the year 1850 (0 dSL). For the grey line (0 dT) the temperature was not allowed to change after 1850.

According to Church et al (2014), the sea-level contribution from the AIS in 2100, w.r.t. 2000 will be between -20 and 185 mm. This range is predominantly based on Little et al (2013). However, in their study they did not allow the SMB to change, while e.g. Ligtenberg et al (2013) concluded that the SMB increases significantly in the coming century ($0.27 \text{ mm s.l.e. K}^{-1} \text{ yr}^{-1}$, equivalent to approximately 27 to 54 mm, from 2000 to 2100). Figure 5.8 shows the sea-level contribution for the four RCP-scenarios for the IFS simulation (Standard IFS, solid lines) and for the same simulations without changing the SMB from the year 2000 onwards (0 dSMB, dashed lines). Keeping the SMB constant clearly introduces a positive bias to the sea-level contribution (of about 60 to 120 mm s.l.e. according to our study) due to the fact

that the SMB increases with increasing temperatures. Our estimate of the AIS sea-level contribution by 2100, with respect to 2000, lies in the range of -22 to 8 mm for RCP 2.6, -17 to 23 mm for RCP 4.5, -16 to 25 mm for RCP 6.0 and 6 to 63 mm for RCP 8.5. This still falls within the range of -20 to 185 mm, given by Little et al (2013), but is slightly lower because we include changes in the SMB. Also, our RCP 8.5 range of 6 to 63 mm falls within the range found by Bindschadler et al (2013) of 0 to 144 mm (for their R8 simulation, which is close to the RCP 8.5 scenario), who did an ensemble study with different ice-dynamical models.

Another important process in the future evolution of the AIS is the basal melt of ice shelves (Rignot et al, 2013). In Figure 5.9 the basal melt is shown at the PD. On the eastern side of the RIS the basal melt is overestimated compared to Rignot et al (2013), but it is underestimated on the western side. The basal melt under the FRIS shows roughly the same pattern with more melt in the middle and less melt and even freezing of the southern and northern parts of the ice shelf. The AmIS shows large melt rates, which are also found in Rignot et al (2013). However, we do not find the high melt and freezing rates that are observed close to the coasts (especially the coast of the Amundsen Sea. This is probably due to the low resolution of the model and the simplistic calving scheme. Basal melt rates underneath the RIS have also been studied by Dinniman et al (2011) with a model, which suggests melt rates around zero for most of the ice shelf and rather high melt rates near the calving line. Our results are in accordance with these findings except for the high basal melt rate near the calving line, although it is generally accepted that most of the basal melt takes place near the grounding line and close to the calving line freezing occurs with moderate basal melt rates in between (Jenkins and Doake, 1991). Additionally, an average basal melt rate of 0.20 ± 0.06 m/yr for the FRIS is mentioned in Nicholls et al (2009), which suggests a slight underestimation of the basal melt in ANICE. As most of the smaller ice shelves are not captured by ANICE, we underestimate the total basal melt rate quite severely. For the IFS simulation we model a BMB of 80 Gt/yr in the year 2000, as opposed to the estimate of 1325 Gt/yr by Rignot et al (2013). In the year 2100, the BMB has increased to 380 Gt/yr for the IFS85 simulation, with melt rates around 0.5 m/yr for the FRIS. This is much less than the melt rates of 4 m/yr as predicted by Hellmer et al (2012), although they say that the timing of these high melt rates of the FRIS is uncertain and might also arise after 2100. The BMB of the floating part of the ice sheet and the other parts of the mass balance are shown in Figure 5.10.

Grounding line motion determines the rapid changes in grounded ice volume in ANICE, which is probably mostly an artefact of the coarse resolution of the model. Because of the 20x20 km resolution, every grid point contributes about 1 to 4 km³/yr (assuming an ice thickness of 250 to 1000 m at the grounding line), so the grounding of a few grid points already leads to a visible increase in the grounded ice volume. Ice discharge and SMB balance each other as the dominant components of the mass balance, whereas the BMB of the grounded part of the ice sheet is very small (about

-20 km³/yr). Furthermore, the ice discharge over the grounding line is shown for the IFS85 simulation where the SMB is not varied after 2000 (the 0 dSMB simulation in Figure 5.8). As Winkelmann et al (2012) predicts as well, the ice discharge is smaller for this simulation. According to our study, the extra discharge due to an increase in SMB during the 21st century following the RCP 8.5 scenario is about 0.04 mm s.l.e. per year, very comparable to the results by Winkelmann et al (2012).

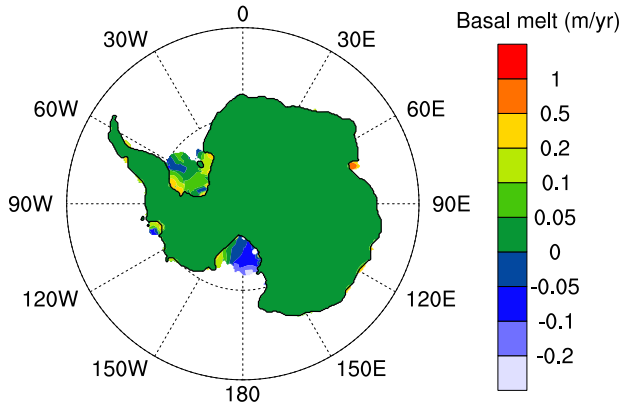


Figure 5.9: Basal melt at the PD for the IFS85 simulation.

5.4 Conclusions

We carried out 16 simulations of the AIS from the LGM to the PD using different temperature and sea-level reconstructions. We found no significant difference in the influence of the four temperature records on the evolution of the ice sheet. Only using the WDC ice core record causes the ice sheet to retreat later than for the other temperature records because the slope of the increase in temperature from 18 to 12 kyr ago is less steep and therefore the temperature is somewhat lower in these simulations than in the others during the deglaciation. This difference is also seen between two sea-level records. The sea level from the SPECMAP record rises more slowly and therefore the ice sheet retreats later than for the simulations with a sea-level record from Bintanja and van de Wal (2008). The simulations with a forcing based on the ICE-5G topography have a smaller AIS volume than for the simulations with a forcing based on the ANICE topography. This is due to the fact that the AIS is higher in the ICE-5G topography and therefore the temperatures and the SMB are lower. Furthermore, two simulations have been carried out with either the temperature or the sea level kept constant at their LGM level. These experiments show that sea-level rise is the primary cause of the deglaciation of the AIS, and here the grounded ice volume difference between its maximum value (around 15 kyr ago) and its PD value ranges from 8.4 to 12.5 m s.l.e., which is on the high side of other

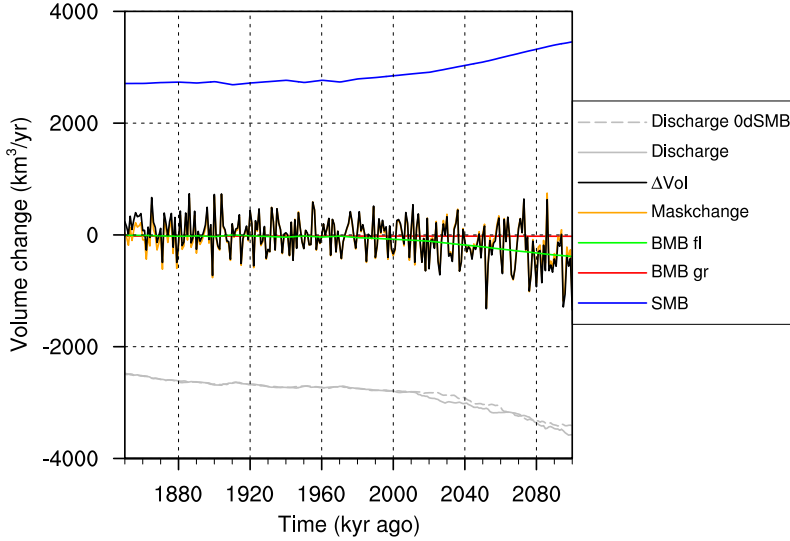


Figure 5.10: Mass balance components of the grounded part of the AIS from 1850 until 2100 for the IFS85 simulation: Basal mass balance (of the grounded part, BMB gr), surface mass balance (SMB), ice discharge over the grounding line, grounding-line (GL) motion and the resulting change in volume. Additionally, the BMB of the floating part of the ice sheet (BMB fl) is shown and the discharge over the grounding line if the SMB is kept constant after the year 2000 (Discharge 0dSMB).

values found in recent literature (Golledge et al, 2013; Gomez et al, 2013; Whitehouse et al, 2012).

The results of these 16 simulations have been compared to observations of past ice extent, ice thickness and the PD state of the AIS. From this comparison we conclude that especially the RIS and Amundsen Sea areas are well modelled, but the FRIS, Antarctic Peninsula and Amery regions are less well modelled in both the past and the present. The EAIS and the floating part of the WAIS are significantly better modelled than the grounded part of the WAIS, due to the quite severe overestimation of the ice thickness on the Antarctic Peninsula. The floating ice thickness of the WAIS is mainly overestimated due to the FRIS extending too far into the ocean. Similar results are found by Whitehouse et al (2012), although their misfits are generally smaller than ours. This is due to the fact that they used observations as constraints for their ice-sheet model which is run to a steady state for five time slices (20, 15, 10 and 5 kyr ago and the PD), whereas ANICE simulates a continuous evolution of the ice sheet without using observations as constraints. They discuss some model limitations, which are also mentioned by Bindshadler et al (2013), and are applicable to ANICE as well: (1) inadequate understanding of all physical processes and incomplete model physics resulting in poor representation of all the processes, (2) the use of a 20 km grid, which is too coarse to capture complex topography and small-scale,

fast-flowing outlet glaciers, (3) uncertain climate and sea-level reconstructions and coupling between the ice-sheet model and its surrounding atmosphere and ocean. Despite these limitations, we have confidence in determining the key processes that played a role during the deglaciation of the AIS and that will play a role in the future.

The 16 simulations have been continued until the year 2100 using the four RCP-scenarios from the IPCC AR5 and using a constant pre-industrial forcing from 1850 until 2100. The volume of the AIS continues to increase until about 2030 because of the EAIS that is still growing from a minimum in the mid-Holocene and due to rising temperatures leading to an increase in SMB. However, after 2030 the increase in discharge starts to dominate for the RCP 4.5, 6.0 and 8.5 scenarios and the AIS starts retreating. The history of the ice sheet is very important for its evolution between 2000 and 2100, and therefore for its sea-level contribution. It makes the difference between a negative and a positive sea-level contribution by 2100. We find a sea-level contribution by 2100, with respect to 2000 in the range of -22 to 63 mm, depending on the scenario and the history of the ice sheet. These results compare well to the ranges given by Little et al (2013) and Bindschadler et al (2013).

Bindschadler et al (2013) also discusses some limitations of dynamical ice-sheet models that still need to be overcome to be able to adequately predict the future of ice sheets. These limitations are applicable to this study as well, nevertheless we conclude that both the SMB and the discharge of the ice sheet are dominant, counteracting components and therefore very important to get right. Furthermore, the background signal of the ice volume, caused by its history, is a component that can not be ignored and motivates using ice-dynamical models to predict the future of the AIS.

Acknowledgements

The figures in this chapter were produced with NCL (UCAR/NCAR/CISL/VETS, 2013). We thank SURFsara (www.surfsara.nl) for the support in using the Cartesius Compute Cluster. We also appreciate the suggestions and comments by two anonymous reviewers, which led us to improvements of the manuscript.

Conclusions and outlook

This thesis discusses the evolution of the AIS from the LGM to 2100, as modelled with the ice-dynamical model ANICE. In the first two chapters a general introduction and a discussion of the model have been given. In the third chapter, temperature and precipitation output from different GCMs have been compared to observations for the Antarctic region in order to find the GCM that best represents past and present climate for this region. One of the best performing GCMs was HadCM3, of which the output was then used in RACMO2/ANT to simulate an LGM climatology (temperature and SMB) to force ANICE with. This forcing was used in Chapter 4 in sensitivity experiments with ANICE from 120 kyr ago until the PD. These experiments led to optimal values for certain important model parameters and produced an initial ice sheet to start simulations from 20 kyr ago until the PD, the focus of this thesis. An ensemble study from the LGM until 2100 showed that the deglaciation is still important in the current evolution of the ice sheet, but that human-induced climate change is quickly taking an equally important role. In this chapter these main conclusions are presented in more detail. Furthermore, some limitations in ANICE and other ice-dynamical models are described, including possible ways to overcome these limitations.

6.1 Conclusions

6.1.1 The GCM intercomparison

The ice-dynamical model ANICE, as described in Chapter 2, has been applied to the AIS over the past 120 kyr, with a focus on the past 21 kyr. To force the model the

regional atmospheric climate model RACMO2/ANT has been used, which needs input from re-analysis data or a GCM at its lateral boundaries. Therefore, Era-interim data were used to force RACMO2/ANT for the PD and for 120 kyr ago, as the climatological conditions were approximately the same then. However, to simulate the LGM climate, a suitable GCM had to be found.

In Chapter 3 the output for the Antarctic region of 18 different GCMs has been compared to ice-core data for the past and to a reference state from RACMO2/ANT for the present. GCM output was available for the PD (all 18 GCMs), the mid-Holocene at 6 kyr ago (14 GCMs) and the LGM at 21 kyr ago (9 GCMs). However, as the differences in temperature and precipitation between the mid-Holocene and the present are small in ice-core reconstructions and in the output from the GCMs, the biases of the GCMs are of the same order of magnitude as these differences or even larger. Additionally, the uncertainties in ice-core data are approximately as large as the signal for this period. Therefore, it is hard to judge individual model performances for the mid-Holocene and the results for this period were not taken into consideration for the final intercomparison.

For the PD, the air-temperature patterns are generally well simulated, and more correctly simulated over the ocean than over the ice sheet. The temperature over the ice shelves is too high in most of the models, which is probably due to the fact that there is land at the locations of the ice shelves in the GCMs, which is only partly covered with ice. Precipitation patterns are also well simulated in general, but the amount of precipitation is often underestimated over the ocean. In addition, a strong negative bias is observed over the western coast of the Antarctic Peninsula. The GCMs probably do not resolve the circulation pattern and the orography well enough to simulate the additional precipitation in this region (Rojas et al, 2009).

During the LGM, temperatures were lower and there was less precipitation than in the present-day climate, according to both ice-core reconstructions and GCM output. The temperature difference between the LGM and the present is modelled to be larger over the WAIS than over the EAIS by most GCMs. This is not in accordance with ice-core reconstructions, for which the LGM temperature from the WDC ice core is slightly higher than the LGM temperature from the EDC ice core, for instance (see Figure 5.2). The precipitation differences between the LGM and the present over the Antarctic Peninsula are generally modelled to be smaller than elsewhere, or even positive (wetter at the LGM than in the present).

There are two main sources of uncertainties in the comparison between the GCM results and the reference data (RACMO2/ANT-data for the PD and ice-core reconstructions for the past). The first source, important to the judgement of PD performance of the GCMs, is the uncertainty in RACMO2/ANT-data. This is negligibly small compared to the other uncertainties in this study (see Van de Berg, 2008; Lenaerts et al, 2012a). The second source is the uncertainty in the ice-core reconstructions; part of this is due to the uncertainty in the temperature and precipitation reconstruction and part is due to the uncertainty in the determination of the age of

the ice in the ice core.

Some GCMs simulate temperature and precipitation significantly better than others, in the past as well as at the PD. As GCMs are often used to provide ice-dynamical models with a climatological forcing and because this forcing is important for the evolution of the ice sheet, it is important to put some effort into finding the GCM best suited to the purpose of the study before using its output. The best suited GCMs for modelling the AIS from the LGM to the PD are HadCM3 and MIROC 3.2.2.

6.1.2 The sensitivity experiments with ANICE

To study the evolution of an ice sheet with an ice-dynamical model, the initial state of the ice sheet is important, as well as the climatological forcing. To find a good initial state and set-up of the model parameters a sensitivity study of ANICE has been done by running the model from 120 kyr ago until the PD while varying certain parameters (see Chapter 4). The climatological forcing for these simulations has been obtained by interpolating between three climate states (consisting of the air temperature and the SMB): 120 kyr ago, 21 kyr ago and the PD, where the PD climate has been used for 120 kyr ago as well. The LGM climate comes from RACMO2/ANT, with HadCM3 forcing at the lateral boundaries, while the PD climate comes from RACMO2/ANT with Era-interim forcing. The temperature and SMB patterns are interpolated linearly in time, whereas their amplitudes are interpolated following the EDC ice core (see Section 4.2.2 for a detailed explanation).

The parameters that have been investigated in the sensitivity study are the friction angle of the bed below sea level, the SSA and SIA enhancement factors and the flexural rigidity and the relaxation time of the bedrock. The effect of varying these parameters on the evolution of the AIS has been studied, but first a reference simulation was defined which gave satisfactory results for the LGM and the PD.

The effect of the amount of sliding on the ice sheet has been studied by changing two different parameters, the friction angle of the bed below sea level (ϕ_{min}) and the SSA enhancement factor (E_{SSA}). More sliding generally leads to less volume due to the ice flowing faster away from the ice sheet. Between the LGM and the PD the AIS loses mass until a minimum ice volume is reached around the mid-Holocene (5-6 kyr ago) after which the ice re-advances. The timing and the strength of this minimum is dependent on the amount of sliding, where less sliding leads to a less pronounced and later minimum. In other words, more sliding effectively reduces the response time of the ice sheet. These results are in good agreement with observations, which indicate that the onset of this re-advance was indeed timed in the mid-Holocene.

The effect of changing the SIA enhancement factor (E_{SIA}) is mostly seen on the EAIS, where the ice moves due to deformation. A larger value of E_{SIA} leads to less volume over the entire simulation period from 120 kyr ago until the present.

The effect of the changes in the flexural rigidity and the relaxation time of the bedrock are most pronounced on the WAIS where the largest changes in ice loading take place. A thinner lithosphere (modelled by a smaller flexural rigidity and relax-

ation time) leads to a higher PD ice volume due to a faster rebounding of the bed, causing shallower grounding-line depths and thus reducing the ice flux across the grounding line.

The maximum grounded ice volume for the entire AIS occurred between 15 and 16 kyr ago and lies between 30.5 and $32.4 \cdot 10^6 \text{ km}^3$, which is within the range of 27.3 to $34.6 \cdot 10^6 \text{ km}^3$ found in the literature (Clark and Mix, 2002; Briggs and Tarasov, 2013). The PD grounded ice volume is overestimated in the model by about 8%, which is probably mainly due to the fact that with a resolution of $20 \times 20 \text{ km}$ the details of the topography of the Antarctic Peninsula and the Amery Ice Shelf area cannot be modelled correctly. The difference between the modelled LGM and the PD grounded ice volume is $-4.3 \pm 0.5 \cdot 10^6 \text{ km}^3$, equivalent to $10.7 \pm 1.3 \text{ m s.l.e.}$, which is also within the range found in the literature (6.3 to 24.5 m s.l.e.)

6.1.3 Modelling the AIS from the LGM to 2100

In Chapter 4 it has been concluded that ANICE performs well, regarding the PD grounding line, grounding-line retreat and LGM grounded ice volume for the optimal set of parameters that were used to define the reference simulation. ANICE, with this optimal set of parameters, can then be applied to study the deglaciation of the AIS from LGM to PD in more detail, which has been done in Chapter 5.

I carried out 16 simulations of the AIS from the LGM to the PD using four different temperature reconstructions (from the EDC, Vostok, Fuji and WDC ice cores), two different sea-level reconstructions (from SPECMAP and Bintanja and van de Wal (2008)) and two different ice-sheet topographies to simulate the LGM climate in RACMO2/ANT (from Ice-5G and from the ANICE reference simulation of Chapter 4). No significant difference was found in the influence of the four temperature records on the evolution of the ice sheet. Only using the WDC ice-core record causes the ice sheet to retreat later than for the other temperature records because the slope of the increase in temperature from 18 to 12 kyr ago is less steep and therefore the temperature is somewhat lower in these simulations than in the others during the deglaciation. This difference is also seen between the two sea-level records. The sea level from the SPECMAP record rises more slowly and therefore the ice sheet retreats later than for the simulations with a sea-level record from Bintanja and van de Wal (2008). The simulations with a forcing based on the Ice-5G topography have a smaller AIS volume than for the simulations with a forcing based on the ANICE topography. This is due to the fact that the AIS is higher in the Ice-5G topography and therefore the temperatures and the SMB are lower. Furthermore, two simulations have been carried out with either the temperature or the sea level kept constant at their LGM level. These experiments show that sea-level rise is the primary cause of the deglaciation of the AIS.

The results of these 16 simulations have been compared to observations of past ice extent, ice thickness and the PD state of the AIS, following the method described by Briggs and Tarasov (2013). From this comparison it has been concluded that

especially the Ross Ice Shelf and Amundsen Sea areas are well modelled, but the Filchner-Ronne Ice Shelf, Antarctic Peninsula and Amery regions are less well modelled in both the past and the present. The EAIS and the floating part of the WAIS are significantly better modelled than the grounded part of the WAIS, due to the quite severe overestimation of the ice thickness on the Antarctic Peninsula.

The 16 simulations have been continued until the year 2100 using the four RCP-scenarios from the IPCC AR5 and using a constant pre-industrial forcing from 1850 until 2100, giving a total of 80 simulations. The volume of the AIS continues to increase until about 2030 because the EAIS is still growing from a minimum in the mid-Holocene and due to rising temperatures leading to an increase in the SMB. However, after 2030 the increase in discharge starts to dominate for the RCP 4.5, 6.0 and 8.5 scenarios and the AIS starts retreating. The history of the ice sheet is very important for its evolution between 2000 and 2100, and therefore for its sea-level contribution. It makes the difference between a negative and a positive sea-level contribution by 2100. By 2100, with respect to 2000, a sea-level contribution in the range of -22 to 63 mm was found, depending on the scenario and the history of the ice sheet. These results compare well to the ranges given by Little et al (2013) and Bindshadler et al (2013).

Qualitatively, it can be concluded from this study that the SMB and the discharge over the grounding line are the dominant, counteracting components of the grounded mass budget of the AIS. Therefore, these two components are important to model correctly. Furthermore, the history of the ice sheet is a component that can not be ignored and motivates using ice-dynamical models to investigate the future of the AIS.

6.2 Outlook

In the introduction it was stated that 'we want to know what part of the current changes on Antarctica are associated with the natural transition from a glacial into an interglacial period and what part is a consequence of human activities'. This question is hard to answer quantitatively, but the results from the research in this thesis indicate that the deglaciation still plays a role in the current changes on Antarctica (see Chapter 5). However, this natural signal is rapidly getting lost in the signal of global warming.

Although the role of different components in the past and the future of the evolution of the AIS can qualitatively be estimated, a quantitative assessment of the future of the ice sheet is still hampered by model limitations. Whitehouse et al (2012) discuss some of these limitations, which are also mentioned by Bindshadler et al (2013), and are applicable to ANICE as well: (1) inadequate understanding of all physical processes involved in modelling ice dynamics and incomplete model physics resulting in poor representation of these processes, (2) the use of a 20 km grid, which is too coarse to capture complex topography and small-scale,

fast-flowing outlet glaciers, (3) uncertain climate and sea-level reconstructions and coupling between the ice-sheet model and other models simulating the surrounding atmosphere and ocean.

Some of these issues have already been addressed in other studies. For instance, Gomez et al (2013) have coupled a 3-D ice-dynamical model with a model which solves the sea-level equation. Furthermore, Helsen et al (2012) have coupled ANICE asynchronously to RACMO2/GR with a 1000 year interval from the Eemian (128 kyr ago) until the PD to study the evolution of the Greenland Ice Sheet. For the future, coupling ANICE to a model that solves the sea-level equation, to RACMO2/ANT (asynchronously) and to a self-gravitating Earth model (e.g. De Boer et al, 2014b) could be considered. Coupling to a better Earth model is mentioned as well because it has been concluded in Chapter 4 that the movement of the bedrock plays an important role in the deglaciation of the AIS. Additionally, experiments with a higher resolution should be done to model the ice thickness more accurately on the Antarctic Peninsula and in the Amery Ice Shelf region.

To investigate the importance of the different physical processes in ice-sheet dynamics, some (large) ensemble studies have been carried out in which model results have been tuned to or compared to observations (e.g. Whitehouse et al, 2012; Briggs et al, 2013). Briggs and Tarasov (2013) describe a database and a method to compare model results to this database. It would be interesting to use this comparison method with several different ice-dynamical models in an ensemble study. In this way a more coherent view on important physical processes and model performance can be obtained, improving and reinforcing predictions of the future of the AIS by ice-dynamical models.

List of acronyms

ACC	Antarctic Circumpolar Current
AIS	Antarctic Ice Sheet
AmIS	Amery Ice Shelf
BMB	Basal Mass Balance
EAIS	East Antarctic Ice Sheet
EDC	Epica Dome C
EDML	Epica Dronning Maud Land
ELRA	Elastic Lithosphere Relaxed Asthenosphere
ERA	ECMWF (European Centre for Medium-range Weather Forecasts) Re-Analyses
FRIS	Filchner-Ronne Ice Shelf
GCM	General Circulation Model
GIA	Glacial Isostatic Adjustment
GLR	Grounding Line Retreat
IMAU	Institute for Marine and Atmospheric research Utrecht
IPCC AR5	Intergovernmental Panel on Climate Change Assessment Report 5
LGM	Last Glacial Maximum
MH	Mid-Holocene
OMC	Onset of open Marine Conditions
PD	Present-Day
PMIP	Paleoclimate Modelling Intercomparison Project
RACMO	Regional Atmospheric Climate MOdel
RCM	Regional Climate Model
RCP	Representative Concentration Pathway
RIS	Ross Ice Shelf
SIA	Shallow Ice Approximation
SMB	Surface Mass Balance

SPECMAP	SPECTral MApping Project)
SSA	Shallow Shelf Approximation
WAIS	West Antarctic Ice Sheet
WDC	WAIS Divide ice Core
WMO	World Meteorological Organisation
WOCE	World Ocean Circulation Experiment

Bibliography

- Ackert Jr., R.P., A.E. Putnam, S. Mukhopadhyay, D. Pollard, R.M. DeConto, M.D. Kurz and H.W. Borns Jr. (2013) Controls on interior West Antarctic Ice Sheet Elevations: inferences from geologic constraints and ice sheet modeling. *Quaternary Science Reviews* 65:26–38, DOI 10.1016/j.quascirev.2012.12.017
- Amos, J. (2013) Antarctic's Pine Island glacier produces giant iceberg. *BBC News*
- Anderson, J.B., S.S. Shipp, A.L. Lowe, J. Smith Wellner and A.B. Mosola (2002) The Antarctic Ice Sheet during the Last Glacial Maximum and its subsequent retreat history: a review. *Quaternary Science Reviews* 21:49–70
- Annan, J.D. and J.C. Hargreaves (2013) A new global reconstruction of temperature changes at the Last Glacial Maximum. *Climate of the Past* 9:367–376, DOI 10.5194/cp-9-367-2013
- Aschwanden, A., G. Aðalgeirsdóttir and C. Khroulev (2013) Hindcasting to measure ice sheet model sensitivity to initial states. *The Cryosphere* 7:1083–1093, DOI 10.5194/tc-7-1083-2013
- Bamber, J.L., R.E.M. Riva, B.L.A. Vermeersen and A.M. LeBrocq (2009) Reassessment of the potential sea-level rise from a collapse of the WAIS. *Science* 324:901–903, DOI 10.1126/science.1169335
- Benn, D.I., C.R. Warren and R.H. Mottram (2007) Calving processes and the dynamics of calving glaciers. *Earth-Science Reviews* 82:143–179, DOI 10.1016/j.earscirev.2007.02.002
- Bentley, M.J. (1999) Volume of antarctic ice at the last glacial maximum and its impact on global sea level change. *Quaternary Science Reviews* 18:1569–1595
- Bentley, M.J. (2010) The Antarctic palaeo record and its role in improving predictions of future Antarctic Ice Sheet change. *Journal of Quaternary Science* 25:5–18, DOI 10.1002/jqs.1287
- Bindschadler, R.A., S. Nowicki, A. Abe-Ouchi, A. Aschwanden, H. Choi, J. Fastook, G. Granzow, R. Greve, G. Gutowski, U. Herzfeld, C. Jackson, J. Johnson, C. Khroulev, A. Levermann, W.H. Lipscomb, M.A. Martin, M. Morlighem, B.R. Parizek, D. Pollard, S.F. Price, D. Ren, F. Saito, T. Sato, H. Seddik, H. Seroussi, K. Takahashi and W. Li Wang (2013) Ice-sheet model sensitivities to environmental forcing and their use in projecting future sea level (the SeaRISE project). *Journal of Glaciology* 59(214):195–224, DOI 10.3189/2013JG12J125
- Bintanja, R. and R.S.W. van de Wal (2008) North American ice-sheet dynamics and the onset of 100,000-year glacial cycles. *Nature* 454:869–872, DOI 10.1038/nature07158
- Bintanja, R., R.S.W. van de Wal and J. Oerlemans (2002) Global ice volume variations through the last glacial cycle simulated by a 3-D ice-dynamical model. *Quaternary International* 95-96:11–23
- Braconnot, P., B. Otto-Bliesner, S. Harrison, S. Joussaume, J.-Y. Peterschmitt, A. Abe-Ouchi, M. Crucifix, E. Driesschaert, Th. Fichefet, C.D. Hewitt, M. Kageyama, A. Kitoh, A. Láiné, M.-F. Loutre, O. Marti, U. Merkel, G. Ramstein, P. Valdes, S.L. Weber, Y. Yu and Y. Zhao (2007) Results of PMIP2 coupled simulations of the Mid-Holocene and Last Glacial Maximum - Part 1: experiments and large-scale

- features. *Climate of the Past* 3:261–277, DOI 10.5194/cp-3-261-2007
- Brewer, S., J. Guiot and F. Torre (2007) Mid-Holocene climate change in Europe: a data-model comparison. *Climate of the Past* 3
- Briggs, R.D. and L. Tarasov (2013) How to evaluate model-derived deglaciation chronologies: a case study using Antarctica. *Quaternary Science Reviews* 63:109–127, DOI 10.1016/j.quascirev.2012.11.021
- Briggs, R.D., D. Pollard and L. Tarasov (2013) A glacial systems model configured for large ensemble analysis of Antarctic deglaciation. *The Cryosphere* 7:1949–1970, DOI 10.5194/tc-7-1949-2013
- Budretsky, A.B. (1984) New absolute minimum of air temperature. *Information Bulletin of Soviet Antarctic Expedition* 105
- Bueler, E. and J. Brown (2009) Shallow shelf approximation as a "sliding law" in a thermomechanically coupled ice sheet model. *Journal of Geophysical Research* 114(F03008):1–21, DOI 10.1029/2008JF001179
- Buiron, D., J. Chappellaz, B. Stenni, M. Frezzotti, M. Baumgartner, E. Capron, A. Landais, B. Lemieux-Dudon, V. Masson-Delmotte, M. Montagnat, F. Parrenin and A. Schilt (2011) TALDICE-1 age scale of the Talos Dome deep ice core, East Antarctica. *Climate of the Past* 7, DOI 10.5194/cp-7-1-2011
- Center for Advanced Marine Core Research, Kochi University (2006) Marine Core Research Objectives. <http://www.kochi-u.ac.jp/marine-core/research/>
- Church, J.A., P.U. Clark, A. Cazenave, J.M. Gregory, S. Jevrejeva, A. Levermann, M.A. Merrifield, G.A. Milne, R.S. Nerem, P.D. Nunn, A.J. Payne, W.T. Pfeffer, D. Stammer and A.S. Unnikrishnan (2014) Climate Change 2013: The Physical Science Basis. Contribution of Working Group I to the Fifth Assessment Report on the Intergovernmental Panel on Climate Change, Cambridge University Press, Cambridge, United Kingdom, chap Sea Level Change, pp 1137–1216. 13
- Clark, P.U. and A.C. Mix (2002) Ice sheets and sea level of the Last Glacial Maximum. *Quaternary Science Reviews* 21:1–7
- Clarke, G.K.C. (2005) Subglacial Processes. *Annual Review of Earth and Planetary Sciences* 33:247–276, DOI 10.1146/annurev.earth.33.092203.122621
- Collins, M., R. Knutti, J. Arblaster, J.-L. Dufresne, T. Fichefet, P. Friedlingstein, X. Gao, W.J. Gutowski, T. Johns, G. Krinner, M. Shongwe, C. Tebaldi, A.J. Weaver and M. Wehner (2014) Climate Change 2013: The Physical Science Basis. Contribution of Working Group I to the Fifth Assessment Report on the Intergovernmental Panel on Climate Change, Cambridge University Press, Cambridge, United Kingdom, chap Long-term Climate Change: Projections, Commitments and Irreversibility, pp 1029–1136. 12
- Cox, D. (2012) Chapter 7: Glaciers, Deserts, and Wind. coxclasses.com/earthscience/ch7/esch7.html
- Crucifix, M., M.-F. Loutre, K. Lambeck and A. Berger (2001) Effect of isostatic rebound on modelled ice volume variations during the last 200 kyr. *Earth and Planetary Science Letters* 184:623–633
- Cuffey, K.M. and W.S.B. Paterson (2010) The physics of glaciers, 4th edn. Elsevier: Butterworth-Heinemann, Burlington, MA, USA
- Dansgaard, W. (1964) Stable isotopes in precipitation. *Tellus* 52B:19–36
- De Boer, B. (2012) A reconstruction of temperature, ice volume and atmospheric CO₂ over the past 40 million years. PhD thesis, Utrecht University, Utrecht
- De Boer, B., R.S.W. van de Wal, L.J. Lourens and R. Bintanja (2012) Transient nature of the Earth's climate and the implications for the interpretation of benthic $\delta^{18}\text{O}$ records. *Palaeogeography, Palaeoclimatology, Palaeoecology* 335-336:4–11, DOI 10.1016/j.palaeo.2011.02.001
- De Boer, B., R.S.W. van de Wal, L.J. Lourens, R. Bintanja and T.J. Reerink (2013) A continuous simulation of global ice volume over the past 1 million years with 3-D ice-sheet models. *Climate Dynamics* 41:1365–1384, DOI 10.1007/s00382-012-1562-2
- De Boer, B., L.J. Lourens and R.S.W. van de Wal (2014a) Persistent 400,000 year variability of Antarctic ice volume and the carbon cycle is revealed throughout the Plio-Pleistocene. *Nature Communications* 5(2999), DOI 10.1038/ncomms3999
- De Boer, B., P. Stocchi and R.S.W. van de Wal (2014b) A fully coupled 3-D ice-sheet - sea-level model: algorithm and applications. *Geoscientific Model Development Discussion* 7:3505–3544, DOI 10.5194/gmdd-7-3505-2014
- DeConto, R.M. and D. Pollard (2003) Rapid Cenozoic glaciation of Antarctica induced by declining atmo-

- spheric CO₂. *Nature* 421:245–249, DOI 10.1038/nature01290
- Denton, G.H. and T.J. Hughes (2002) Reconstructing the Antarctic Ice Sheet at the Last Glacial Maximum. *Quaternary Science Reviews* 21:193–202, DOI 10.1016/S0277-3791(01)00090-7
- Depoorter, M.A., J.L. Bamber, J.A. Griggs, J.T.M. Lenaerts, S.R.M. Ligtnerberg, M.R. van den Broeke and G. Moholdt (2013) Calving fluxes and basal melt rates of Antarctic ice shelves. *Nature* 502:89–92, DOI 10.1038/nature12567
- Dinniman, M.S., J.M. Klinck and W.O. Smith Jr. (2011) A model study of Circumpolar Deep Water on the West Antarctic Peninsula and Ross Sea continental shelves. *Deep-Sea Research II* 58:1508–1523, DOI 10.1016/j.dsr2.2010.11.013
- Emiliani, C. (1955) Pleistocene temperatures. *The Journal of Geology* 63:538–578
- Ettema, J., M.R. van den Broeke, E. van Meijgaard, W.J. van de Berg, J.L. Bamber, J.E. Box and R.C. Bales (2009) Higher surface mass balance of the Greenland ice sheet revealed by high-resolution climate modeling. *Geophysical Research Letters* 36(L12501), DOI 10.1029/2009GL038110
- Ettema, J., M.R. van den Broeke, E. van Meijgaard, W.J. van de Berg, J.E. Box and K. Steffen (2010) Climate of the greenland ice sheet using a high-resolution climate model, part 1: Evaluation. *The Cryosphere* 4:511–527, DOI 10.5194/tc-4-511-2010
- Forte, A.M. and J.X. Mitrovica (2001) Deep-mantle high-viscosity flow and thermochemical structure inferred from seismic and geodynamic data. *Nature* 410:1049–1056
- Fox Maule, C., M.E. Purucker, N. Olsen and K. Mosegaard (2005) Heat flux anomalies in Antarctica revealed by satellite magnetic data. *Science* 309:464–467, DOI 10.1126/science.1106888
- Frankcombe, L.M., P. Spence, A. McC. Hogg, M.H. England and S.M. Griffies (2013) Sea level changes forced by Southern Ocean winds. *Geophysical Research Letters* 40:5710–5715, DOI 10.1002/2013GL058104
- Fretwell, P., H.D. Pritchard, D.G. Vaughan, J.L. Bamber, N.E. Barrand, R. Bell, C. Bianchi, R.G. Bingham, D.D. Blankenship, G. Casassa, G. Catania, D. Callens, H. Conway, A.J. Cook, H.F.J. Corr, D. Damaske, V. Damm, F. Ferraccioli, R. Forsberg, S. Fujita, Y. Gim, P. Gogineni, J.A. Griggs, R.C.A. Hindmarsh, P. Holmlund, J.W. Holt, R.W. Jacobel, A. Jenkins, W. Jokat, T. Jordan, E.C. King, J. Kohler, W. Krabill, M. Riger-Kusk, K.A. Langley, G. Leitchenkov, C. Leuschen, B.P. Luyendyk, K. Matsuoka, J. Mouginot, F.O. Nitsche, Y. Nogi, O.A. Nost, S.V. Popov, E. Rignot, D.M. Rippin, A. Rivera, J. Roberts, N. Ross, M.J. Siegert, A.M. Smith, D. Steinhage, M. Studinger, B. Sun, B.K. Tinto, B.C. Welch, D. Wilson, D.A. Young, C. Xiangbin and A. Zirizzotti (2013) Bedmap2: improved ice bed, surface and thickness datasets for Antarctica. *The Cryosphere* 7:375–393, DOI 10.5194/tc-7-375-2013
- Gibson, J.K., P.Källberg, S. Uppala, A. Hernandez, A. Nomura and E. Serrano (1999) ERA ECMWF Re-Analysis Project Report Series 1. ERA-15 Description. Tech. rep., European Centre for Medium-Range Weather Forecasts
- Glen, J.W. (1958) The flow law of ice: A discussion on the assumptions made in glacier theory, their experimental foundations and consequences. *IASH Publ* 47:171–183
- Golledge, N.R., C.J. Fogwill, A.N. Mackintosh and K.M. Buckley (2012) Dynamics of the last glacial maximum Antarctic ice-sheet and its response to ocean forcing. *Proceedings of the National Academy of Sciences* 109(40):16,052–16,056, DOI 10.1073/pnas.1205385109
- Golledge, N.R., R.H. Levy, R.M. McKay, C.J. Fogwill, D.A. White, A.G.C. Graham, J.A. Smith, C.-D. Hillenbrand, K.J. Licht, G.H. Denton, R.P. Ackert Jr., S.M. Maas and B.L. Hall (2013) Glaciology and geological signature of the Last Glacial Maximum Antarctic Ice Sheet. *Quaternary Science Reviews* 78:225–247, DOI 10.1016/j.quascirev.2013.08.011
- Gomez, N., D. Pollard and J.X. Mitrovica (2013) A 3-D coupled ice sheet - sea level model applied to Antarctica through the last 40 ky. *Earth and Planetary Science Letters* 384:88–99, DOI 10.1016/j.epsl.2013.09.042
- Hall, B.L. (2009) Holocene glacial history of Antarctica and the sub-Antarctic islands. *Quaternary Science Reviews* 28:2213–2230, DOI 10.1016/j.quascirev.2009.06.011
- Hartmann, D.L., A.M.G. Klein Tank, M. Rusticucci, L.V. Alexander, S. Brönnimann, Y. Abdul-Rahman Charabi, F.J. Dentener, E.J. Dlugokencky, D.R. Easterling, A. Kaplan, B.J. Soden, P.W. Thorne, M. Wild and P. Zhai (2014) Climate Change 2013: The Physical Science Basis. Contribution of Working Group

- I to the Fifth Assessment Report on the Intergovernmental Panel on Climate Change, Cambridge University Press, Cambridge, United Kingdom, chap Observations: Atmosphere and Surface, pp 159–254. 2
- Hassold, N.J.C., D.K. Rea, B.A. van der Pluijm and J.M. Parés (2009) A physical record of the Antarctic Circumpolar Current: Late Miocene to recent slowing of abyssal circulation. *Palaeogeography, Palaeoclimatology, Palaeoecology* 275:28–36, DOI 10.1016/j.palaeo.2009.01.011
- Hellmer, H.H., F. Kauker, R. Timmermann, J. Determann and J. Rae (2012) Twenty-first-century warming of a large Antarctic ice-shelf cavity by a redirected coastal current. *Nature* 485:225–228, DOI 10.1038/nature11064
- Helsen, M.M. (2006) On the interpretation of stable isotopes in Antarctic precipitation. PhD thesis, Utrecht University
- Helsen, M.M., R.S.W. van de Wal, M.R. van den Broeke, W.J. van de Berg and J. Oerlemans (2012) Coupling of climate models and ice sheet models by surface mass balance gradients: application to the Greenland Ice Sheet. *The Cryosphere* 6:255–272, DOI 10.5194/tc-6-255-2012
- Herrmann, N. (2012) Rock Hunting. www.polar-trec.com
- Holland, D.M. and A. Jenkins (1999) Modeling thermodynamic ice-ocean interactions at the base of an ice shelf. *Journal of physical oceanography* 29:1787–1800
- Huerta, A.D. and D.L. Harry (2007) The transition from diffuse to focused extension: Modeled evolution of the West Antarctic Rift system. *Earth and Planetary Science Letters* 255:133–147, DOI 10.1016/j.epsl.2006.12.011
- Hughes, T. (1975) The West Antarctic Ice Sheet: Instability, disintegration, and initiation of Ice Ages. *Reviews of geophysics and space physics* 13:502–526
- Hutter, L. (1983) *Theoretical Glaciology*. D. Reidel, Dordrecht, The Netherlands
- Huybrechts, Ph. (1990) A 3-D model for the Antarctic Ice Sheet: a sensitivity study on the glacial-interglacial contrast. *Climate Dynamics* 5:79–92
- Huybrechts, Ph. (1992) The Antarctic ice sheet and environmental change: a three-dimensional modelling study. *Berichte zur Polarforschung* 99:1–241
- Huybrechts, Ph. (2002) Sea-level changes at the LGM from ice-dynamic reconstructions of the Greenland and Antarctic ice sheets during the glacial cycles. *Quaternary Science Reviews* 21:203–231
- Huybrechts, Ph., J. Gregory, I. Janssens and M. Wild (2004) Modelling Antarctic and Greenland volume changes during the 20th and 21st centuries forced by GCM time slice integrations. *Global and Planetary Change* 42:83–105
- Imbrie, J., J.D. Hays, D.G. Martinson, A. McIntyre, A.C. Mix, J.J. Morley, N.G. Pisias, W.L. Prell and N.J. Shackleton (1984) *Milankovitch and Climate, Part 1*, D. Reidel, Dordrecht, The Netherlands, chap The orbital theory of Pleistocene climate: Support from a revised chronology of the marine $\delta^{18}\text{O}$ record, pp 269–305
- Ingólfsson, Ó., C. Hjort, P.A. Berkman, S. Björck, E. Colhoun, I.D. Goodwin, B. Hall, K. Hirakawa, M. Melles, P. Möller and M.L. Prentice (1998) Antarctic glacial history since the Last Glacial Maximum: an overview of the record on land. *Antarctic Science* 10:326–344
- Jenkins, A. and C.S.M. Doake (1991) Ice-ocean interaction on Ronne Ice Shelf, Antarctica. *Journal of Geophysical Research* 96(C1):791–813
- Joughin, I. and D.R. MacAyeal (2005) Calving of large tabular icebergs from ice shelf rift systems. *Geophysical Research Letters* 32(L02501), DOI 10.1029/2004GL020978
- Jouzel, J., C. Lorius, J.R. Petit, C. Genthon, N.I. Barkov, V.M. Kotlyakov and V.M. Petrov (1987) Vostok ice core: A continuous isotope temperature record over the last climatic cycle (160,000 years). *Nature* 329:402–408
- Jouzel, J., V. Masson-Delmotte, O. Cattani, G. Dreyfus, S. Falourd, G. Hoffmann, B. Minster, J. Nouet, J.M. Barnola, J. Chappellaz, H. Fischer, J.C. Gallet, S. Johnsen, M. Leuenberger, L. Loulergue, D. Luethi, H. Oerter, F. Parrenin, G. Raisbeck, D. Raynaud, A. Schilt, J. Schwander, E. Selmo, R. Souchez, R. Spahni, B. Stauffer, J.P. Steffensen, B. Stenni, T.F. Stocker, J.L. Tison, M. Werner and E.W. Wolff (2007) EPICA Dome C ice core 800kyr deuterium data and temperature estimates. IGBP PAGES/World Data Center for Paleoclimatology data contribution series 2007-091, NOAA/NCDC Paleoclimatology Program,

- Boulder CO, USA
- Kawamura, K., R. Uemura, M. Hideaki, S. Fujita, K. Azuma, Y. Fujii, O. Watanabe and F. Vimeux (2007) Dome Fuji ice core preliminary temperature reconstruction, 0-340 kyr. ICBP PAGES/World Data Center for Paleoclimatology data contribution series 2007-074, NOAA, Boulder CO, USA
- Knauss, J.A. (1997) Introduction to physical oceanography, 2nd edn. Prentice Hall, Upper Saddle River, New Jersey
- Kuipers Munneke, P., M.R. van den Broeke, J.T.M. Lenaerts, M.G. Flanner, A.S. Gardner and W.J. van de Berg (2011) A new albedo parameterization for use in climate models over the Antarctic ice sheet. *Journal of Geophysical Research* 116(D05114), DOI 10.1029/2010JD015113
- Le Brocq, A.M., A.J. Payne and A. Vieli (2010) An improved Antarctic dataset for high resolution numerical ice sheet models (ALBMAP v1). *Earth System Science Data* 2:247–260, DOI 10.5194/essd-2-247-2010
- Le Meur, E. and Ph. Huybrechts (1996) A comparison of different ways of dealing with isostasy: examples from modelling the Antarctic ice sheet during the last glacial cycle. *Annals of Glaciology* 23:309–317
- Lenaerts, J.T.M., M.R. van den Broeke, S.J. Déry, E. van Meijgaard, W.J. van de Berg, S.P. Palm and J. Sanz Rodrigo (2012a) Modeling drifting snow in Antarctica with a regional climate model: 1. Methods and model evaluation. *Journal of Geophysical Research* 117(D05108):1–17, DOI 10.1029/2011JD016145
- Lenaerts, J.T.M., M.R. van den Broeke, W.J. van de Berg, E. van Meijgaard and P. Kuipers Munneke (2012b) A new, high-resolution surface mass balance map of Antarctica (1979-2010) based on regional atmospheric climate modeling. *Geophysical Research Letters* 39(L04501):1–5, DOI 10.1029/2011GL050713
- Ligtenberg, S.R.M., W.J. van de Berg, M.R. van den Broeke, J.G.L. Rae and E. van Meijgaard (2013) Future surface mass balance of the Antarctic ice sheet and its influence on sea level change, simulated by a regional atmospheric climate model. *Climate Dynamics* 41:867–884, DOI 10.1007/s00382-013-1749-1
- Little, C.M., N.M. Urban and M. Oppenheimer (2013) Probabilistic framework for assessing the ice sheet contribution to sea level change. *Proceedings of the National Academy of Sciences* 110(9):3264–3269, DOI 10.1073/pnas.1214457110
- Livingstone, S.J., C. Ó. C.R. Stokes, C.-D. Hillenbrand, A. Vieli and S.S.R. Jamieson (2012) Antarctic palaeo-ice streams. *Earth-Science Reviews* 111:90–128, DOI 10.1016/j.earscirev.2011.10.003
- Lythe, M.B., D.G. Vaughan and the BEDMAP Consortium (2001) BEDMAP: A new ice thickness and sub-glacial topographic model of Antarctica. *Journal of Geophysical Research - Solid Earth* 106(B6):11,335–11,351, DOI 10.1029/2000JB900449
- Ma, Y., O. Gagliardini, C. Ritz, F. Gillet-Chaulet, G. Durand and M. Montagnat (2010) Enhancement factors for grounded ice and ice shelves inferred from an anisotropic ice-flow model. *Journal of Glaciology* 56(199):805–812, DOI 10.3189/002214310794457209
- Maris, M.N.A., S.R.M. Ligtenberg, M. Crucifix, B. de Boer and J. Oerlemans (2014) Modelling the evolution of the Antarctic Ice Sheet since the last interglacial. *The Cryosphere Discussions* 8:85–120, DOI 10.5194/tcd-8-85-2014
- Masson-Delmotte, V., M. Kageyama, P. Braconnot, S. Charbit, G. Krinner, C. Ritz, E. Guilyardi, J. Jouzel, A. Abe-Ouchi, M. Crucifix, R.M. Gladstone, C.D. Hewitt, A. Kitoh, A.N. LeGrande, O. Marti, U. Merkel, T. Motoi, R. Ohgaito, B. Otto-Bliesner, W.R. Peltier, I. Ross, P.J. Valdes, G. Vettoretti, S.L. Weber, F. Wolk and Y. Yu (2006) Past and future polar amplification of climate change: climate model intercomparisons and ice-core constraints. *Climate Dynamics* 26:513–529, DOI 10.1007/s00382-005-0081-9
- Masson-Delmotte, V., D. Buiron, A. Ekaykin, M. Frezzotti, H. Gallée, J. Jouzel, G. Krinner, A. Landais, H. Motoyama, H. Oerter, K. Pol, D. Pollard, C. Ritz, E. Schlosser, L.C. Sime, H. Sodemann, B. Stenni, R. Uemura and F. Vimeux (2011) A comparison of the present and last interglacial periods in six Antarctic ice cores. *Climate of the Past* 7, DOI 10.5194/cp-7-397-2011
- McKay, R.M., G.B. Dunbar, T.R. Naish, P.J. Barrett, L. Carter and M. Harper (2008) Retreat history of the Ross Ice Sheet (Shelf) since the Last Glacial Maximum from deep-basin sediment cores around Ross Island. *Palaeogeography, Palaeoclimatology, Palaeoecology* 260:245–261, DOI 10.1016/j.palaeo.2007.08.015
- Moody, Ryan (2007) *Cucullaea raea* (arcidae). Flickr
- Morelli, A. and S. Danesi (2004) Seismological imaging of the Antarctic continental lithosphere: a review. *Global and Planetary Change* 42:155–165, DOI 10.1016/j.gloplacha.2003.12.005

- Morland, L.W. (1987) Unconfined ice-shelf flow. In: Van der Veen, C.J. and J. Oerlemans (eds) Dynamics of the West Antarctic Ice Sheet, D. Reidel, Dordrecht, The Netherlands, pp 99–116
- Murphy, B.F., I. Marsiat and P. Valdes (2002) Atmospheric contributions to the surface mass balance of Greenland in the HadAM3 atmospheric model. *Journal of Geophysical Research* 107(D21):4556, DOI 10.1029/2001JD000389
- NASA (2013) The coldest place in the world. URL http://science.nasa.gov/science-news/science-at-nasa/2013/09dec_coldspot/
- Nicholls, K.W., S. Østerhus, K. Makinson and T. Gammelsrød (2009) Ice-ocean processes over the continental shelf of the southern Weddell Sea, Antarctica: a review. *Reviews of geophysics* 47(RG3003):1–23, DOI 8755-1209/09/2007RG000250
- Nowicki, S., R.A. Bindshadler, A. Abe-Ouchi, A. Aschwanden, E. Bueler, H. Choi, J. Fastook, G. Granzow, R. Greve, G. Gutowski, U. Herzfeld, C. Jackson, J. Johnson, C. Khroulev, E. Larour, A. Levermann, W.H. Lipscomb, M.A. Martin, M. Morlighem, B.R. Parizek, D. Pollard, S.F. Price, D. Ren, E. Rignot, F. Saito, T. Sato, H. Seddik, H. Seroussi, K. Takahashi, R. Walker and W. Li Wang (2013) Insights into spatial sensitivities of ice mass response to environmental change from the SeaRISE ice sheet modeling project I: Antarctica. *Journal of Geophysical Research* 118:1002–1024, DOI 10.1002/jgrf.20081
- Orsi, A.H. and T. Whitworth III (2004) Hydrographic Atlas fo the World Ocean Circulation Experiment (WOCE) Volume 1: Southern Ocean. International WOCE Project Office, Southampton, U.K.
- Overpeck, J.T., B.L. Otto-Bliesner, G.H. Miller, D.R. Muhs, R.B. Alley and J.T. Kiehl (2006) Paleoclimatic evidence for future ice-sheet instability and rapid sea-level rise. *Science* 311:1747–1750, DOI 10.1126/science.1115159
- Oxford Dictionaries (2013) URL <http://oxforddictionaries.com>
- Pattyn, F., C. Schoof, L. Perichon, R.C.A. Hindmarsh, E. Bueler, B. de Fleurian, G. Durand, O. Gagliardini, R. Gladstone, D. Goldberg, G.H. Gudmundsson, V. Lee, F.M. Nick, A.J. Payne, D. Pollard, O. Rybak, F. Saito and A. Vieli (2012) Results of the Marine Ice Sheet Model Intercomparison Project, MISMP. *The Cryosphere* 6:573–588, DOI 10.5194/tc-6-573-2012
- Pattyn, F., L. Perichon, G. Durand, L. Favier, O. Gagliardini, R.C.A. Hindmarsh, T. Zwinger, T. Albrecht, S. Cornford, D. Docquier, J.J. Fürst, D. Goldberg, G.H. Gudmundsson, A. Humbert, M. Hütten, Ph. Huybrechts, G. Jouvett, T. Kleiner, E. Larour, D. Martin, M. Morlighem, A.J. Payne, D. Pollard, M. Rückamp, O. Rybak, H. Seroussi, M. Thoma and N. Wilkens (2013) Grounding-line migration in plan-view marine ice-sheet models: results of the ice2sea MISMP3d intercomparison. *Journal of Glaciology* 59:410–422, DOI 10.3189/2013JoG12J129
- Peltier, W.R. (2004) Global glacial isostasy and the surface of the ice-age Earth: The ICE-5G (VM2) Model and GRACE. *Annual Review of Earth and Planetary Sciences* 32:111–149, DOI 10.1146/annurev.earth.32.082503.144359
- Petit, J.R., J. Jouzel, D. Raynaud, N.I. Barkov, J.M. Barnola, I. Basile, M. Bender, J. Chappellaz, J. Davis, G. Delaygue, M. Delmotte, V.M. Kotlyakov, M. Legrand, V. Lipenkov, C. Lorius, L. Pépin, C. Ritz, E. Saltzman and M. Stievenard (1999) Climate and atmospheric history of the past 420,000 years from the Vostok ice core, Antarctica. *Nature* 399:429–436
- Philippon, G., G. Ramstein, S. Charbit, M. Kageyama, C. Ritz and C. Dumas (2006) Evolution of the Antarctic ice sheet throughout the last deglaciation: A study with a new coupled climate - north and south hemisphere ice sheet model. *Earth and Planetary Science Letters* 248:750–758, DOI 10.1016/j.epsl.2006.06.017
- Pollard, D. and R.M. DeConto (2009) Modeling West Antarctic ice sheet growth and collapse through the past five million years. *Nature* 458:329–332, DOI 10.1038/nature07809
- Pollard, D. and R.M. DeConto (2012a) A simple inverse method for the distribution of basal sliding coefficients under ice sheets, applied to Antarctica. *The Cryosphere* 6:953–971, DOI 10.5194/tc-6-953-2012
- Pollard, D. and R.M. DeConto (2012b) Description of a hybrid ice sheet-shelf model, and application to Antarctica. *Geoscientific Model Development* 5:1273–1295, DOI 10.5194/gmd-5-1273-2012
- Ranalli, G. (1995) Rheology of the Earth, 2nd edn. Chapman & Hall, 2-6 Boundary Row, London
- Reerink, T.J. (2013) Documentation ICEDYN-package: deriving the model equations. Tech. rep., IMAU
- Reijmer, C.H., E. van Meijgaard and M.R. van den Broeke (2005) Evaluation of temperature and wind

- over Antarctica in a Regional Atmospheric Climate Model using 1 year of automatic weather station data and upper air observations. *Journal of Geophysical Research* 110(D04103):1–12, DOI 10.1029/2004JD005234
- Ren, D., R. Fu, L.M. Leslie, J. Chen, C.R. Wilson and D.J. Karoly (2011) The Greenland Ice Sheet response to transient climate change. *Journal of Climate* 24:3469–3483, DOI 10.1175/2011JCLI3708.1
- Rignot, E., S. Jacobs, J. Mouginot and B. Scheuchl (2013) Ice-shelf melting around Antarctica. *Science* 341:266–270, DOI 10.1126/science.1235798
- Ritz, C., V. Rommelaere and C. Dumas (2001) Modeling the evolution of Antarctic ice sheet over the last 420,000 years: Implications for altitude changes in the Vostok region. *Journal of Geophysical Research* 106(D23):31,943–31,964
- Rohling, E.J., K. Grant, M. Bolshaw, A.P. Roberts, M. Siddall, Ch. Hemleben and M. Kucera (2009) Antarctic temperature and global sea level closely coupled over the past five glacial cycles. *Nature Geoscience* 2:500–504, DOI 10.1038/NGEO557
- Rojas, M., P. Moreno, M. Kageyama, M. Crucifix, C.D. Hewitt, A. Abe-Ouchi, R. Ohgaito, E.C. Brady and P. Hope (2009) The Southern Westerlies during the last glacial maximum in PMIP2 simulations. *Climate Dynamics* 32:525–548, DOI 10.1007/s00382-008-0421-7
- Royer, D.L. (2006) CO₂-forced climate thresholds during the Phanerozoic. *Geochimica et Cosmochimica Acta* 70:5665–5675, DOI 10.1016/j.gca.2005.11.031
- Schoof, C. (2007) Ice sheet grounding line dynamics: Steady states, stability and hysteresis. *Journal of Geophysical Research* 112(F03S28):1–19, DOI 10.1029/2006JF000664
- Shapiro, N.M. and M.H. Ritzwoller (2004) Inferring surface heat flux distributions guided by a global seismic model: particular application to Antarctica. *Earth and Planetary Science Letters* 223:213–224, DOI 10.1016/j.epsl.2004.04.011
- Steig, E.J., D.L. Morse, E.D. Waddington, M. Stuiver, P.M. Grootes, P.A. Mayewski, M.S. Twickler and S.I. Whitlow (2000) Wisconsinan and Holocene climate history from an ice core at Taylor Dome, western Ross Embayment, Antarctica. *Geografiska Annaler* 82 A(2-3):213–235
- Stenni, B., V. Masson-Delmotte, E. Selmo, H. Oerter, H. Meyer, R. Röthlisberger, J. Jouzel, O. Cattani, S. Falourd, H. Fischer, G. Hoffmann, P. Iacumin, S.J. Johnsen, B. Minster and R. Udisti (2010) The deuterium excess records of EPICA Dome C and Dronning Maud Land ice cores (East Antarctica). *Quaternary Science Reviews* 29:146–159, DOI 10.1016/j.quascirev.2009.10.009
- Stern, T.A. and U.S. ten Brink (1989) Flexural uplift of the Transantarctic Mountains. *Journal of Geophysical Research* 94(B8):10,315–10,330
- Stonehouse, B. (ed) (2002) *Encyclopedia of Antarctica and the Southern Oceans*. John Wiley & Sons, West Sussex, England
- Thomas, R.H. (1979) The dynamics of marine ice sheets. *Journal of Glaciology* 24(90):167–177
- UCAR/NCAR/CISL/VETS (2013) The NCAR Command Language (Version 6.1.2) [Software]. Boulder CO, DOI 10.5065/D6WD3XH5
- USGS (2013) Inside the earth. <http://pubs.usgs.gov/publications/text/inside.html>, URL <http://pubs.usgs.gov/publications/text/inside.html>
- Van de Berg, W.J. (2008) Present-day climate of antarctica, a study with a regional climate model. PhD thesis, Graduate School of Natural Sciences
- Van de Berg, W.J., M.R. van den Broeke, C.H. Reijmer and E. van Meijgaard (2005) Characteristics of the Antarctic surface mass balance (1958–2002) using a regional atmospheric climate model. *Annals of Glaciology* 41(1):97–104, DOI 10.3189/172756405781813302
- Van de Berg, W.J., M.R. van den Broeke, C.H. Reijmer and E. van Meijgaard (2006) Reassessment of the Antarctic surface mass balance using calibrated output of a regional atmospheric climate model. *Journal of Geophysical Research* 111(D11104):1–15, DOI 10.1029/2005JD006495
- Van de Berg, W.J., M.R. van den Broeke and E. van Meijgaard (2007) Heat budget of the East Antarctic lower atmosphere derived from a regional atmospheric climate model. *Journal of Geophysical Research* 112(D23101):1–14, DOI 10.1029/2007JD008613
- Van de Wal, R.S.W. (1999) The importance of thermodynamics for modeling the volume of the Greenland ice sheet. *Journal of Geophysical Research-Atmospheres* 104(D4):2887–3898

- Van den Berg, J., R.S.W. van de Wal, G.A. Milne and J. Oerlemans (2008) Effect of isostasy on dynamical ice-sheet modeling: A case study for Eurasia. *Journal of Geophysical Research - Solid Earth* 113(B05412), DOI 10.1029/2007JB004994
- Van den Broeke, M.R., W.J. van de Berg, E. van Meijgaard and C.H. Reijmer (2006) Identification of Antarctic ablation areas using a regional atmospheric climate model. *Journal of Geophysical Research* 111(D18110):1–14, DOI 10.1029/2006JD007127
- Van Meijgaard, E., L.H. van Ulft, W.J. van de Berg, F.C. Bosveld, B.J.J.M. van den Hurk, G. Lenderink and A.P. Siebesma (2008) The KNMI regional atmospheric climate model RACMO version 2.1. Royal Netherlands Meteorological Institute, De Bilt, The Netherlands
- Van Ommen, T.D. (2011) Interactive comment on "A model comparison study for the Antarctic region: present and past" by M.N.A. Maris et al. *Climate of the Past Discussions* 7(3583):C1772–C1773
- Van Ommen, T.D., V. Morgan and M.A.J. Curran (2004) Deglacial and Holocene changes in accumulation at Law Dome, East Antarctica. *Annals of Glaciology* 39:359–365
- Vaughan, D.G., J.C. Comiso, I. Allison, J. Carrasco, G. Kaser, R. Kwok, P. Mote, T. Murray, F. Paul, J. Ren, E. Rignot, O. Solomina, K. Steffen and T. Zhang (2014) Climate Change 2013: The Physical Science Basis. Contribution of Working Group I to the Fifth Assessment Report of the Intergovernmental Panel on Climate Change, Cambridge University Press, Cambridge, United Kingdom, chap Observations: Cryosphere, pp 317–382. 4
- Verleyen, E., D.A. Hodgson, G.A. Milne, K. Sabbe and W. Vyverman (2005) Relative sea-level history from the Lambert Glacier region, East Antarctica, and its relation to deglaciation and Holocene glacier readvance. *Quaternary Research* 63:45–52, DOI 10.1016/j.yqres.2004.09.005
- Waelbroeck, C., A. Paul, M. Kucera, A. Rosell-Melé, M. Weinelt, R. Schneider, A.C. Mix, A. Abelmann, L. Armand, E. Bard, S. Barker, T.T. Barrows, H. Benway, I. Cacho, M.-T. Chen, E. Cortijo, X. Crosta, A. de Vernal, T. Dokken, J. Duprat, H. Elderfield, F. Eynaud, R. Gersonde, A. Hayes, M. Henry, C. Hillaire-Marcel, C.-C. Huang, E. Jansen, S. Juggins, N. Kallel, T. Kiefer, M. Kienast, L. Labeyrie, H. Leclaire, L. Londeix, S. Mangin, J. Matthiessen, F. Marret, M. Meland, A.E. Morey, S. Mulitza, U. Pflaumann, N.G. Pisias, T. Radi, A. Rochon, E.J. Rohling, L. Sbaffi, C. Schäfer-Neth, S. Solignac, H. Spero, K. Tachikawa and J.-L. Turon (2009) Constraints on the magnitude and patterns of ocean cooling at the Last Glacial Maximum. *Nature Geoscience* 2:127–132, DOI 10.1038/NGEO411
- WAIS Divide Project Members (2013) Onset of deglacial warming in West Antarctica driven by local orbital forcing. *Nature* 500:440–444, DOI 10.1038/nature12376
- Weber, M.E., P.U. Clark, W. Ricken, J.X. Mitrovica, S.W. Hostetler and G. Kuhn (2011) Interhemispheric ice-sheet synchronicity during the Last Glacial Maximum. *Science* 334:1265–1269, DOI 10.1126/science.1209299
- Weertman, J. (1974) Stability of the junction of an ice sheet and an ice shelf. *Journal of Glaciology* 13:3–13
- Whitehouse, P.L., M.J. Bentley and A.M. Le Brocq (2012) A deglacial model for Antarctica: geological constraints and glaciological modelling as a basis for a new model of Antarctic glacial isostatic adjustment. *Quaternary Science Reviews* 32:1–24, DOI 10.1016/j.quascirev.2011.11.016
- Winkelmann, R., M.A. Martin, M. Haseloff, T. Albrecht, E. Bueler, C. Khroulev and A. Levermann (2011) The Potsdam Parallel Ice Sheet Model (PISM-PIK) - Part 1: Model description. *The Cryosphere* 5:715–726, DOI 10.5194/tc-5-715-2011
- Winkelmann, R., A. Levermann, M.A. Martin and K. Frieler (2012) Increased future ice discharge from Antarctica owing to higher snowfall. *Nature* 492:239–242, DOI 10.1038/nature11616
- Yanase, W. and A. Abe-Ouchi (2007) The LGM surface climate and atmospheric circulation over East Asia and the North Pacific in the PMIP2 coupled model simulations. *Climate of the Past* 3:439–451, DOI www.clim-past.net/3/439/2007
- Zweck, C. and Ph. Huybrechts (2005) Modeling of the northern hemisphere ice sheets during the last glacial cycle and glaciological sensitivity. *Journal of Geophysical Research* 110(D07103):1–24, DOI 10.1029/2004JD005489
- Zwinger, T., R. Greve, O. Gagliardini, T. Shiraiwa and M. Lyly (2007) A full Stokes-flow thermo-mechanical model for firn and ice applied to the Gorshkov crater glacier, Kamchatka. *Annals of Glaciology* 45:29–37, DOI 10.3189/172756407782282543

Bedankt

Promoveren is in veel opzichten als een lange fietstocht: je begint met goede moed, vraagt je op een gegeven moment af of je ooit het einde gaat halen en dan ineens is het af. Om het einde te bereiken zijn passie, doorzettingsvermogen en bovenal een goede bewegwijzering nodig. Daarom wil ik eerst jou bedanken Hans. Als promotor en begeleider heb je mijn werk niet alleen gefaciliteerd, maar ook in goede banen geleid. Jouw manier van begeleiden was een goede mix waarbij je mij zelf dingen liet uitzoeken en toch de vinger aan de pols hield. Bas, jij bent in mijn derde jaar als AIO mijn dagelijkse begeleider geworden, vooral omdat je die rol daarvoor ook al deels speelde, en nu ben je ook mijn co-promotor. Ik kon bij jou altijd binnenlopen met een ideetje of een probleem waar ik tegenaan liep en uiteindelijk ben je op het reddende idee gekomen om ANICE te gaan gebruiken, daar ben ik je erg dankbaar voor. Je positieve insteek heeft me ook geholpen om door te zetten nadat ik bij het IMAU weg was.

Aan de anderen waarmee ik heb samengewerkt op het IMAU: Stefan, Willem-Jan, Melchior, HOEMBA-genoten en de ijs-en klimaatgroep als geheel, bedankt voor jullie feedback op mijn artikelen en onderzoeksideoën. Marcel en Michael, jullie wil ik graag bedanken voor het gezond houden van mijn computer en voor de hulp bij het installeren van PISM en het gebruik van een supercomputer. Paul, bedankt dat je me hebt meegenomen naar Groenland en hebt laten zien hoe veldwerk gedaan wordt. Het was een onvergetelijke ervaring om over die enorme ijsskape te vliegen en erop te mogen rondlopen. Yvonne, Wanda en Sandra, bedankt voor jullie adviezen en voor het (mee) organiseren van menig leuk uitje.

Gelukkig hoeven we niet alleen maar hard te werken op het IMAU. De pétanque- en badmintontoernooien zorgden voor de nodige ontspanning, alsook het schaatsen en hardlopen, en in het bijzonder het wielrennen (dank voor de mooie tochtjes Jan, Jan en Michiel) dat we samen deden. Bedankt sportieve collega's! Dagelijkse

ontspanning was te vinden tijdens de lunch en de vermaarde koffie-thee (en taart) pauzes. Back in my room I was not alone. Aimée, as a senior PhD student you gave me a lot of advice, thank you for your help and your cheerful company. Bing, thank you for your patience and your kindness. Claudia, we have been roommates for only a short time, but thank you for bearing with me during my most stressful period.

Lieve 'Boxtelmeiden', Hetty, Moniek, Annet, Anneke, Els, Dianne en Lieke, door dik en dun zijn we al lange tijd samen. Jullie vriendschap heeft me al door heel wat heen gesleept, waaronder dit proefschrift. Bedankt voor al jullie steun en voor de vele leuke avondjes en weekenden. Tomek, Iris, Lineke en Evelyne, ook jullie ben ik dankbaar voor de vele leuke en goede gesprekken en de leuke dingen die we samen gedaan hebben. Vera, Mart, David, Martijn en Kevin, ook jullie ken ik al sinds de middelbare school, bedankt voor de gezellige bbq's en andere uitstapjes.

Lieve Hetty, dear Markella, a special thank you to you both for being my par-nymphs. You're both down-to-earth girls on whom I feel I can depend.

Lieve papa en mama, van kleins af aan hebben jullie me op een leuke manier gestimuleerd om me te interesseren voor wetenschap. Later heb ik altijd het gevoel gehad dat jullie me steunden en trots op me waren, heel veel dank daarvoor. Eelco, ik ben blij dat ik jou als broer heb, als ik een serieuze mening of hulp nodig heb geef je me die. Het laatste jaar had ik zelfdiscipline en doorzettingsvermogen nodig en wat dat betreft ben jij mijn voorbeeld geweest. Peter en Inge, Geert, Gerry, Joost, Lindy, en Oma (ik weet dat je bij ons bent, ook al ben je er niet meer), wat een gezellige, kleine familie hebben we. Jullie wil ik ook bedanken voor de leuke uitstapjes en jullie steun de afgelopen jaren.

Françoise, Guy, Manou, Arnaud, et petite Anaïs, merci de m'avoir si chaleureusement accueilli dans votre famille. Les visites en France étaient très reposantes et j'espère qu'il y en aura de nombreuses à venir.

Cher Cédric, nous nous sommes rencontré lors de ma dernière année de ma thèse et tu savais déjà ce qui allait se passer. Tu m'as réconforté, soutenu et supporté. Sans toi j'aurais eu des vraies difficultés pour finir. J'ai hâte de passer le future avec toi, merci d'être là.

About the author

Malou Maris was born on 11 January 1986 in Ommen, The Netherlands. At the age of four she and her parents moved to Oisterwijk, where she went to the neighbourhood primary school. Afterwards, she attended the Jacob Roelands Lyceum in Boxtel as a secondary education. Having been interested in the weather and astronomy since childhood and keen to live in the country's capital, she decided to study physics at the VU in Amsterdam. After obtaining her BSc diploma in physics she looked for a master



in meteorology and found it in Utrecht, where she followed the master Meteorology, Physical Oceanography and Climatology. Her master's research project led her to go abroad and for almost a year at the CEN in Grenoble, where she investigated the Pyrenean climate, and especially snowfall, over the past 50 years. Back in Utrecht she obtained her MSc in 2010, after which she started as a PhD-student under the supervision of Prof. Hans Oerlemans on the topic of modelling the evolution of the Antarctic Ice Sheet since the Last Glacial Maximum. The results obtained during these four years of research are presented in this thesis. During this project she had the opportunity to go on fieldwork to Greenland, attend a summer school, several conferences and to meet a lot of people from many different countries. Having developed a keen interest for computer science and sharpened her skill in programming during the four years as a PhD-student, Malou joined the international consulting company Alten in March 2014, where she now works as a scientific software engineer.